University of Nottingham
UK | CHINA | MALAYSIA

Development of a core–shell composite hydrogel for 3D bioprinting

Pritesh Mistry

A thesis submitted to the University of Nottingham for the degree of Doctor of Philosophy

September 2017

Abstract

Recently, 3D printing has become popular in the field of tissue engineering, where materials and biology are combined with the aim of producing functional tissues for regenerative medicine therapies and for *in vitro* disease and toxicology models. However, current 3D printing techniques are not able to produce functional tissue-engineered constructs that are physiologically-relevant in the long-term. Challenges arise when combining desired mechanical properties with biological properties in a single construct. Often, cell-supportive materials lack mechanical stability and mechanically-robust materials are unable to support cell growth and function. In addition, many native tissues and organs are heterogeneous, with graded properties. The recapitulation of these factors will help to produce more physiologically-relevant tissue replacements and *in vitro* models with better predictability.

This thesis seeks to combine biological and mechanical properties in a single core–shell strand: a mechanically-robust shell hydrogel encapsulating biologically active cell-laden core. This body of work has been split into three sections, the assessment of a hybrid material for use in the shell, the production of 3D printed constructs with core–shell strands, and the incorporation of gradients into these printed constructs.

First, the mechanical properties of a poly(ethylene glycol) diacrylate (PEGDA)/alginate hybrid hydrogel was assessed using tensile testing. The hybrid hydrogels demonstrated synergy in their mechanical properties in a composition-dependent manner. In the second part of this thesis, a coaxial printing method was developed by combining a coaxial needle with a commercial extrusion-based 3D printer. Extruded strands displayed distinct core and shell regions and were able to support cell viability and function for up to 6 weeks. In the final part of this thesis, gradients were incorporated into the shell of core–shell strands. Both soluble factors gradients and stiffness gradients were characterised, and their longevity within these printed constructs was studied.

In summary, core–shell strands have been shown to be a viable method to combine optimal mechanical and biological properties in a single construct. The core–shell technique could be made more complex with the addition of gradients, bringing printed constructs closer to their *in vivo* counterparts. With further research, this technique will help to create more physiologically-relevant tissue engineered constructs, which can drive research a step closer towards better disease models and future therapies.

Acknowledgements

This thesis would not have come to be without the help and support of many, many others, and here I would like to take the time to thank them.

I would first like to thank my supervisors: Dr Jing Yang, Dr Andrew Bennett, Professor Morgan Alexander, and Professor Kevin Shakesheff, for their continued guidance throughout this project, and also for the opportunities they provided me with.

I would like to thank Dr Felicity Rose, and all members, both past and present, in the Division of Regenerative Medicine and Cellular Therapies (formerly the Tissue Engineering Group), for all those great scientific (and non-scientific) discussions. A special thanks goes to Teresa Marshall for her support throughout. I would also like to thank Dr Omar Qutachi for his advice, and for the synthesis of microparticles used in this work.

I would like to thank the "Bioprinting subgroup", Laura, Omar, Scarlett, Ahmed, Lara, Aruna, and Elisa. Thank you for all of the help you gave me, and for all the great times we had in the lab.

I am grateful to members of Dr Andrew Bennett's lab in the Queen's Medical Centre (Nottingham), particularly to Elke, Monika, and Fatima, for providing me with training, and for supplying the primary hepatic cells used in this project.

I would like to thank Professor Shoji Takeuchi, Dr Minghao Nie, and all of the members in the “t-lab”, for welcoming me so warmly during my placement at the University of Tokyo (Japan). Thank you for all of your assistance, and for the wonderful experience you left me with.

Thank you to Dr Oksana Kehoe and everyone at the Robert Jones & Agnes Hunt Orthopaedic Hospital in Oswestry for being so welcoming and for the fantastic experience during my mini-project.

Thank you to the EPSRC & MRC Centre for Doctoral Training in Regenerative Medicine for giving me the opportunity to carry out this studentship and for funding the work in this project (MRC-EPSRC EP/L015072/1), with special thanks to Dr Karen Coopman. Of course, thank you to DTC6 that were with me from the beginning, and to all the other DTC/CDT students I met along the way.

A big, big thank you my friends that I could always turn to throughout my PhD. I would list them all… but you know who you are!

Thank you to my family (mother, father, brothers) for being there during this long, long PhD, and for putting up with me nonetheless.

Finally, and last but not least, thank you Elisabetta Prina. Without you, this thesis would not have been possible. You really are a VIP.

List of publications

Journal publications

E. Prina, **P. Mistry**, L.E. Sidney, J. Yang, R.D. Wildman, M. Bertolin, C. Breda, B. Ferrari, V. Barbaro, A. Hopkinson, H.S. Dua, S. Ferrari, F.R.A.J. Rose, 2017. 3D Microfabricated Scaffolds and Microfluidic Devices for Ocular Surface Replacement: a Review. *Stem Cell Reviews and Reports,* 13(3), p.430-431.

P. Mistry, A. Aied, M. Alexander, K. Shakesheff, A. Bennett, J. Yang, 2017. Bioprinting Using Mechanically Robust Core–Shell Cell-Laden Hydrogel Strands. *Macromolecular Bioscience*, 17, 1600472.

M.J. Sawkins, **P. Mistry**, B.N. Brown, K.M. Shakesheff, L.J. Bonassar, J. Yang, 2015. Cell and protein compatible 3D bioprinting of mechanically strong constructs for bone repair. *Biofabrication*, 7(3), p.035004.

Conference proceedings

M. Nie, **P. Mistry**, J. Yang, S. Takeuchi, 2017. IEEE 30th International Conference on Micro Electro Mechanical Systems. Las Vegas, USA, 22nd–26th January 2017. *Institute of Electrical and Electronics Engineers*.

P. Mistry, A. Aied, M. Alexander, K. Shakesheff, A. Bennett, J. Yang, 2016. 16th Tissue & Cell Engineering Society Annual Meeting. London, UK, 4th–6th July 2016. *European Cells and Materials Journal.*

J. Yang, **P. Mistry**, K. Shakesheff, A. Aied, 2015. 4th Tissue Engineering and Regenerative Medicine International Society World Congress. Boston, USA, 8th–11th September 2015. *Tissue Engineering, Part A.*

Conference presentations

TERMIS (Tissue Engineering and Regenerative Medicine International Society) European Chapter Meeting, Davos, Switzerland, 26th–30th June 2017. Bioprinting using mechanically robust core-shell cell-laden strands. *Poster presentation.*

16th Tissue and Cell Engineering Society Annual Meeting, London, UK. 4th–6th July 2016. Bioprinting using mechanically robust core-shell cell-laden strands. *Oral presentation.*

Table of contents

List of figures

List of tables

List of abbreviations

Abbreviation	Definition
°C	Degrees Celsius
2D	Two dimensional
3D	Three dimensional
3T3	NIH Swiss mouse embryonic fibroblast cell line
ANOVA	Analysis of variance
BSA	Bovine serum albumin
$CaCl_2$	Calcium chloride
$CaSO_4$	Calcium sulfate
cc	Cubic centimetre
Da	Dalton
diH_2O	Deionised water
DMEM	Dulbecco's Modified Eagle's Medium
DMSO	Dimethyl sulfoxide
DNA	Deoxyribonucleic acid
ECM	Extracellular matrix
EDTA	Ethylenediaminetetraacetic acid
ELISA	Enzyme-linked immunosorbent assay
Em	Emission (wavelength)
EM	Elastic modulus
Ex	Excitation (wavelength)
FS	Failure strain
G	Gauge
g	Gram
GelMA	Gelatine methacrylate/methacryloyl
g_n	Standard acceleration due to gravity (9.80665 m s^{-2})

h	Hour
HBS	HEPES-buffered saline
HepG2	Hepatocellular carcinoma HepG2 cell line
HSA	Human serum albumin
HUVEC	Human umbilical vein endothelial cell
Hz	Hertz
I-2959	Irgacure-2959 / 2-Hydroxy-4′-(2-hydroxyethoxy)-2-methylpropiophenone
ID	Inner diameter
IgG	Immunoglobulin G
ihMSC	Immortalised human bone marrow-derived mesenchymal stem cell
L	Litre
LAP	Lithium phenyl(2,4,6-trimethylbenzoyl) phosphinate
m	metre
M	Molar
MEME	Minimum Essential Medium Eagle
mESC	Mouse embryonic stem cell
min	Min
mRNA	Messenger ribonucleic acid
MW	Molecular weight
MWCO	Molecular weight cut-off
OD	Outer diameter
Pa	Pascal
PBS	Phosphate-buffered saline
PCR	Polymerase chain reaction
PEGDA	Poly(ethylene glycol) diacrylate

PFA	Paraformaldehyde
PTFE	Polytetrafluoroethylene
qPCR	Quantitative polymerase chain reaction
RHSC	Primary rat hepatic stellate cell
RNA	Ribonucleic acid
rpm	Revolutions per min
RT	Room temperature
s	Second
SD	Standard deviation
SEM	Scanning electron microscope/microscopy
UK	United Kingdom
USA	United States of America
UTS	Ultimate tensile strength
UV	Ultraviolet
v/v	Volume per unit volume
W	Watt
w/v	Weight per unit volume
α	Significance level
αSMA	Alpha smooth muscle actin

Chapter 1 – Introduction

Tissue engineering

Regenerative medicine is a branch of research that aims to replace or repair damaged tissues and organs in order to restore normal function. Tissue engineering is a field of regenerative medicine which involves the creation of artificial tissues and organs that are biologically viable, and have all the function of their *in vivo* counterparts. Other than for regenerative medicine therapies, fabricated tissue engineered constructs may also be used as models for disease modelling, and in drug discovery for toxicology studies. Such models will help to better understand normal physiological function, how diseases impact upon this function, and also how drugs and other therapeutics act. One such organ requiring more physiologically-relevant tissue models is the liver. In the human body, the liver is the major site of drug metabolism and also a site of toxicity due to adverse side effects. Drug-induced liver injury (DILI) is the primary reason of liver failure and withdrawal of drugs from the market (Khetani and Bhatia, 2008). Animal models require supplementary data from human models due to variation between humans and other species. Current human tissues models either lack several liver-specific functions, are unable to function for long periods of time, lack liver-specific architectures, or display abnormal functions that are not physiologically-

relevant to humans (Marx, 2015). Overall, current major challenges are focused on the ability to fabricate physiologically-relevant constructs. These constructs should better match the normal physiology of the intended tissue or organ, and this can be by: containing all of the cell types present in that tissue or organ, arranging those cells in the same manner in which they are found *in vivo*, ensuring cells remain viable for the length of time required, and making sure these cells function as they do *in vivo*.

However, human physiology is complex. Factors that influence a cell's behaviour includes, but isn't limited to the cell type itself, how it is arranged within a tissue, motifs on neighbouring cells and/or the surrounding ECM, the stiffness of the ECM itself, and soluble factors such as growth factors and hormones. It is these signals that enable cells to differentiate and exhibit desired phenotypes (Kim and Mooney, 1998; Demirbag *et al.*, 2011). Gradients of these factors are also present and allow graded cell phenotype, allowing tissues to have regions of specific functionalities (Bracaglia *et al.*, 2017). An example is zonation in the liver, were hepatocytes closer to the hepatic portal vein carry out more gluconeogenesis, when compared to hepatocytes located closer to the central vein (Godoy et al., 2013).

3D printing

To overcome these fabrication challenges, 3D printing has rapidly gained interest in the field of tissue engineering due to its ability to fabricate complex structures on demand. 3D printing has been used to print whole organs, and is promoting the advent of personalised medicine (Wu and Hsu, 2015; Murphy and Atala, 2014). 3D printing, also known as additive manufacturing, is a technique by which 3D structures can be fabricated on demand from computer-aided designs. In this manner, heterogeneity can be incorporated into 3D printed constructs. Using light-based and ink-based techniques, 3D structures can be fabricated in a layer-by-layer manner. Currently, there are many types of 3D printing techniques, including stereolithography, selective laser sintering, fused deposition modelling, inkjet printing, laser-assisted printing and extrusion-based printing.

Stereolithography involves the layer-by-layer photo-polymerisation of a liquid polymer (**Figure 1-1a**). Upon completion of a layer, a motorised stage moves up in a single increment to allow the next layer to be photo-polymerised (Melchels, Feijen and Grijpma, 2010). In this manner 3D structures can be generated. Selective laser sintering functions in a similar manner, fusing particles in a powder bed layer-by-layer (**Figure**

1-1b). Between each later, a new layer of powder is spread across the surface. The unpolymerised powder acts as a support for the printed construct and can be later recycled (Kinstlinger *et al.*, 2016).

Fused deposition modelling is the process of melting and extruding thermoplastics through a small nozzle (**Figure 1-1d**). The rapid cooling of the thermoplastic upon extrusion allows 3D constructs to be fabricated layer-by-layer (Zein, Hutmacher, Tan and Teoh, 2002). Stereolithography, selective laser sintering and fused deposition modelling, however, are unable to directly incorporate cells into the 3D printed constructs in a single step, due to the unfavourable conditions.

3D bioprinting

The aforementioned 3D printing techniques do not allow the direct incorporation of cells into the printed constructs. Bioprinting is a subdivision of 3D printing in which cells are directly incorporated into the fabricated 3D structures and this ability to pattern cells and biomaterials in three dimensions presents a promising strategy for tissue engineering. There are three main bioprinting techniques: inkjet bioprinting, laser-assisted bioprinting, and extrusion-based bioprinting.

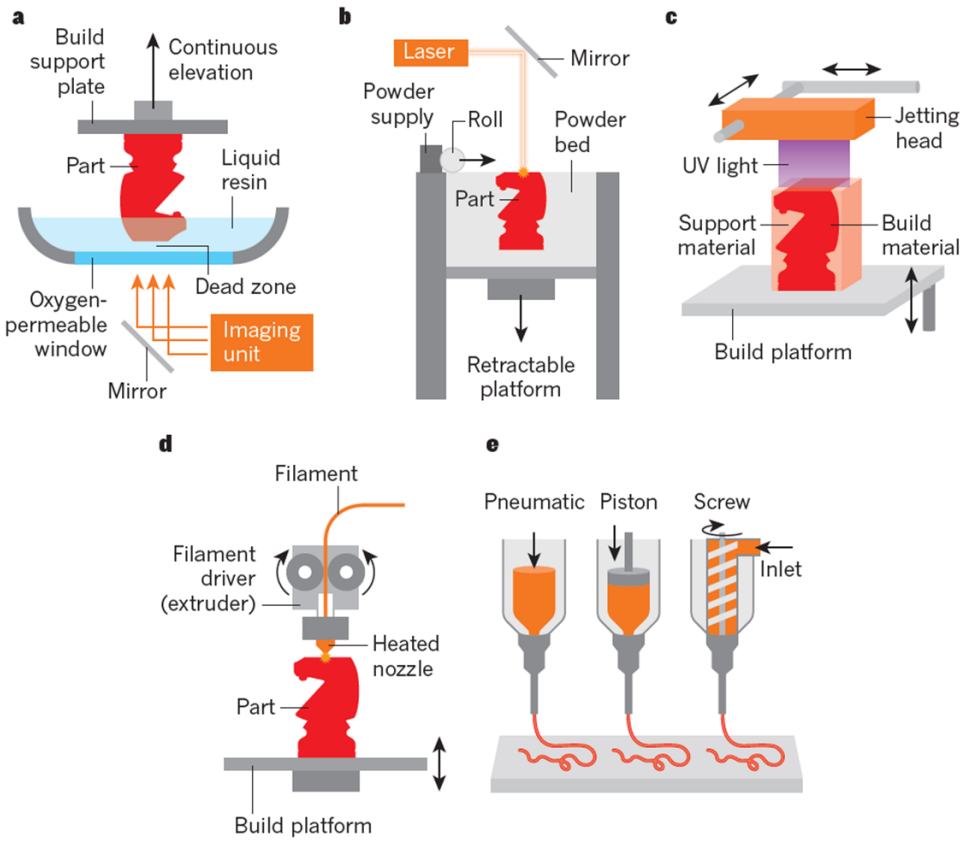

Figure 1-1 3D printing methods. Depictions of various 3D printing techniques including stereolithography (a), selective laser sintering (b), inkjet printing (c), fusion deposition modelling (d) and direct ink writing (e). Reproduced from (Truby and Lewis, 2016) with permissions from Springer Nature.

Inkjet bioprinting

During inkjet printing, droplets of bioink are dispensed to produce 3D structures in a layer-by-layer manner (**Figure 1-1c**). Inkjet bioprinters are low cost and high-speed. These droplet-on-demand printers dispense droplets of a controlled volume using thermal or acoustic systems. Thermal systems involve the local heating of the printhead to vaporise a

small volume of bioink. A small bubble is created and the change in pressure forces a droplet to be ejected (Seol *et al.*, 2014). The heating in the printhead is localised and short-lived, limiting damage to biological agents, such as cells (Xu *et al.*, 2005; Okamoto, Suzuki and Yamamoto, 2000; Xu *et al.*, 2006). Piezoelectric systems function by applying a deformation-inducing voltage to piezoelectric crystals, causing a droplet of the bioink to be ejected from the nozzle. Inkjet printing, however, has its limitations. Due to the droplet dispensing mechanism, the viscosity of the bioink must be low. As a result, the maximum cell density allowed is far lower than other printing methods, resulting in low cell encapsulation, thus limiting its use in many tissues and organs where the cell density is high, such as the liver and heart. Furthermore, due to the requirement of a small nozzle, this printing technique is liable to clogging (Nakamura *et al.*, 2010).

Laser-assisted bioprinting

Laser-assisted printing is the use of a laser to enable bioink to be transferred to another substrate. In laser-induced forward transfer, an absorbing layer is overlaid on a bioink layer. Application of laser energy to a specific coordinate on the absorbing layer induces the propulsion of a droplet of material from the underlying bioink layer (Koch, Gruene,

Unger and Chichkov, 2013; Guillotin *et al.*, 2010). This technique avoids clogging, and printed cells lack damage or loss of function (Guillotin and Guillemot, 2011). However this technique is laborious, slow and fabricates scaffolds with limited build height (Schuurman *et al.*, 2013).

Extrusion-based bioprinting

Extrusion-based bioprinters fabricate 3D structures by the direct deposition of continuous bioink strands through a small nozzle, in a layer-by-layer fashion (**Figure 1-1e**) (Malda *et al.*, 2013). Extrusion-based bioprinting is relatively affordable and one of the fastest bioprinting techniques. These two factors alone promote scalability. Extrusion-based bioprinting also facilitates the deposition of high viscosity bioinks, in addition to high cell densities, and the ability to produce porous constructs (Ozbolat and Hospodiuk, 2016; Bajaj *et al.*, 2014). In addition to this, the technique allows a variety of materials to be printed including, but not limited to, cell spheroids, microcarriers and decellularised ECM, alongside cell-laden hydrogels (Malda *et al.*, 2013; Pati *et al.*, 2014; Faulkner-Jones *et al.*, 2013; Levato *et al.*, 2014; Chung *et al.*, 2013).

However, extrusion-based bioprinting also has its drawbacks. The selection of bioink can be limited as they are typically required to possess

shear-thinning properties, and must possess suitable gelation properties to fabricate stable constructs. An example is ECM-like materials, such as collagen and Matrigel, whose viscosity is too low to allow fabrication of 3D structures without another supporting hydrogel. Cells also experience a considerable shear stress during extrusion, due to the forces at the wall of the nozzle. This is made greater when the nozzle is small, or the cell density is high (Chang, Nam and Sun, 2008). As a result, the resolution of this technique is poorer than other bioprinting techniques, and cannot be used to pattern individual cells in a specific manner. Despite these limitations, a number different approaches have been taken to improve this technique (**Figure 1-2**).

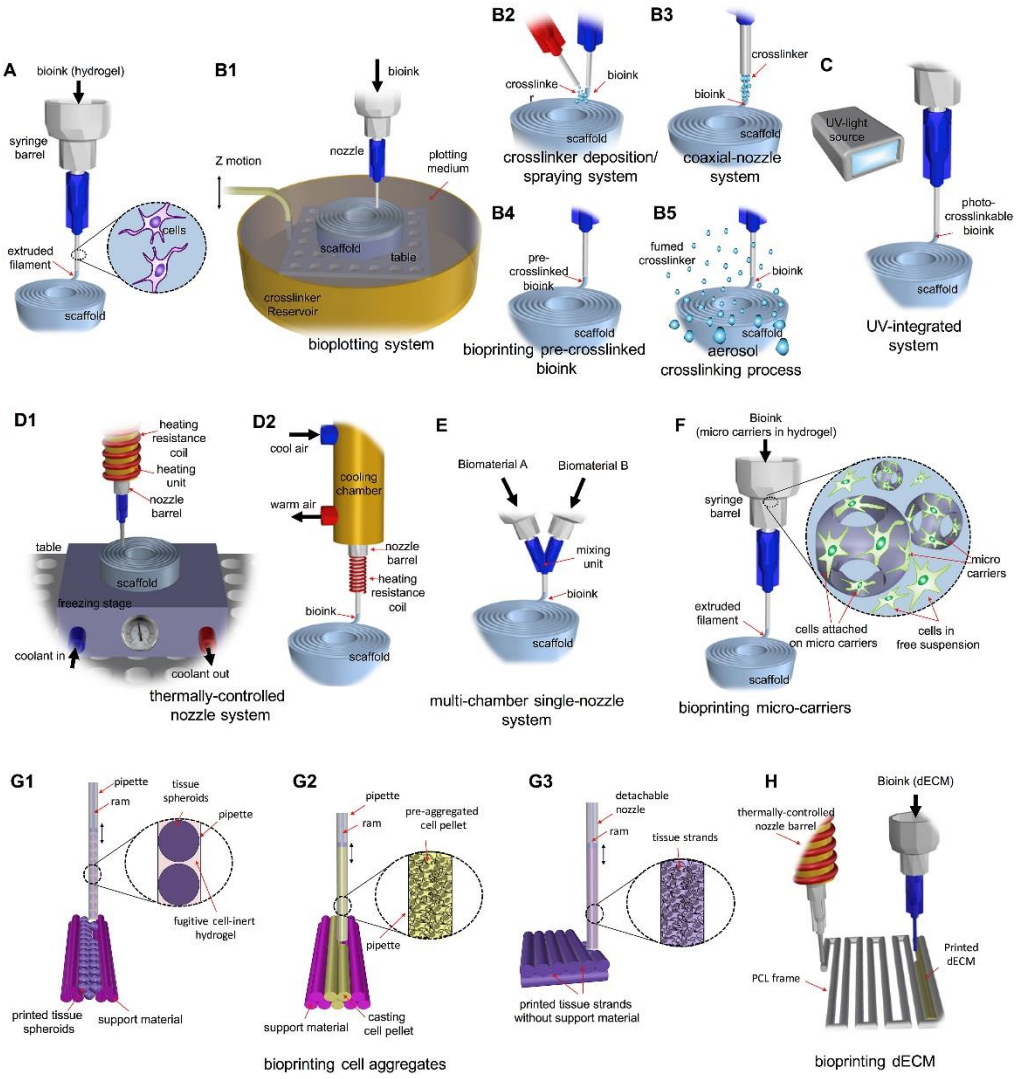

Figure 1-2 Extrusion-based bioprinting techniques. A) Direct extrusion of a cell-laden bioink. B1–B5) Methods to introduce crosslinker solutions during cell-laden bioink extrusion. C) Photo-crosslinking incorporation during cell-laden bioink extrusion. D1–D2) Thermal-assisted bioprinting. E) Multi-material bioink extrusion through a single nozzle. (F) Bioprinting of cell-loaded microcarriers via a facilitating bioink. G1–G3) Deposition of cell spheroids and pre-moulded strands. H) Co-printing of a cell-laden bioink with a thermoplastic support. Reproduced from (Ozbolat and Hospodiuk, 2016) with permission from Elsevier.

Coaxial bioprinting

One method of extrusion-based bioprinting uses a coaxial nozzle for strand deposition. In this method, two materials are simultaneously dispensed to produce strands, typically by co-perfusion of a crosslinking solution. Solid and hollow strands can be printed when the crosslinker solution is ejected through the shell and core needles, respectively, and commonly alginate, co-perfused with $CaCl_2$, is used as the printed ink (Zhang *et al.*, 2015; Zhang, Yu and Ozbolat, 2013; Gao *et al.*, 2015b; Colosi *et al.*, 2016a).

Core–shell bioprinting

If a cell-laden core is used, however, so-called "core–shell" strands can be fabricated. Core–shell strands in particular present an attractive approach to tissue engineering, as they mimic the morphology of many human tissues such as tendon, ligament, blood vessel, nerve and muscle. Furthermore, these strands allow for softer materials, which are unable to form porous constructs without additional support, such as collagen, decellularised ECM and Matrigel, to be printed into 3D structures. Core–shell fibres, with an ECM core and an alginate shell, have been fabricated with a microfluidic device (Onoe *et al.*, 2013). Whilst not printed, these fibres demonstrated that the cells cultured in the core could remain viable long-term, display tissue-like morphologies, and continued to

exhibit function during culture. These fibres were arranged into higher-order structures using a textile weaving machine. Core–shell bioprinting has been explored previously. Core–shell strands have been printed using a 16.7% (w/v) alginate shell (Akkineni, Ahlfeld, Lode and Gelinsky, 2016). These strands were printed with a cell-laden core, a variety of core materials were tried, including alginate, gellan gum, gelatine and collagen. However, due to the high concentration of alginate in the shell, which was used to provide sufficient viscosity for printing, these constructs required 1 h of crosslinking with 1 M $CaCl_2$. The group demonstrated good shape fidelity and interconnected pores for their 3D printed structures. Despite this, cell viability in the printed constructs was initially low, only 65%, increasing to 80% after 21 days of culture. Core–shell strands have also been fabricated with an alginate/gelatine shell with a cell-laden fibrinogen core (Dai *et al.*, 2017). These strands had an overall diameter of ~900 µm, with a variable core diameter (~240 – 530 µm), depending on the flow rate used. These strands were used to create 3D tumour models for studying the tumour microenvironment *in vitro*, and cell viabilities were above 90%.

Requirements of a 3D printed construct

Previous studies have tackled different aspects of bioprinted constructs: bioink selection, mechanical properties, vasculature and gradients (Patra and Young, 2016; Wu et al., 2016; Pekkanen, Mondschein, Williams and Long, 2017; Liu et al., 2017; Datta, Ayan and Ozbolat, 2017). However most of these techniques fail to incorporate all factors in a single printing step. For bioprinting the most important aspect of the process is maintaining cell viability. Cells are precious cargo that are required in order for the bioprinted construct to carry out its role. Therefore, the bioink must be tuned in order to complement cells. Many cell types, particularly those that have been differentiated are more delicate, and require gentler printing processes to ensure that the cells are viable and functional post-printing. Biomaterials for implantation must avoid generating an immunological response in the host species, therefore care must be given when selecting materials. The immunological response of current biomaterials has recently been reviewed (Cravedi *et al.*, 2017).

There are several key factors in the fabrication of a cell-laden construct using extrusion-based bioprinting, and these factors can be divided into bioink requirements and printing process requirements. First of all, the

printing process must be biocompatible (Murphy and Atala, 2014). Bioinks must allow cells to be incorporated within them and promote cell survival during the printing process. During the printing process, the shear stress experienced by the cells must be reduced, particularly in the nozzle, where narrowing increases the shearing force between the cells and the nozzle wall. Shear stress is a major determinant in cell viability post-printing (Skardal, Zhang and Prestwich, 2010). The resolution of the printed strands must allow the patterning of cell types to a degree suitable for the role of the printed construct. Vasculature is also important to incorporate in printed constructs, especially in the fabrication of thicker constructs (Lee et al., 2014). Where vasculature isn't possible, pores at least should be present to allow nutrient diffusion into the centre of large constructs. Crosslinking of the bioink must be cell compatible to minimise cell death or adverse effects such as mutagenesis. Post-printing, the printed scaffold must support the cell growth and function post-printing. For example, if the cells were undifferentiated stem cells, and the application was for cartilage repair, the material should contain motifs for cell binding and cell spreading and encourage differentiation towards chondrogenesis. The mechanical properties of the bioink and printed construct also play a role: the stiffness of the bioink will determine how the cells will respond, and how

their state of differentiation will change, and the mechanical properties of the printed construct must be able to withstand external mechanical forces, including *in vitro* and *in vivo* manipulation (Discher, Janmey and Wang, 2005).

Bioink selection

Hydrogels are typically the main component of a printable bioink in extrusion-based bioprinting. Hydrogels are polymer networks capable of trapping large volumes of water in a 3D structure. As a result, hydrogels provide an environment that simulates natural extracellular matrix and are considered the best material for encapsulating and culturing cells in (Malda *et al.*, 2013). In terms of bioprinting, hydrogels have several key factors that influence their printability and impact on cells, including gelation time, swelling/contraction, stability, and biocompatibility (**Figure 1-3**) (Murphy, Skardal and Atala, 2013).

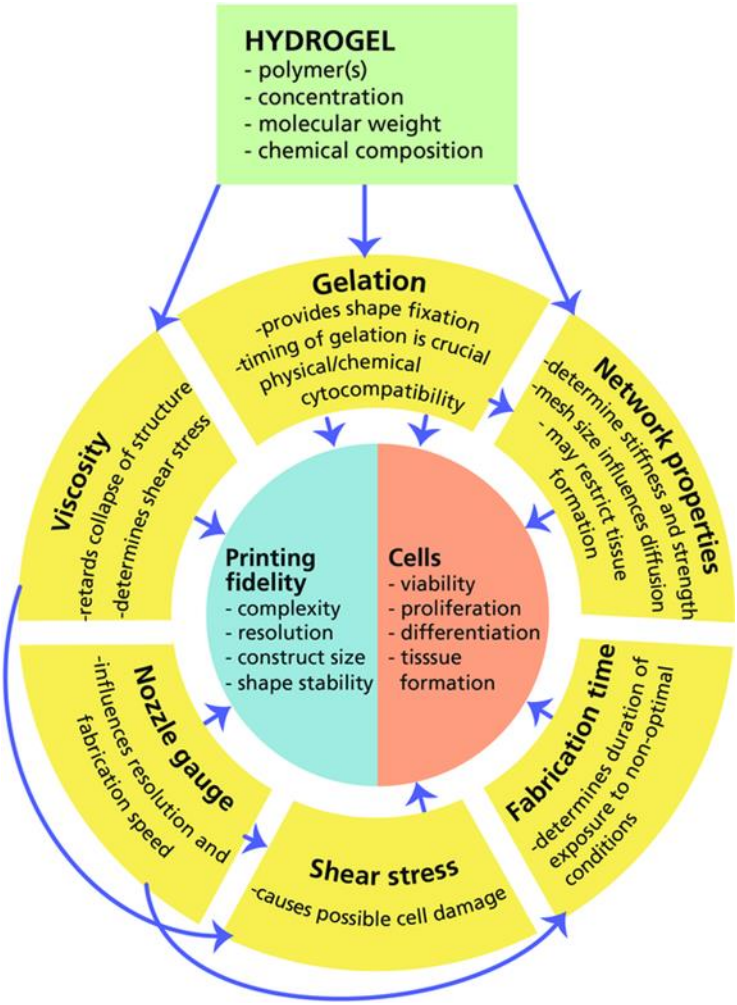

Figure 1-3 Key parameters to be considered when selecting hydrogels for bioprinting. Reproduced from (Malda *et al.*, 2013) with permission from Wiley.

Hydrogels can be synthesised or sourced from nature. Some natural polymers such as collagen, fibrin and gelatine contain motifs that allow cells to bind and spread, thus supporting their growth. Other commonly used natural hydrogels include agarose, chitosan and alginate do not have these motifs and require modification with RGD peptides in order to facilitate cell binding via integrin binding. Natural polymers also suffer

from batch-to-batch variability. On the other hand, synthetic polymers can be produced more reproducibly but typically lack motifs for cell binding. Synthetic polymers can be modified to include these motifs, such as RGD-peptide conjugation for example, in order to allow cells to bind via integrin receptors, and spread (Maher *et al.*, 2009). Common synthetic polymers include polyacrylamide and poly(ethylene glycol) (PEG). PEG is a synthetic polymer commonly used in tissue engineering. A major benefit of PEG, and other synthetic polymers, is their ability to be chemically manipulated in order to produce the optimal gelation kinetics and mechanical properties.

Alginate is a polysaccharide normally extracted from brown algae, but may also be synthesised bacterially (Remminghorst and Rehm, 2006). Alginate is widely used for drug and protein delivery, wound dressings and cell culture. Alginate chains are comprised of two main monomers, guluronic acid (G) residues and mannuronic acid (M) residues. Consecutive sequences of these monomers are referred to as "G-blocks" and "M-blocks", respectively. Alternating M and G residues are referred to as "MG-blocks". G-blocks can participate in ionic crosslinking with other G-blocks using divalent ions (**Figure 1-4a**). Commonly, calcium is selected as the ion of choice, however barium has also been used to

crosslink alginate. Alginate is biocompatible and typically has low immunogenicity, depending on its purity (Lee and Mooney, 2012). However, alginate is also bioinert and does not contain biological motifs that promote cell binding. Alginate may be modified with RGD peptides for general cell attachment, but another peptide, YIGSR, has been shown to specifically allow neural cell adhesion (Alsberg *et al.*, 2001; Dhoot, Tobias, Fischer and Wheatley, 2004). Degradation of alginate occurs via ion exchange, replacing the divalent ions in the egg-boxes with monovalent ions in physiology, typically sodium ions (Kong, Kaigler, Kim and Mooney, 2004). Degradation via ion exchange is slower than enzymatic degradation. Alginase, the enzyme that can cleave alginate chains, is not present in mammals (Lee and Mooney, 2012).

Gelatine is a natural polymer extracted from animal skins, through an acid or alkali wash process. The extracted gelatine is a thermo-responsive polymer that is liquid at 37°C and forms solid hydrogels when chilled. Gelatine is also comprised of denatured ECM, and intrinsically contains cell binding motifs and can be remodelled by cells. Gelatine can be modified with methacrylate groups to produce gelatine methacrylate. Via photo polymerisation, and in the presence of the correct photoinitiator, GelMA can be crosslinked into hydrogels which are stable

at 37°C (**Figure 1-4b**) (Schuurman *et al.*, 2013; Nichol *et al.*, 2010; Billiet *et al.*, 2014).

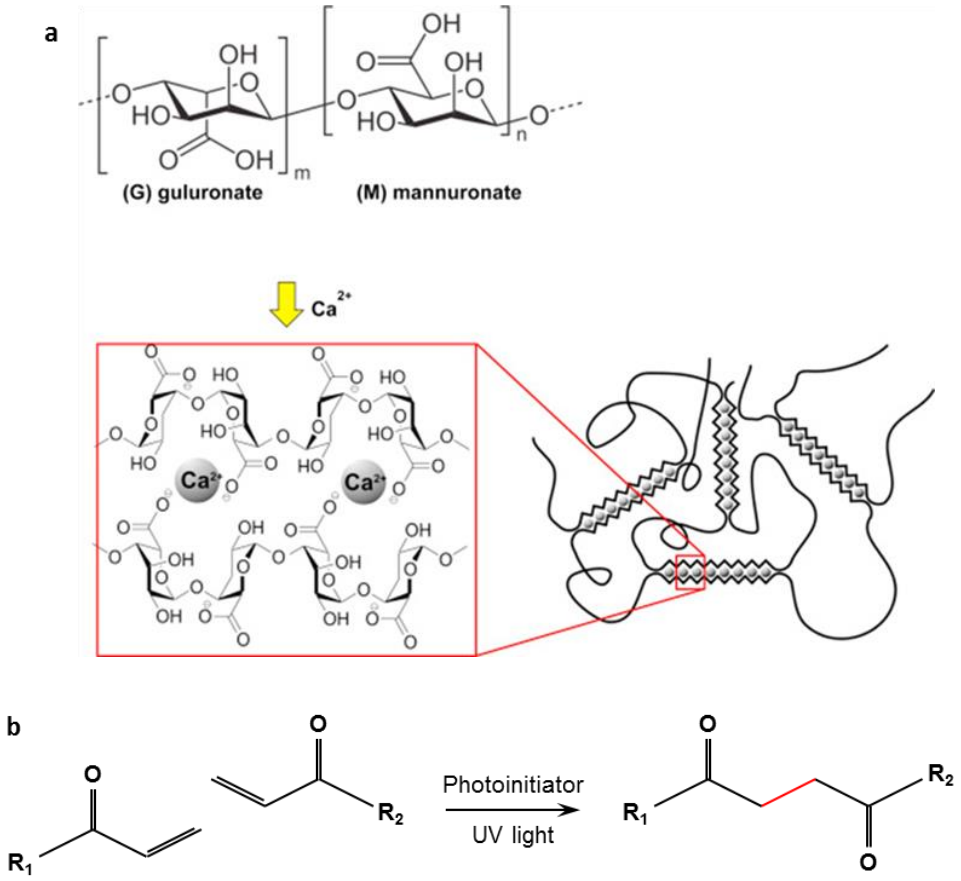

Figure 1-4 Hydrogel crosslinking mechanisms. a) Ionic crosslinking of alginate. Divalent ions, such as calcium, bind to negatively charged regions in G-blocks of alginate polymer chains. Reproduced from (Bruchel *et al.* 2015) with permission from Elsevier. b) Photocrosslinking of polymers containing acrylate groups. In the presence of UV light, and using a suitable photoinitiator, polymers containing acrylate groups can be crosslinked into stable hydrogels via free radical polymerisation.

Mechanical properties

The mechanical properties of the printed construct play an important role in determining how well it functions. In bioprinting, the bioprinted constructs are typically formed from hydrogels. Despite being suitable printable materials for cell encapsulation, hydrogels suffer due to their relatively weak mechanical properties, limiting their applications. The elastic moduli of hydrogels are typically found in the kPa range (Oyen, 2014). Popular hydrogels such as alginate are brittle, and cannot stretch beyond 1.2 times their original length (Okumura and Ito, 2001; Haraguchi and Takehisa, 2002). The fracture energies of such hydrogels, the energy dissipated upon fracture of the hydrogel, is ~10 J m^{-2}, which is magnitudes away from the physiological values of cartilage (~10^3 J m^{-2}), tendon, and ligaments (Adams, Kerin and Wisnom, 1998; Ambrosio, De Santis and Nicolais, 1998; Zhao *et al.*, 2014). Approaches to improve mechanical properties of hydrogels include double network hydrogels, nanocomposite hydrogels, sliding-ring hydrogels, macromolecular microsphere composite hydrogels, tetra-PEG hydrogels, and physical interaction enhanced hydrogels. Of these approaches, double network hydrogels have demonstrated fracture energies within physiological range, or greater (Gong, 2010).

Double network hydrogels are hydrogels composed of two polymer networks. The first network, formed from densely crosslinked short chain polymers, is rigid, whilst the second network, formed from sparsely crosslinked long chain polymers, is ductile. The two networks work together to provide toughness and stretchability. When stretched, energy is dissipated by the breaking of crosslink in the first network. The hydrogel maintains intact due to crosslinks in the second network and, as a result of the long polymer chains in the second network, is able to stretch by a great proportion. Upon release, the gel is able to shrink back to its original length as a result of crosslinks in the first network reforming (Chen, Chen, Zhu and Zheng, 2016b; Gong, 2010). Recently, a biocompatible double network hydrogel has been used to encapsulate cells, and was subsequently bioprinted (Hong *et al.*, 2015). Whilst toughness was improved and the hydrogel had excelled shape recovery, the hybrid hydrogel lacked the biological properties for optimal cell survival and function.

Vasculature

For the eventual fabrication of organs, incorporation of vasculature into bioprinted constructs is essential. Bioprinting of vascularised constructs has recently been reviewed (Datta, Ayan and Ozbolat, 2017). There have

been many approaches, either to directly incorporate micro channels during the printing process, using sacrificial inks, or to induce angiogenesis or neovascularisation (Miller *et al.*, 2012; Kolesky *et al.*, 2014; Wu, Deconinck and Lewis, 2011). Printing interconnected pores provides constructs with nutrient diffusion, especially in thick constructs. When implanted, pores within constructs also allow for the infiltration of vasculature. Many studies have used Pluronic F-127 as a sacrificial ink (Kolesky *et al.*, 2014; Wu, Deconinck and Lewis, 2011). Pluronic F-127 has limitations in bioprinting due to the requirement of lowering the temperature to 4°C in order to liquefy the ink, and despite being FDA approved (Diniz *et al.*, 2015), high concentrations of Pluronic F-127 have been shown to be cytotoxic to certain cell types (Khattak, Bhatia and Roberts, 2005).

Gradients

Many parts of the body contain gradients, and these gradients are essential for the maintenance of homeostasis, driving cell differentiation, migration and proliferation. In the body different types of gradients can be found including, but not limited to, pore gradients, stiffness gradients and biochemical gradients. Natural ECM is porous, and these pores are distributed heterogeneously (Hutmacher, 2000; Loh and Choong, 2013).

Pores provide space for cell attachment, allow nutrient exchange and allow for vascular infiltration. 3D printing has been used to produce scaffolds with a gradient of pores, however, bioprinting porous gradients has yet to be shown (Woodfield *et al.*, 2004; Sobral *et al.*, 2011). Cells have been well characterised to differentiate along a gradient of stiffness (Engler, Sen, Sweeney and Discher, 2006; Murphy, McDevitt and Engler, 2014; Wells, 2008; Discher, Janmey and Wang, 2005). Gradients of elastic modulus have been prepared by photo-crosslinking hydrogels for varying times (Wong, Velasco, Rajagopalan and Pham, 2003; Kloxin, Benton and Anseth, 2010). Other studies have used multiple printheads to produce graded and heterogeneous constructs (Kolesky *et al.*, 2014; Schuurman *et al.*, 2011; Pati *et al.*, 2014; Liu *et al.*, 2017; Hardin, Ober, Valentine and Lewis, 2015).

Thesis aims

In summary, despite these significant advances in bioprinting using cell-laden strands, a remaining challenge is the bioprinting of tissue-relevant architectures using strands that combine biological and mechanical properties.

This thesis aims to explore coaxial bioprinting to combine mechanical properties with biological properties in a single cell-laden core–shell strand which better mimics *in vivo* tissues. The shell material will be comprised of a mechanically robust hydrogel based on alginate, and the core will be comprised of an ECM-like material, which can support cell growth and function.

The work of this thesis is divided into three main objectives:

- To characterise the mechanical properties of hybrid hydrogels composed of PEGDA and alginate, examining the impact of hydrogel composition, PEGDA molecular weight and swelling on the strength, modulus and failure strain of the hybrid hydrogels.
- To develop a coaxial printing technique that allows the co-extrusion of cell-laden core–shell strands. The hybrid

PEGDA/alginate hydrogel will be used as the shell material and live cells will be incorporated into the core of the strands. The long-term viability and function of the cells will be assessed.

- To incorporate gradients into the shell of the bioprinted core–shell strands. Two type's gradients will be examined: gradients of stiffness and gradients of soluble factors. The longevity of these gradients within printed structures will be assessed.

Chapter 2 – Materials and methods

The following chapter details the materials and methods used to generate the data found in the later chapters of this thesis.

Materials

An exhaustive list of chemicals/reagents and equipment can be found in **Appendix A**.

Buffers

HEPES-buffered saline

The buffer was prepared as a 10× stock solution. 1.5 M NaCl, 0.25 M HEPES and phenol red were dissolved in diH_2O. The pH was adjusted to 7.4 using NaOH and HCl, and the solution was autoclaved and stored at RT. To produce a 1× working solution, 1 volume of 10× HBS was filtered through a 0.2 µm filter and then diluted with 9 volumes of diH_2O.

10× PBS

10 PBS tablets were dissolved in 100 mL diH_2O. The solution was filtered through 0.2 µm filter, autoclaved, and stored at 4°C until required.

Calcium crosslinking buffer

100 mM $CaCl_2$ was prepared in 1× HBS. The pH was adjusted to 7.4 using NaOH and HCl, autoclaved, and stored at RT.

GelMA synthesis

GelMA was prepared using a modified protocol as described previously (Van Den Bulcke *et al.*, 2000; Nichol *et al.*, 2010). Briefly, a 10% (w/v) HB gelatine solution was prepared in PBS and stirred at 100 rpm at 50°C for 1 h, at which the gelatine had fully dissolved. The stirring was increased to 400 rpm and methacrylic anhydride was added at a rate of 0.5 mL min^{-1}, to a final concentration of 8% (v/v). The reaction was protected from light and was allowed to continue at 50°C and 400 rpm for 3 h. After this time, the reaction volume was diluted 1:4 in PBS (preheated to 80°C) to quench the reaction. The reaction was stirred at 400 rpm for a further 30 min. The reacted material was dialysed, through an 8 kDa cut-off cellulose dialysis membrane (BioDesign Inc. of New York, USA), against 3-4 volumes diH_2O for 7 days to remove any unreacted methacrylic anhydride and acidic by-products. The dialysis water was changed three times per day. The dialysed product was pooled and filtered through a 40 µm nylon sieve. The final product was freeze-dried (Modulyo®; Thermo Fischer Scientific, UK) and stored at −80°C until required. The degree of methacrylation was confirmed using ^{1}H NMR (**Figure 2-1**).

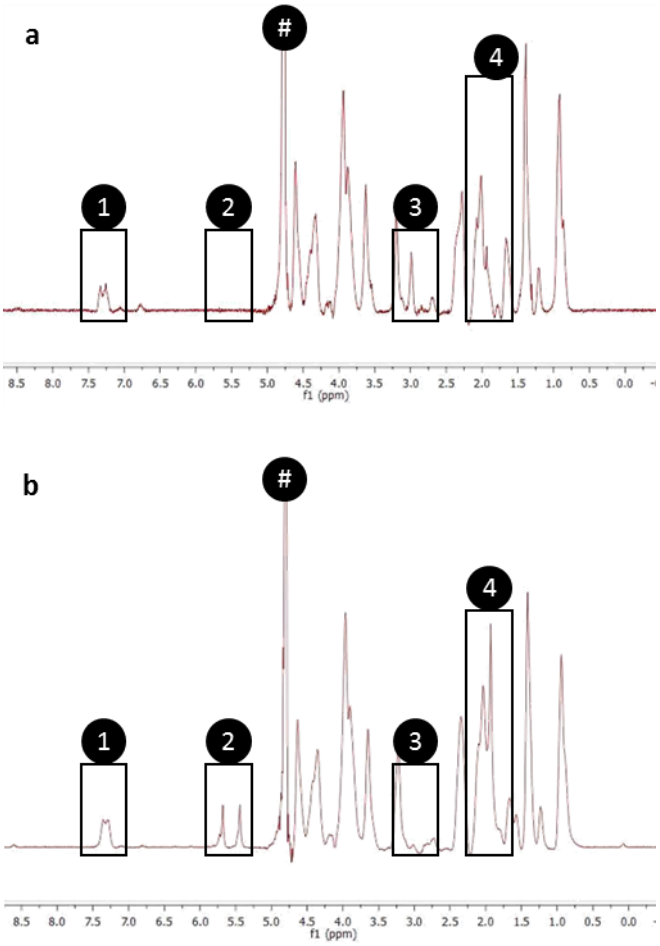

Figure 2-1 NMR spectra confirming methacrylation of gelatine. The methacrylation of gelatine was confirmed using ^{1}H NMR, recorded in D_2O. Spectra of gelatine (a) and GelMA (b) are shown (both at 10 mg mL^{-1}). Selected regions have been marked on both spectra showing signals for the aromatic group (1), the methacrylate vinyl group (2), lysine group (3), the methyl group (4), and D_2O (#).

Methods

Preparation of hydrogel solutions

Alginate

Alginate solutions were prepared by dissolving alginate powder in a deionised water. An appropriate mass of alginate powder was added as a single layer on top of the required volume of water. The solution was rapidly vortexed at maximum speed to produce an even suspension. The suspension was left to mix on a roller mixer at 37°C overnight (minimum 16 h). Alginate solutions were stored at 4°C for up to 5 days.

PEGDA

I-2959 was dissolved at 80°C in dH_2O at a final concentration of 0.1% (w/v). A suitable mass of PEGDA was added to produce the desired % (w/v) concentration, and vortexed at maximum speed until fully dissolved. The suspension was left to mix on a roller mixer at 37°C overnight (minimum 16 h). The solution was then centrifuged (400 g_n; 5 min; RT) to remove any air bubbles.

PEGDA/alginate hybrids

I-2959 or LAP were dissolved at 80°C in diH_2O at a final concentration of 0.1% (w/v) or 0.17% (w/v), respectively. Alginate and PEGDA were added to produce the desired % (w/v) concentrations, without exceeding a total

hydrogel concentration of 11% (w/v), and vortexed at maximum speed to produce a homogenous suspension. The suspension was left to mix on a roller mixer at 37°C overnight (minimum 16 h). The solution was then centrifuged (400 g_n; 5 min; RT) to remove any air bubbles.

Gelatine

LB gelatine was dissolved in diH_2O, pre-warmed to 80°C, to produce a 6% (w/v) solution. The suspension was vortexed at maximum speed until the gelatine had completely dissolved. The solution was then centrifuged (400 g_n; 5 min; RT) to remove any trapped air bubbles. The pH was adjusted to 7.4 and the solution was autoclaved and stored at RT.

GelMA

I-2959 or LAP were dissolved at 80°C in the appropriate solvent at a final concentration of 0.1% (w/v) or 0.17% (w/v), respectively. The required mass of GelMA was weighed out and added to the photoinitiator solution. The suspension was vortexed at maximum speed until fully mixed. The suspension was left to mix on a roller mixer at 37°C overnight (minimum 16 h). The solution was then centrifuged (400 g_n; 5 min; RT) to remove any trapped air bubbles. The pH was adjusted to 7.4 prior to use. GelMA solutions were stored at 4°C for up to 2 days.

Preparation of hydrogels for bioprinting

Alginate

Alginate was printed as a partially crosslinked hydrogel. 6 mL 3% (w/v) alginate and 3 mL of 51 mM $CaCl_2$ were loaded into separate 10 mL syringes. The two syringes were connected using a butterfly connector (Qosina, USA). Beginning by pushing the $CaCl_2$, the two materials were rapidly syringe mixed for a minimum of 100 depressions of the plunger. The partially crosslinked gel was left for up to 30 min prior to printing.

GelMA

GelMA solution was heated and maintained at 37°C prior to use. The solution was added directly to cell pellets and the cells were gently resuspended.

Collagen

Collagen was prepared on ice, using ice-cold reagents, according to manufacturer's guidelines. The volumes of each reagent required were calculated using the following equations:

$$10X\ PBS\ volume = \frac{Final\ volume}{10}$$

$$Collagen\ volume = Final\ volume \times \frac{Final\ collagen\ concentration}{Stock\ collagen\ concentration}$$

$$NaOH\ volume = Collagen\ volume \times 0.0023$$

$$Media\ volume = Final\ volume - (10X\ PBS\ volume + Collagen\ volume + NaOH\ volume)$$

To prepare the collagen solution, 1 M NaOH and 10X PBS were added to the appropriate cell culture media. The solution was mixed well using a pipette and then collagen was added. The solution was mixed again and left on ice prior to cell preparation. The collagen solution was added directly to the cell pellet and, using a wide-bore pipette tip, the cells and collagen were mixed gently until a homogenous suspension was achieved.

Matrigel

Matrigel was thawed for 24 h on ice at 4°C. The Matrigel was aliquoted into 1 mL microcentrifuge tubes and stored at −20°C. Aliquots were thawed on ice when required. The thawed Matrigel was used undiluted and pipetted directly onto the cell pellet. Using a wide-bore pipette tip, the cells and Matrigel were mixed gently until a homogenous suspension was achieved.

3D printing

Core-shell printing

Core-shell strands were extruded through a tailor-made 27G/18G (ID/OD) coaxial needle (ramé-hart instrument co., USA). A schematic of

the needle can be found in Appendix A. The needle was attached to a commercial 3D bioprinter (3DDiscovery™; RegenHu, Switzerland) for layer-by-layer deposition. A diagram of the printing setup can be found in **Figure 2-2a**. Syringe pumps (WZ-74905-04; Cole-Parmer, UK) were used as the driving force for material extrusion, and the flow rates of the core and shell materials were fixed at 0.01 mL min^{-1} and 0.1 mL min^{-1}, respectively. The shell material was loaded into a 10 mL syringe barrel and connected to the outer needle via 1.6/4.8 mm (ID/OD) tubing (Z685593; Sigma-Aldrich, UK). The core material was loaded into 10 mL cartridges (7012114; Nordson EFD., UK).

In order to allow simultaneous dispensing of the core and shell materials, two syringe pumps had to be used in conjunction with the 3D bioprinter. These syringe pumps had to be placed at a distance from the 3D bioprinter due to physical constraints (see **Figure 2-2b** to see positioning). To connect the syringe to the coaxial needle, long tubing was required to cover this distance. This increased the volume of core material required and, as the flow rate was 0.01 mL min^{-1}, pressure could not be conveyed to the needle tip, preventing dispensing of the core material. To convey pressure from the core syringe to the coaxial needle, and also to minimise the volume of core material required, a liquid-phase was used as the driving mechanism for core material dispensing. A liquid

phase of PBS was used to convey pressure from the syringe pump, along the length of tubing, to a cartridge. The liquid-phase was separated from the core material via a piston (**Figure 2-2c**), which in turn allowed the dispensing of core material when the liquid-phase was compressed.

The core and shell materials were printed at 5°C and RT, respectively, and the printhead movement speed was fixed at 3 mm s^{-1}. The core material was cooled using a cartridge cooler. Scaffolds were drawn using BioCAD™ software (Version 1.0; RegenHU, Switzerland). Imported CAD files were converted to G-code using MM Converter™ software (Version 1.0.0.6; RegenHU, Switzerland).

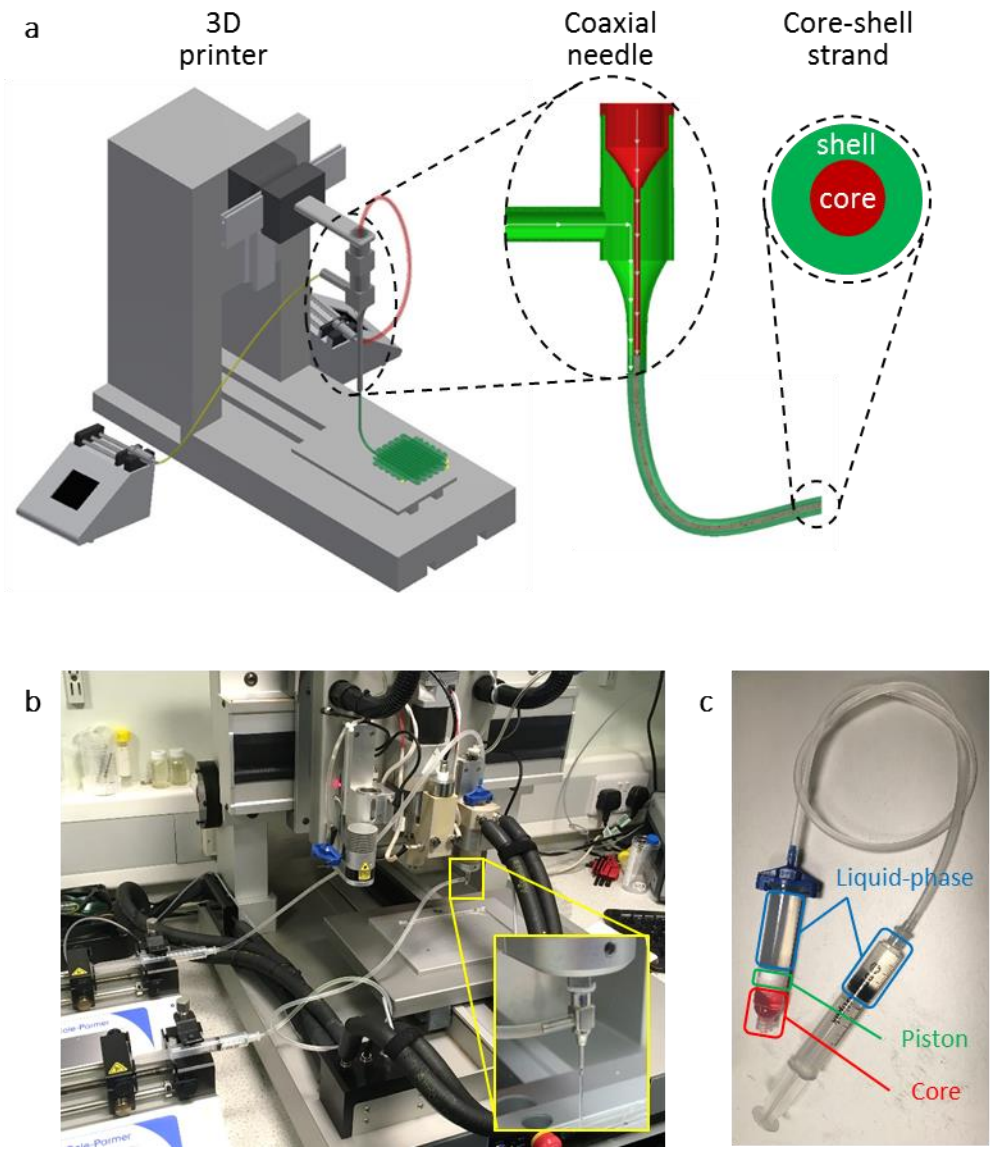

Figure 2-2 Core–shell printing setup. (a) Schematic of the bioprinting setup, showing the 3D printer, coaxial needle and core–shell strand. (b) Image of the actual printing setup. Inset: close-up view of the coaxial needle with a strand being extruded. (c) Core material printing system.

Gradient printing set up

Gradient printing was performed using the coaxial needle and two syringe pumps. The setup is shown in **Figure 2-3**. Two materials were simultaneously accelerated and decelerated through the outer part of the coaxial needle to produce a gradient strand. Each materials was loaded into a 10 mL syringe and place on a syringe pump. One syringe pump was programmed to accelerate from 0 mL min^{-1} to 0.1 mL min^{-1}, whilst the other syringe pump was programmed to simultaneously decelerate from 0.1 mL min^{-1} to 0 mL min^{-1}. By altering the acceleration and deceleration of the flow rates, different gradients could be obtained. In all experiments, the magnitude of acceleration and deceleration were set to the same values. The acceleration and deceleration was varied from 6.3 µL min^{-2} to 6000 µL min^{-2}. The two syringes were connected using tubing (Z685593; Sigma-Aldrich, UK), connected with a Y-shaped connector (Qosina, USA) at the terminal end. A shorter length of tubing was used to connect the Y-shaped connector to the outer needle.

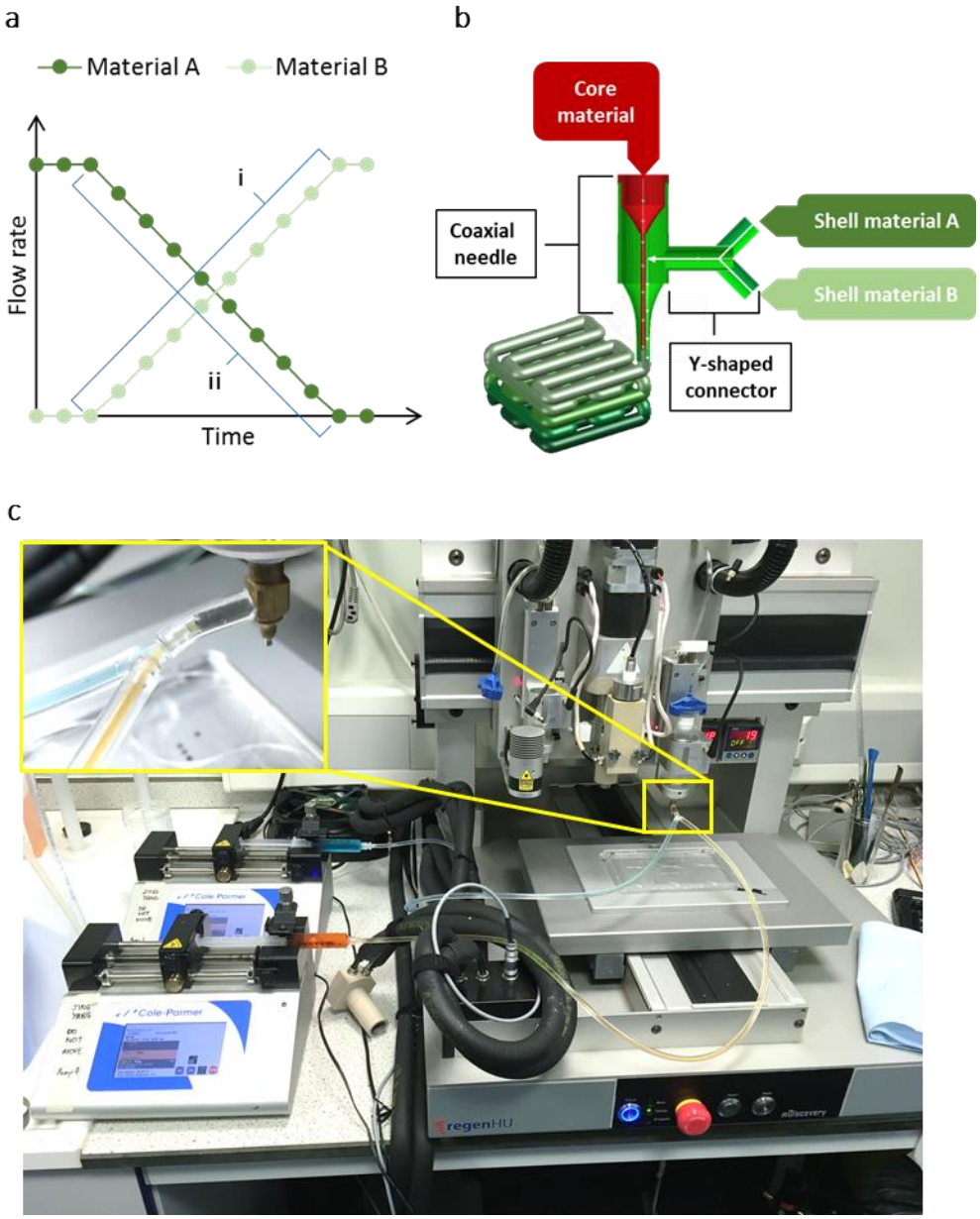

Figure 2-3 Gradient printing setup. (a) Graph showing how gradients could be fabricated by controlling flow acceleration (i) and flow deceleration (ii). (b) Schematic of a printed gradient construct showing the inputs of each material. (c) Image showing the actual gradient setup. Inset: close-up of the coaxial needle with a Y-shaped connector attached to the outer needle for gradient fabrication.

Printed construct crosslinking

Constructs containing alginate were crosslinked in calcium crosslinking buffer. The constructs were then washed in αMEM containing 1% (v/v) AB/AM. Constructs containing I-2959 were crosslinked using UV light (365 nm, 15 W (Blak-Ray® XX-15L UV Bench Lamp; Ultra-Violet Products Ltd, UK) at a distance of 35 mm. Constructs containing LAP were crosslinked using visible light (365 nm, 15 W (Blak-Ray® XX-15L UV Bench Lamp; Ultra-Violet Products Ltd, UK) at a distance of 35 mm.

Hydrogel characterisation

Mechanical testing

Mechanical testing was performed using a Texture Analyser HD Plus (Stable Microsystems, USA) fitted with a 5 kg load cell. A 32 mm diameter cylindrical aluminium probe was used for compression testing. Tensile grips were used for tensile testing. The deformation rate for both types of test was fixed at 0.5 mm s^{-1}. Stress–strain curves were plotted from the mechanical testing data, from which strength, elastic modulus and failure strain could be obtained. The maximum stress prior to failure was taken as the strength. The strain at this point was taken as the failure strain. Elastic modulus was obtained by calculating the gradient of a linear trendline fitted to the data in the strain region of 0 – 0.1.

Rheology

Viscosity measurements were performed using a MCR301 rheometer (Anton Paar, UK) in rotational mode. Shear rate sweeps were performed with a 25 mm cone plate (cone angle 1°). The shear rate was increased from 0 to 1000 s^{-1}, whilst the temperature was kept constant at 20°C. Gelatine and gelatine methacrylate were loaded onto the plate at 37°C and then chilled to 20°C for 10 min prior to testing.

Cell culture

Unless specified otherwise, all cells were cultured in a humidified incubator at 37°C with 5% CO_2, and expanded in 2D. All cell culture was performed in a Class II biosafety cabinet. Cell passage was typically performed once cells had achieved a specified confluency (see **Table 2-1** for individual cell type details) using media and reagents pre-warmed to 37°C.

Thawing

Cryopreserved cells were thawed in a 37°C water bath until a small ice crystal remained. The cell suspension was slowly pipetted in a drop-wise manner into 5 mL of the appropriate pre-warmed cell culture media and centrifuged at the appropriate speed and time. The supernatant was

decanted and discarded, and the cells were resuspended in the appropriate cell culture media at the recommended density.

Passaging

Cells were first washed twice in PBS. Next, 3 mL of trypsin or Accutase was added, and the cells were incubated at 37°C for a maximum of 5 min or 10 min, respectively. Cell detachment was validated by light microscopy. 12 mL of culture media was added to quench the enzymatic reaction. The cell growth surface was gently washed to ensure maximal cell retrieval. Cells were centrifuged at the appropriate speed and time. The supernatant was decanted and the cell pellet was resuspended as required. For subculture, the cells were resuspended in the appropriate cell culture media and divided as required.

Cryopreservation

Cells were harvested as described above. The cell pellet was resuspended in FBS containing 10% (v/v) DMSO at a density of 1×10^6 cells mL^{-1}. The cell suspension was aliquoted into cryovials and placed in a CoolCell® LX cell freezing container (BioCision, USA) and stored at −80°C overnight. The cryovials were then transferred to the vapour phase of liquid nitrogen (−150°C) for long-term storage.

Table 2-1 Cell culture conditions.

Cell type	Source	Maximum passage	Passage frequency, split	Centrifuge settings	Culture media composition
3T3 mouse fibroblasts (3T3 cells)	NIH	80	3 / week, 1 in 10	5 min, 180 g_n	DMEM, 9% (v/v) FBS, 2 mM L-glutamine, 1% (v/v) AB/AM
HepG2 Hepato-carcinoma (HepG2)	ATCC	20	2 / week, 1 in 4	5 min, 180 g_n	MEME, 10% (v/v) FBS, 4 mM L-glutamine, 1% (v/v) NEAA, 1% (v/v) AB/AM
Human umbilical vein endothelial cells (HUVECs)	PromoCell	5	1-2 / week, 1 in 4	5 min, 200 g_n	Endothelial medium, 1% (v/v) AB/AM
Immortalised human mesenchymal stem cells (ihMSCs)	Lonza (immortalised in-house)	25	1-2 / week, 1 in 4	5 min, 200 g_n	αMEM, 10% (v/v) FBS, 2 mM L-glutamine, 1% (v/v) NEAA, 1% (v/v) AB/AM
Rat hepatic stellate cells (RHSCs)	Freshly isolated from female rats	N/A	N/A	15 min, 500 g_n	DMEM, 10% (v/v) FBS, 2 mM L-glutamine, 1% (v/v) AB/AM

Cell characterisation

IgG ELISA

All media samples were stored at −80°C prior to ELISA. Media samples were thawed on ice and centrifuged at 10,000 g_n for 10 min at 4°C to pellet any cells and/or debris. IgG ELISA was performed on the supernatants according to manufacturer's guidelines.

Insulin ELISA

All media samples were stored at −80°C prior to assay. Media samples were thawed on ice and centrifuged at 10,000 g_n for 10 min at 4°C to pellet any cells and/or debris. Insulin ELISA was performed on the supernatants according to manufacturer's guidelines.

LIVE/DEAD staining

LIVE/DEAD staining was performed according to manufacturer's guidelines. Vials containing stock calcein-AM and ethidium homodimer-1 were briefly centrifuged at 16,000 g_n for 10 s and subsequently diluted in the appropriate cell culture media at final concentrations of 2 µM and 4 µM, respectively. Samples were removed from incubation and spent media was removed. The samples were washed once in fresh culture media before the working LIVE/DEAD solution was added. The samples were incubated at 37°C for a minimum of 20 min. The samples were

washed in fresh culture media and imaged using fluorescence or confocal microscopy. Quantification of staining was performed by analysing fluorescent images using ImageJ (Version 1.51q; National Institute of Health, USA).

PrestoBlue assay

PrestoBlue assay was performed according to manufacturer's guidelines. Briefly, stock PrestoBlue solution was diluted in the appropriate cell culture media to form a 10% (v/v) working solution. Spent media was removed from the cells/constructs and the working PrestoBlue solution was added. Samples were incubated at 37°C for 1 h. 100 µL samples were taken from each media and the fluorescence at 560/590 (Ex/Em) using a microplate reader. Working PrestoBlue solution was used as a blank and was subtracted from all values.

Microscopy

Optical and fluorescent microscopy

Both optical and fluorescent images were taking using a Leica DBRBE inverted microscope (Leica Microsystems, UK).

Confocal microscopy

Macro confocal images were taken using a Leica TCS LSI Large Scale microscope (Leica Microsystems, UK).

Scanning electron microscopy

Samples were frozen at –80°C and then freeze-dried (Modulyo®; Thermo Fischer Scientific, UK). Dried samples were gold sputter coated (EM SCD005; Leica Microsystem, UK) and SEM images were taken using a JEOL 6060LV SEM (JEOL USA, Inc., USA).

Data analysis

Image analysis

Image analysis was carried out using ImageJ software (Version 1.51q; National Institute of Health, USA).

Statistics

Statistical analysis was performed using Prism 7 for Windows (Version 7.0; GraphPad Software, Inc.). One-way ANOVA with Tukey post-hoc tests were performed using $\alpha = 0.05$.

Chapter 3 – A mechanically robust hybrid hydrogel ink for bioprinting

Introduction

In order to successfully 3D print core–shell strands with a biologically active, ECM-like, cell-laden core, a hybrid shell material that is mechanically robust will be used. In this chapter, the mechanical properties of a PEGDA/alginate hybrid material will be assessed.

Hydrogels are popular materials as they have many potential uses; however they are limited by their poor mechanical properties, especially when in direct comparison to solid polymers such as poly(caprolactone) and poly(lactic-co-glycolic acid). The combination of hydrogels has been a proven approach to markedly improve their mechanical properties (Sun *et al.*, 2012; Hong *et al.*, 2015; Gong, Katsuyama, Kurokawa and Osada, 2003; Czarnecki, Rossow and Seiffert, 2016; Naficy *et al.*, 2013; Li, Illeperuma, Suo and Vlassak, 2014; Yasuda *et al.*, 2005). Alginate, whose hydrogels are relatively brittle and have limited flexibility, has been shown to improve its stretchability and toughness when mixed with polyacrylamide. For this hybrid hydrogel, it was suggested that when force was applied to the hydrogel, the ionic bonds from the alginate crosslinking could "unzip", allowing the hydrogel to stretch. The covalent

crosslinks and long chains of the polyacrylamide allowed the hydrogel to stay together. Upon dissipation of the force, the ionic bonds would re-form as the hydrogel shrank back to its original length. One such paper has demonstrated the printing of an alginate hybrid hydrogel (Hong *et al.*, 2015). However, whilst the hydrogel was mechanically robust, it did not provide an ECM-like environment for cell growth.

The mechanical properties of hydrogels bioinks are important for many reasons including, but not limited to, matching native tissues' mechanical properties and forming stable structures after extrusion (Oyen, 2014). The preparation of these hydrogels must also be biocompatible in order to safely allow cell incorporation. PEGDA has been chosen in order to expand on the work on double network hydrogels containing PEGDA and alginate, carried out by Hong *et al.* 2015. PEGDA is a biocompatible hydrogel with the ability to covalently crosslink into a stable hydrogel under biocompatible conditions, allowing its use with living cells. Furthermore, it is possible to synthesise the base PEG molecules with specific chain length (which can then be used to synthesis PEGDA), allowing us to investigate if the molecular weight of PEGDA impacts the properties of the double network hydrogel.

This chapter of work seeks to explore PEGDA as a possible polymer to improve the mechanical properties of alginate, in order to create a mechanically-robust hydrogel with improved strength, stretchability and resilience. Alginate will be combined with PEGDA in three compositions, using two MW of PEGDA, and the mechanical properties of the hybrid hydrogel will be characterised. The impact of swelling on the mechanical properties will also be assessed. A single hybrid hydrogel composition will be chosen, one which displays the most stretchability and retains the most of its mechanical properties. The role of the hydrogel will be used as a shell material for 3D printing of cell-laden core-shell strands (see **Chapter 4**).

Experimental design

Preparation of cast hydrogels

PEGDA, alginate and PEGDA/alginate hybrid solutions were prepared as described in Chapter 2. Pure alginate hydrogels were prepared by first pre-crosslinking the alginate solution with a 1% (w/v) $CaSO_4$ slurry in diH_2O via syringe mixing. The ratio of alginate to $CaSO_4$ was fixed at 1:0.1328. The solution was immediately poured into a dumbbell-shaped mould, sealed with a glass slide, and left to polymerise for 5 min. The mould was then immersed in a bath of 100 mM $CaCl_2$ for up to 30 min to fully crosslink the alginate. A schematic of the dumbbell-shaped mould is shown in **Figure 3-1**.

Pure PEGDA hydrogels were prepared by pouring PEGDA solutions (containing I-2959) into the dumbbell-shaped mould. A glass slide was used to seal the top of the mould, and the mould was exposed to UV light for 10 min.

PEGDA/alginate hybrid hydrogels were prepared by pouring PEGDA/alginate solutions (containing I-2959) into the dumbbell-shaped mould. A glass slide was used to seal the top of the mould, and the mould was exposed to UV light for 10 min to crosslink the PEGDA. The

mould was then immersed in a bath of 100 mM $CaCl_2$ for up to 30 min to crosslink the alginate.

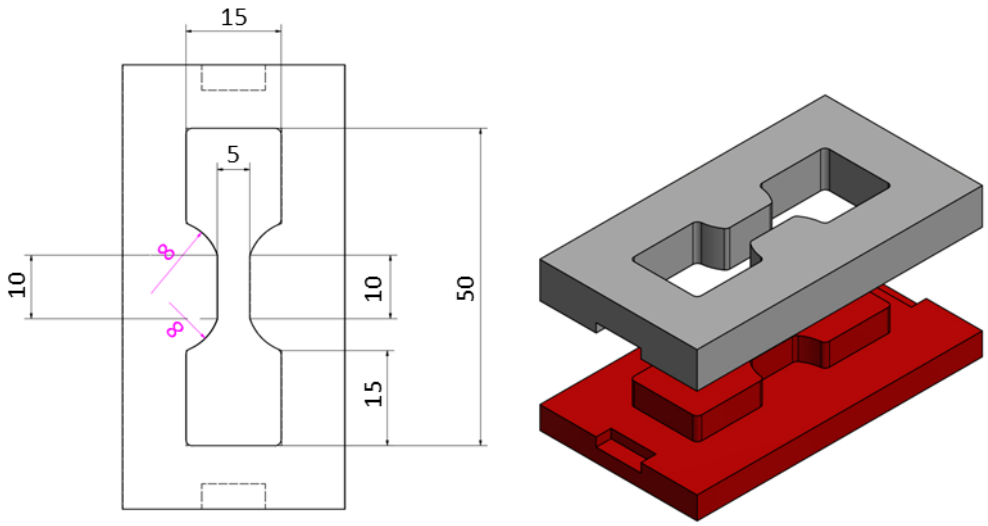

Figure 3-1 Schematic of the dumbbell-shaped mould. A PTFE mould was used to cast hydrogels. A glass slide was used to seal the top of the mould. The depth of the hydrogels was 3 mm. All dimensions are in mm.

Tensile testing of cast hydrogels

Cast hydrogels gently dabbed with paper towel to remove any surface liquid. The "arms" of the samples were wrapped in paper towel to improve grip with the tensile grips, and also to prevent premature fracturing of the hydrogels during the loading process. Samples were gripped parallel to the direction of deformation and were stretched until failure.

Swelling characterisation

Briefly, cast hydrogels were prepared as described above. The hydrogels were weighed and then immersed in a volume of 3T3 culture media 22× the mass of the hydrogel. The immersed hydrogel was incubated statically at 37 with 5% CO_2. At the indicated time points, the hydrogel was removed from the media, gently blotted with tissue paper to remove surface water, and then weighed to obtain the swollen mass. The hydrogel was then re-immersed in the media and incubated once again. This was repeated for each time point. On the final time point, the hydrogel was either tensile tested or dried to obtain the dry mass. Drying was conducted in an oven at 40°C. Swelling ratio was calculated using the following equation:

$$Swelling\ ratio(\%) = \frac{(swollen\ mass\ -\ dry\ mass)}{dry\ mass} \times 100$$

Results

The aim of this chapter was to examine whether PEGDA could improve the mechanical properties of alginate. Hybrid hydrogels were prepared by blending PEGDA and alginate and their strength and moduli were assessed using tensile testing. The swelling of the hydrogels was also characterised, and the impact of swelling on their mechanical properties.

PEDGA synergistically improves the mechanical properties of alginate

The mechanical properties of three blends of alginate with PEGDA were examined by tensile testing. Three ratios of PEGDA to alginate were chosen, whilst maintaining the total hydrogel content at 11% (w/v). These hydrogels were cast in dumbbell-shaped PTFE moulds and subsequently tensile tested. The cast hydrogels were stretched until fracture, from which stress-strain curves were plotted (see **Appendix B**). From these curves the ultimate tensile strength (UTS), elastic modulus (EM) and failure strain (FS) were obtained.

The hybrid hydrogels displayed a composition-dependent and molecular weight-dependent change in mechanical properties (**Figure 3-2**). Compared to alginate, all compositions of hybrid hydrogels displayed increased UTS. The 10 kDa hybrids displayed a 2-fold or greater increase

in UTS when compared to alginate. Though less pronounced, there was a significant increase in UTS when comparing the 20 kDa hybrids with alginate, excluding the 9:2 composition. With regards to the EM, the 10 kDa hybrid hydrogels displayed lower or equal moduli to alginate hydrogels. Excluding the 10:1 composition, the 20 kDa hybrids demonstrated higher moduli. For the FS, the 10 kDa hybrids were more stretchable than alginate. As for the 20 kDa hybrids, the 9:2 and 8:3 compositions displayed FSs similar to alginate. The FSs for the 10:1 20 kDa hybrids were similar to the 10:1 10 kDa hybrids.

In order to look for synergistic effects, the UTSs of the 20 kDa hybrid hydrogels were compared to the sum of the UTSs of alginate hydrogels and 20 kDa PEGDA hydrogel (**Figure 3-3a**). For the 10:1, 9:2 and 8:3 compositions, the 20 kDa hybrid hydrogels showed a 2.4-fold, 1.2-fold and 1.7-fold increase in UTS than the sum of the UTSs of their individual components, respectively. The 20 kDa and 10 kDa hybrids were compared by calculating ratios of their individual mechanical properties.

The values for UTS, EM and FS for the 20 kDa hybrids were normalised by the corresponding values of the 10 kDa hybrids (**Figure 3-3b**). As a general trend, the 10 kDa hybrids had a greater UTS and FS and a lower

EM than the 20 kDa hybrids. This indicated that the 10 kDa hybrids were stronger, deformed more easily, and stretched to a greater proportion, in comparison to the 20 kDa hybrids.

These results demonstrate synergy between alginate and PEGDA in the hybrid hydrogels, and that these hybrid hydrogels display different mechanical properties depending on its composition, indicating tunability of the hydrogel. By changing the proportion of alginate and PEGDA, the mechanical properties of the resulting hybrid hydrogel can be altered. However, in this instance, the results presented here are insufficient and do not show any general trend. Further work is required in order to better predict the mechanical properties of a given composition of hybrid hydrogel. Nonetheless, these results only show the behaviour of the hybrid hydrogels immediately after crosslinking, and do not represent how the hydrogels will behave after incubation in an aqueous environment.

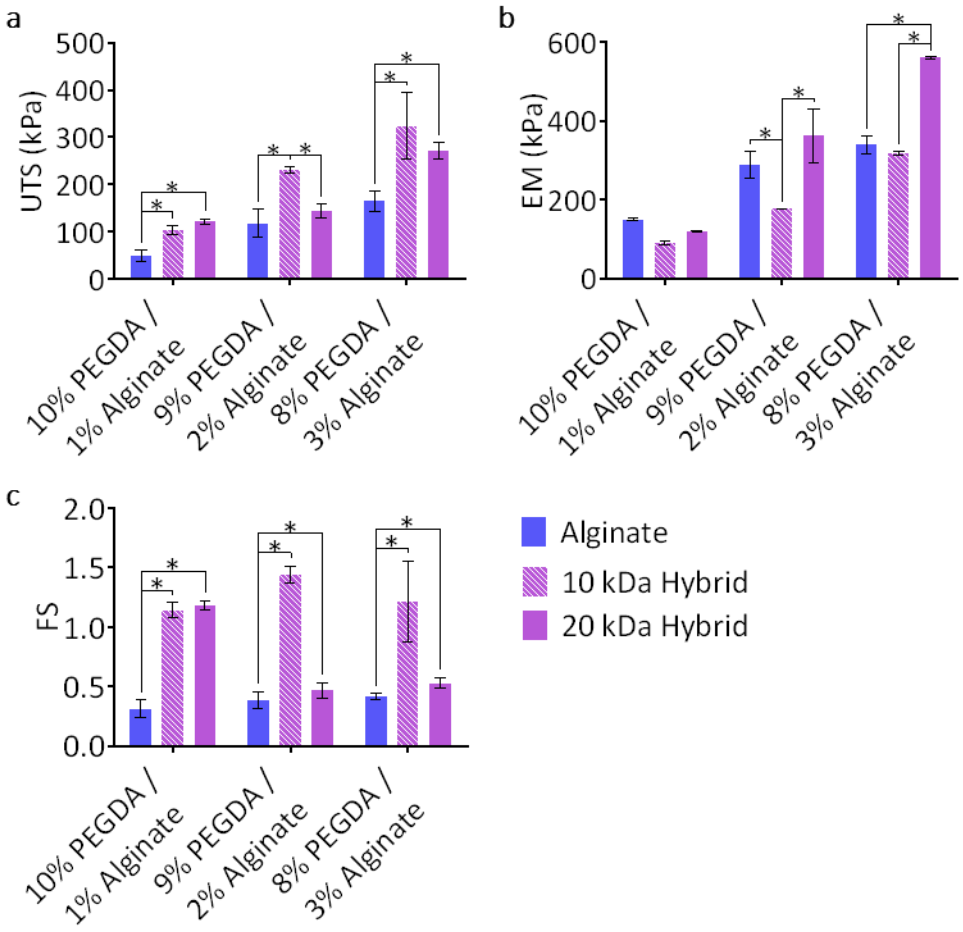

Figure 3-2 Hybrid PEGDA/alginate hydrogels display improved mechanical properties in a composition-dependent manner. Hydrogel solutions, either alginate, PEGDA, or a blend of the two, were cast in a dumbbell-shaped mould. The crosslinked hydrogels were examined by tensile testing to obtain UTS (a), EM (b) and FS (c). Mean values were plotted. Error bars represent standard deviation (n = 3). An asterisk (*) indicates statistical difference using $\alpha = 0.05$.

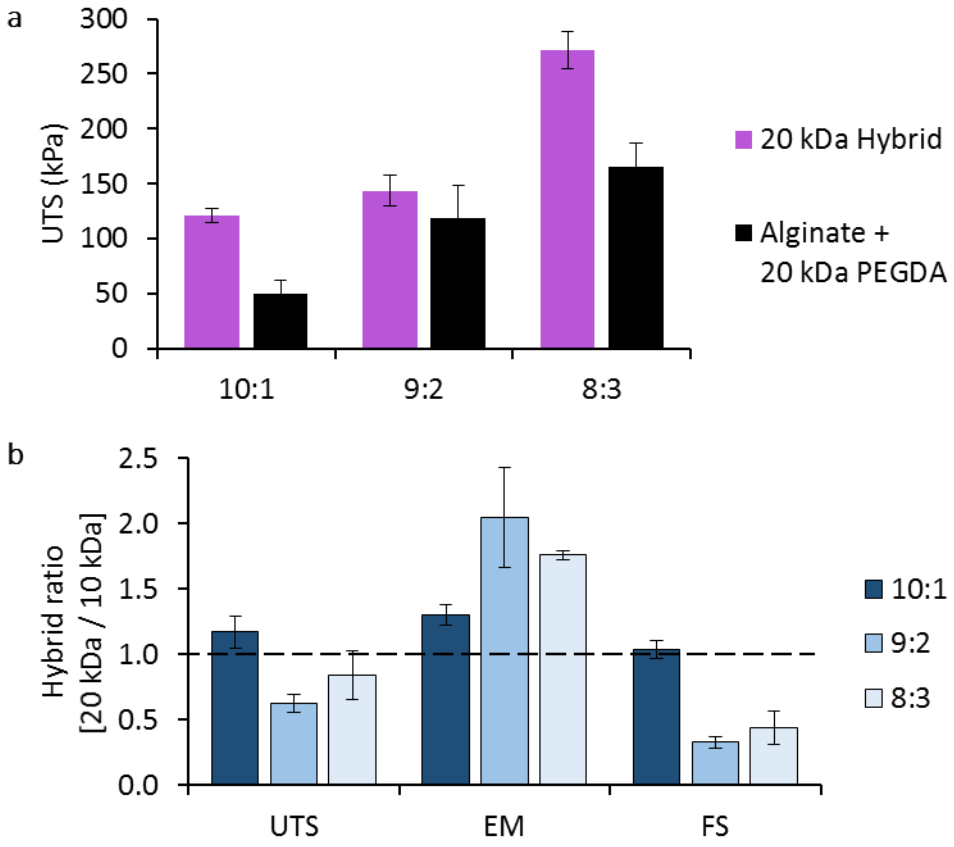

Figure 3-3 PEGDA synergistically improves the mechanical properties of alginate. (a) The UTSs of the 20 kDa hybrid hydrogels were compared to the sum of their individual components, alginate and 20 kDa PEGDA. (b) The absolute values for each concentration of the 20 kDa hybrids were divided by the corresponding absolute values of the 10 kDa hybrids and plotted as a ratio. The dashed line at a ratio of 1.0 represents equal values.

Swelling diminished hybrid mechanical properties

To assess their behaviour in an aqueous environment, the cast hybrid hydrogels were immersed in cell culture media and incubated at 37°C. The hydrogels were then weighed at various time points and then dried after 48 h. A graph of swelling ratio was plotted (**Figure 3-4a**). Both 20 kDa and 10 kDa hybrids swelled to equilibrium within 12 h of incubation and, after 48 h of incubation, were still at their fully swollen state. Increasing the ratio of PEGDA to alginate in the hybrid hydrogel increased the proportion of swelling. This effect was particularly noticeable in the 20 kDa hybrids where, after 48 h, the swelling ratios were 1851±85%, 2207±152% and 2517±181% for the 8:3, 9:2 and 10:1 compositions, respectively. Decreasing the molecular weight of PEGDA decreased the proportion of swelling of the hybrids, and this decrease was much greater: the 10 kDa hybrids swelled less than the 20 kDa hybrids.

To look at the impact of adding PEGDA to alginate, the swelling profiles of alginate (**Appendix B**) were subtracted from the corresponding swelling profiles of the hybrids in order to show the impact of PEGDA on the swelling profiles of the hybrid hydrogels. **Figure 3-4a** shows clear differences between the 10 kDa and 20 kDa hybrids. The 20 kDa hybrid swelling profiles are all positive, whilst the 10 kDa hybrids have negative

swelling profiles (**Figure 3-4b**), suggesting that the addition of 10 kDa PEGDA caused a reduction in swelling in the resultant 10 kDa hydrogels, whilst the addition of 20 kDa PEGDA caused an increased in the proportion of swelling in the resultant 20 kDa hybrid hydrogels.

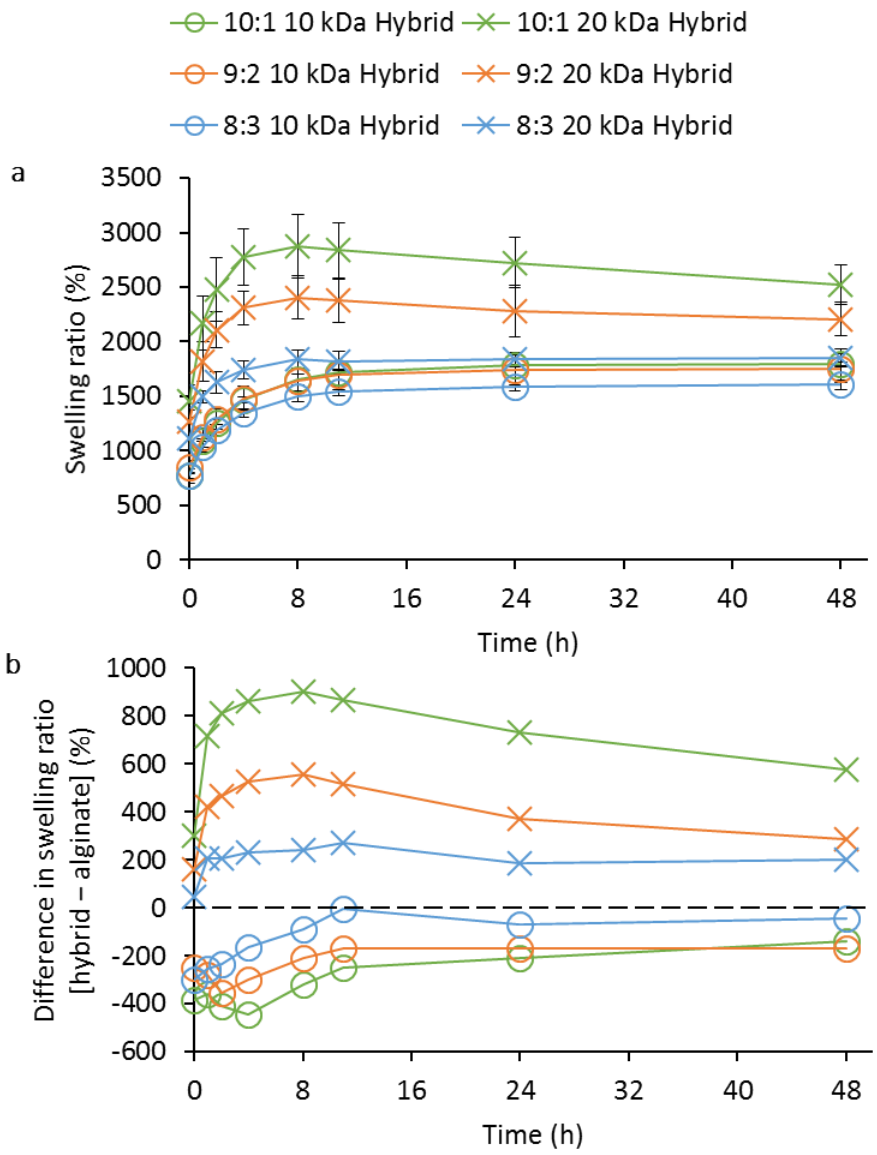

Figure 3-4 Hybrid hydrogels swell when incubated in an aqueous environment. Hybrid hydrogel solutions were cast in a dumbbell-shaped mould. The crosslinked hydrogels were incubated at 37°C in 3T3 culture media. The hydrogels were weighed at various time points, and the swelling ratio at each time point was calculated. (a) Swelling profiles of hybrid hydrogels. Mean values were plotted. Error bars represent standard deviation (n = 3). (b) The swelling profiles of alginate were subtracted from swelling profiles of the hybrid hydrogels to identify the impact of adding PEGDA to alginate. The dashed line at 0% represents no change in the swelling profiles.

Swollen hydrogels display diminished mechanical properties

To assess the impact of swelling on hydrogel mechanical properties, tensile testing was performed on hydrogels in their swollen state. The role of the hybrid hydrogel was to be used as a shell material during core–shell bioprinting and the hybrid hydrogel would therefore be incubated in an aqueous environment whilst the cells in the core were being cultured. The hybrid hydrogel would therefore need to retain its mechanical properties whilst in that aqueous environment. Therefore, the mechanical properties of the hybrid hydrogels were examined when in their fully swollen state.

After 48 h of swelling, when fully swollen, the hybrid hydrogels were examined by tensile testing to determine how their mechanical properties had changed whilst in the swollen state. Results were plotted as a percentage of the mechanical properties prior to swelling (**Figure 3-5**). Following 48 h of swelling, all 20 kDa hybrid hydrogels were weaker, particularly the 10:1 hydrogels, which were too soft to handle and therefore could not be successfully examined by tensile testing. The 9:2 20 kDa hybrid hydrogels were also weaker, retaining just 30.3±4.8% and 59.7±5.6% of their UTS and EM, respectively. Of the 20 kDa hybrid hydrogels, the 8:3 compositions retained the most of their mechanical

properties and were only slightly weaker, retaining 79.7±16.4% and 90.1±7.3% of their UTS and EM, respectively.

As a general trend, reducing the proportion of 20 kDa PEGDA in the hybrid hydrogel increased the proportion of retained UTS and EM. The behaviour of the 10 kDa hybrid hydrogels was composition dependent and did not follow the same trend as the 20 kDa hybrid hydrogels. The 10 kDa hybrid hydrogels retained more of their UTS and EM. All compositions showed a decrease in their UTS; 10:1 showed the lowest retained UTS with the lowest retained EM. However, the 9:2 composition, whilst only retaining 72.1±4.2% UTS, displayed increased EM at 119.0±11.6%. Overall, the hybrid hydrogels were mechanically weaker following swelling and, excluding the 9:2 10 kDa hybrid hydrogel, were softer in terms of stiffness.

The FS for the hybrid hydrogels displayed opposite effects depending on the MW of PEGDA (**Figure 3-5**). A fall in FS indicates a loss of stretchability. For the 10 kDa hybrids, there was a decreasing trend in the retained FS, from 87.6±7.8% for 10:1 to 61.8±6.7% for 8:3. Though no data could be recorded for the 10:1 20 kDa hybrid, the remaining 20 kDa hybrids saw the opposite. There was an increasing trend in the

retained FS from 55.7±11.8% for 9:2 to 91.0±13.3% for 8:3. However, for all hybrids, the retained FS did not exceed 100%, indicating that all hybrid became less stretchable following swelling.

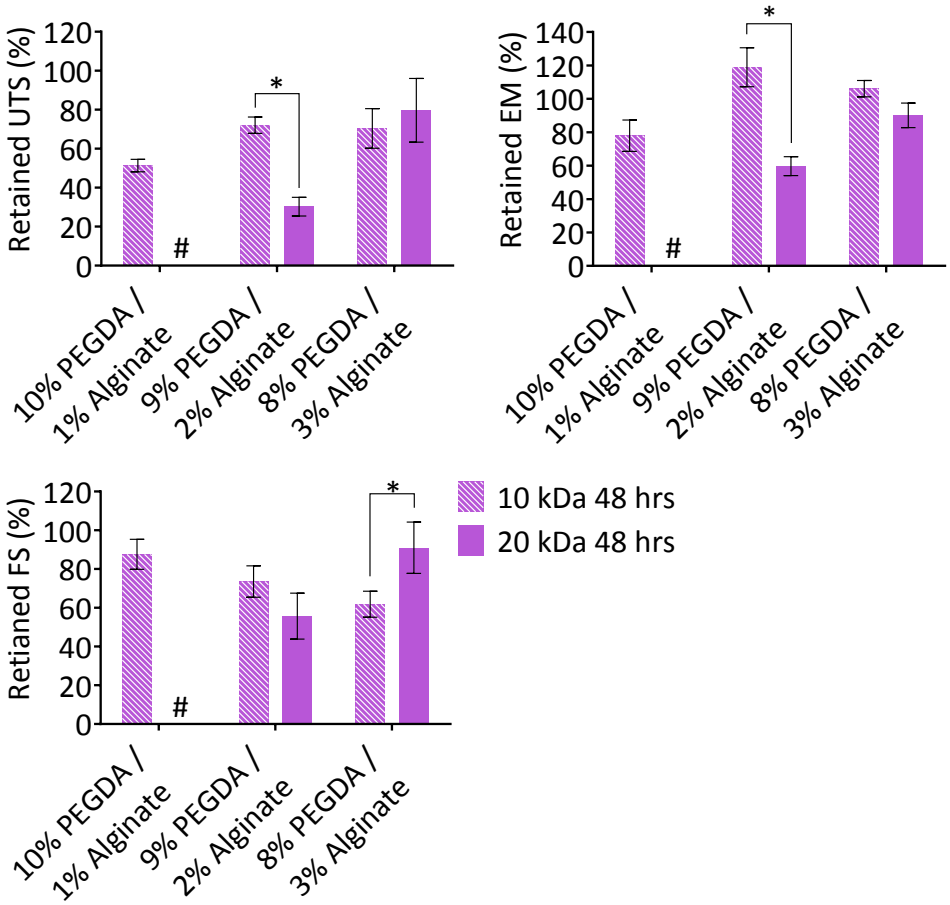

Figure 3-5 Hybrid PEGDA/alginate hydrogels display diminished mechanical properties following swelling. Hydrogel solutions, either alginate, PEGDA, or a blend of the two, were cast in a dumbbell-shaped mould. The crosslinked hydrogels were incubated at 37°C in 3T3 culture media. At the indicated time points, the crosslinked hydrogels were examined by tensile testing to obtain UTS (a), EM (b) and FS (c). Results were plotted as a percentage prior to swelling. Mean values were plotted. Error bars represent standard deviation (n = 3). An asterisk (*) indicates statistical difference using $\alpha = 0.05$. A hash (#) indicates samples that were too weak to be handled.

Discussion

This chapter has sought out to improve the mechanical properties of alginate by addition of the synthetic polymer, PEGDA. Both alginate and PEGDA are biocompatible and have been used in clinical trials (Sharma *et al.*, 2013; Basta *et al.*, 2011). Earlier studies have sought to improve the mechanical properties of alginate by adding polyacrylamide (Sun *et al.*, 2012; Hong *et al.*, 2015; Gong *et al.*, 2003). Here, we have substituted polyacrylamide with PEGDA to increase the biocompatibility of the hybrid materials. PEGDA, which is a derivative of PEG that has been modified to have acrylate groups on both ends of the monomer chain, is a synthetic biocompatible polymer. When exposed to light of the correct wavelength, corresponding to a suitable photoinitiator, PEGDA can be photo-polymerised to form a covalently-crosslinked stable hydrogel (Cavallo *et al.*, 2017; Mazzoccoli, Feke, Baskaran and Pintauro, 2010; Fairbanks, Schwartz, Bowman and Anseth, 2009).

PEGDA was mixed with alginate, and crosslinked using their individual mechanisms, photo-polymerisation and ionic crosslinking, respectively. A mechanism for their interaction has been previously suggested (Hong *et al.*, 2015; Sun *et al.*, 2012). It was suggested that as the hydrogel is deformed, the ionic bonds in alginate break, thus dissipating the

deformation energy. The hydrogel remains intact due to the covalently-crosslinked PEGDA, and is able to stretch due to straightening of the long chains in the PEGDA network. When the deforming force is removed, the hydrogel recovers its shape due to the ionic bonds in alginate re-forming.

First, the tensile properties of the bulk PEGDA/alginate hybrid hydrogels were assessed. Addition of PEGDA to alginate improved the UTS and FS of the resulting hydrogels (**Figure 3-2**). The increase in UTS was much greater than the sum of the individual components, suggesting a synergistic effect (**Figure 3-3**). This effect may be a result of how the hydrogel chains interact and the increase in UTS may be a result of chain entanglement (Jiang *et al.*, 2013; Chen *et al.*, 2016a). The impact of combining alginate with PEGDA was shown to be composition-dependent, in addition to dependent on the molecular weight of the added PEGDA; different compositions with different PEGDA molecular weights yielded hydrogels with varying mechanical properties highlighting the tunability of hybrid hydrogels.

In this study, swelling was shown to negatively impact the mechanical properties of the PEGDA/alginate hybrid hydrogel, reducing both the

ultimate tensile strength and the elastic modulus. Previous studies have shown that the swelling profile of alginate can be controlled using different crosslinking molecules (Lee *et al.*, 2000; Lee, Bouhadir and Mooney, 2004). Here, PEGDA was shown to impact the swelling of alginate. 20 kDa hybrid hydrogels swelled to a greater degree than the 10 kDa counterparts (**Figure 3-4a)**. Whilst 20 kDa caused alginate to swell to a greater degree, 10 kDa PEGDA resisted swelling and reduced the amount of swelling in alginate (**Figure 3-4b**). The chain length of 10 kDa PEGDA is shorter than the chain length of 20 kDa PEGDA. The smaller mesh size and increased stiffness of the 10 kDa PEGDA may have resulted in its resistance to swelling. Other studies have shown that increasing PEG molecular weight increases the degree of swelling in hydrogels (Weber, Lopez and Anseth, 2009a; Yang, Malkoch and Hult, 2013). In their swollen state, it was shown that the hybrid hydrogels were mechanically weaker, with the 20 kDa hybrids showing a larger drop in mechanical properties (**Figure 3-5**). The loss of mechanical properties in swollen hydrogels has been shown previously in other hydrogels (Chen *et al.*, 2016a; Itagaki *et al.*, 2010; Liu *et al.*, 2012; Gao, Du, Sun and Fu, 2015a; Wang *et al.*, 2012). The greater loss in mechanical properties of the 20 kDa hybrids may be attributed to the fact that the 20 kDa hybrids swelled to a greater proportion than the 10 kDa hybrids. The greater

infiltration of more water and subsequent greater expansion of the hydrogel network, leaving it in a weakened state. In the selection of hydrogels and subsequent tailoring of its properties, for example, to suit the function of a particular cell type, or to provide sufficient mechanical properties for a regenerative medicine therapy. It is important to consider the aqueous nature of the environments after implantation and the subsequent impact on the hydrogels mechanical properties due to swelling.

Overall, the 10 kDa 9:2 composition will be used in the following studies. In comparison to the other compositions, the 9:2 composition retained the most of its mechanical properties after swelling. This is a key factor to ensure that the hydrogel remains stable when cultured in an aqueous environment for extended periods of time.

Conclusion

To summarise, this chapter has shown:

- PEGDA/alginate hybrid hydrogels display synergy in a composition-dependent and PEGDA MW-dependent manner. The properties of the hybrid hydrogel can be tuned.
- The hybrid hydrogels swell in an aqueous environment; 20 kDa hybrids swelled more than their 10 kDa counterparts. The mechanical properties of these fully swollen hydrogels were diminished.
- The composition of 9% (w/v) 10 kDa PEGDA with 2% (w/v) alginate will be selected and used in further experiments due to its ability to retain more of its mechanical properties following swelling.

Chapter 4 – 3D bioprinting using core–shell strands

Introduction

3D printed constructs must display a number of properties in order to carry out their desired roles. For a 3D bioprinted construct, such properties include porosity for efficient nutrient and waste exchange, mechanical stability for *in vitro* manipulation and after implantation, and bioactive to promote cell attachment, differentiation and function. Combining these parameters into a single bioprinted construct has many challenges as materials that support cell growth lack mechanical properties that match native tissues, and some of them are too soft for being printed into self-supporting structures. Core–shell strands can overcome this limitation by combining the advantages of two materials, i.e. a cell-supportive material in the core, and a printable, more mechanically-robust ink in the shell. In this chapter, core–shell strands will be explored for cell encapsulation. In the previous chapter a hybrid hydrogel of PEGDA and alginate was characterised (see **Chapter 3**). Here, that material will be used in the shell and cells, mixed with soft ECM-like hydrogels, will be used in the core.

Viscosity is a key parameter in extrusion-based bioprinting. In order to improve the viscosity of a hydrogel ink, to achieve self-supporting 3D

structures that maintain their shape fidelity after printing, various techniques have been tried, such as the addition of viscosity modifiers and increasing the hydrogel concentration (Sawkins et al., 2015; Akkineni et al., 2016). However such methods rely on extra steps during the fabrication process in order to remove the viscosity modifier, and higher hydrogel concentrations may impact on transport of nutrients (Weber, Lopez and Anseth, 2009b; Lee, Tong and Yang, 2014). One study using alginate used $CaCl_2$ to partially crosslink the alginate in order to increase its viscosity (Tabriz, Hermida, Leslie and Shu, 2015). By partially crosslinking the alginate, the viscosity was sufficient to maintain its shape, whilst applying low shear stress allowed the ink to shear thin and fall in viscosity, allowing it to be extruded.

The aim of this chapter is to explore core–shell printing as a method to co-extrude two materials simultaneously in a single strand with distinct regions. Cell viability and function in the strands will be assessed along with the ability to fabricate complex 3D structures using these core–shell strands.

Experimental design

Rheology of alginate inks

Printable inks containing alginate were prepared as described in **Chapter 2**. Rheology was performed as described in **Chapter 2**.

Core–shell bioprinting

Core–shell printing was performed as described in **Chapter 2**. A schematic of the coaxial needle used in the printing is shown in **Figure 4-1**. The shell was comprised of partially crosslinked 2% (w/v) alginate, with or without 9% (w/v) 20 kDa PEGDA. The core material consisted of a cell-laden hydrogel suspension: 3T3 cells in 5% (w/v) GelMA (with I-2959), HepG2 cells in 3 mg mL^{-1} collagen, HUVECs in Matrigel (undiluted). Lattices were printed, dimensions 20×20×1.6 mm^3, with a line spacing of 1.6 mm, and were crosslinked with calcium crosslinking buffer for 2 min at RT and, if required, UV light for 2 min.

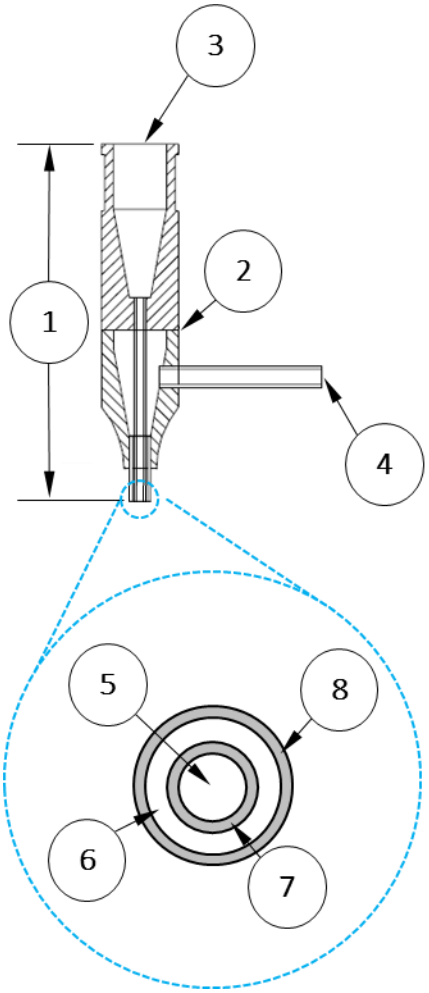

1. Length of the coaxial needle and length of the inner needle
2. Point of separation between the inner and outer needles
3. Inner needle entry point
4. Outer needle entry point
5. Inner diameter
6. Outer diameter
7. Inner needle wall
8. Outer needle diameter

Figure 4-1 Schematic of the coaxial needle used for core-shell strand extrusion.

Protein release from 3D printed core-shell strands

Hydrogels were printed using the core-shell printing technique. The shell was comprised of partially crosslinked 2% (w/v) alginate, with or without 9% (w/v) 10 kDa PEGDA. The core material was 5% (w/v) GelMA dissolved in DMEM, containing either 174 μg mL^{-1} insulin, or 10 μg mL^{-1} human IgG. Lattices were printed, with dimensions 20×20×1.6 mm^3 and a line spacing of 1.6 mm. The printed constructs were crosslinked in 100 mM

$CaCl_2$ for 2 min, washed with DMEM and then cultured in 3T3 culture media at 37°C. The point of initial incubation was considered as t = 0. At the indicated time points, 100% of the media was changed to fresh culture media. Protein samples were analysed by ELISA.

Co-culture core–shell bioprinting

Co-culture core–shell strands consisted of a HUVEC/Matrigel core with an alginate/HepG2 shell. The core was printed as described above. For the shell material, partially crosslinked alginate was prepared in HBS, opposed to diH_2O. HepG2 cells were manually stirred into the partially crosslinked alginate, at a final density of 4×10^6 cells mL^{-1}. Lattices were printed, dimensions $20\times20\times1.6$ mm^3, with a line spacing of 1.6 mm, and were crosslinked with calcium crosslinking buffer for 2 min at RT.

Bioprinting tall porous constructs

Tall porous constructs were printed for proof of concept. To print tall porous constructs, gelatine was co-printed in the line space between core–shell strands. In each layer, gelatine struts were printed first and the core–shell strands were extruded around it. The core–shell strands had a 3T3 cells in a 5% (w/v) GelMA core, with a 20 kDa hybrid shell. 3T3 cells were chosen as a model cell type and GelMA was chosen as the

biocompatible hydrogel to support them in the core of the core–shell strands. 6% (w/v) gelatine was printed at 10°C and was extruded through an 18G non-tapered nozzle using compressed air at 2 bar pressure.

Tall constructs had dimensions of 20×20×16 mm^3 and a line spacing of 1.6 mm. These constructs were crosslinked in calcium crosslinking buffer for 10 min and UV crosslinked for 10 min. The constructs were incubated in 3T3 culture medium overnight at 37°C. The constructs were cut transversely, freeze-dried, and imaged using SEM.

Compression of 3D printed hydrogels

Cell-laden hydrogels were printed using the core-shell strand technique. The shell was comprised of partially crosslinked 2% (w/v) alginate, with or without 9% (w/v) 20 kDa PEGDA. The core material comprised of 5% (w/v) GelMA in 3T3 culture media, with 3T3 cells at a density of 4×10^6 cells mL^{-1}. The printed constructs were solid cubes, with dimensions 8×8×8 mm^3. The constructs with LAP and I-2959 were crosslinked with 10 min of visible light or 10 min of UV light, respectively. The hydrogels were compressed to 50% strain.

Albumin secretion

Albumin secretion was measured indirectly by assaying the culture media for the presence of albumin using ELISA. The media was changed precisely 24 h before the media was sampled. Fresh culture media was sampled for the blank. All media samples were stored at −80°C prior to ELISA. Media samples were thawed on ice and centrifuged at 10,000 g_n for 10 min at 4°C to pellet any cells and/or debris. Albumin ELISA was performed on the supernatants according to manufacturer's guidelines.

Results

Selection of partially crosslinked alginate

In order to select a composition of partially crosslinked alginate, a screening experiment was conducted to find the minimum concentration of $CaCl_2$ required that would produce a viscous alginate paste that was able to be extruded through the coaxial needle, retain its shape fidelity, and allow further crosslinking for stabilisation. Based on previous unpublished data by Omar Hamid (data not shown), the ratio of alginate to $CaCl_2$ used was 2:1. The concentration of $CaCl_2$ was increased by 1 mM until the desired ink was achieved (**Table 4-1**). A minimum of 15 mM was required to crosslink 2% (w/v) alginate, to match the selected composition in **Chapter 3**, sufficiently enough to allow the extruded partially crosslink alginate to retain its shape. 18 mM $CaCl_2$ and above produced an alginate paste that could not be extruded through the coaxial needle. Of the three concentrations of $CaCl_2$ suitable, 17 mM was chosen as it met all three categories, and provided the most viscosity.

Table 4-1: Screening of partially crosslinked alginate. Alginate was crosslinked with $CaCl_2$, and extruded through a coaxial needle.

[Alginate] % (w/v)		[$CaCl_2$] (mM)		Extrudable through coaxial needle?	Retains shape fidelity?	Can be fully/ further crosslinked with $CaCl_2$?
Initial	Final	Initial	Final			
1.5	1	30	10	Yes	No	No
1.5	1	33	11	Yes	No	No
1.5	1	36	12	Yes	No	No
1.5	1	39	13	Yes	No	No
1.5	1	42	14	Yes	No	No
1.5	1	45	15	Yes	No	No
1.5	1	48	16	Yes	No	No
1.5	1	51	17	Yes	No	No
1.5	1	54	18	Yes	No	No
1.5	1	57	19	Yes	No	No
1.5	1	60	20	Yes	No	No
3	2	30	10	Yes	No	Yes
3	2	33	11	Yes	No	Yes
3	2	36	12	Yes	No	Yes
3	2	39	13	Yes	No	Yes
3	2	42	14	Yes	No	Yes
3	2	45	15	Yes	Yes	Yes
3	2	48	16	Yes	Yes	Yes
3	2	51	17	Yes	Yes	Yes
3	2	54	18	No	Yes	Yes
3	2	57	19	No	Yes	Yes
3	2	60	20	No	Yes	Yes
3	2	30	10	Yes	No	Yes
3	2	33	11	Yes	No	Yes
3	2	36	12	Yes	No	Yes
3	2	39	13	Yes	No	Yes
3	2	42	14	Yes	No	Yes
3	2	45	15	Yes	Yes	Yes
3	2	48	16	Yes	Yes	Yes
3	2	51	17	Yes	Yes	Yes
3	2	54	18	No	Yes	Yes
3	2	57	19	No	Yes	Yes
3	2	60	20	No	Yes	Yes

Preparation of viscous inks for bioprinting

In order to extrude core–shell strands, the viscosity of the shell material had to be increased so that two strands could be extruded within close proximity and not coalesce in order for the printed construct to maintain its shape. Alginate was partially crosslinked using $CaCl_2$ via syringe mixing to produce a viscous ink. Rotational rheology was performed to determine the viscosities of these inks. **Figure 4-2** shows the viscosities of the alginate and PEGDA/alginate compositions. Addition of PEGDA to alginate caused a 2.5-fold increase in the viscosities of the resulting hybrid solutions at a shear rate of 0.1 s^{-1}. Partially crosslinking alginate resulted in a 1000-fold and 200-fold increase in the viscosity of 2% and 3% alginate, respectively. The partially crosslinked hybrid solutions displayed viscosities similar to the partially crosslinked alginate. The partially crosslinked alginate and hybrids both retained their shear thinning properties. The partial crosslinking caused the resulting inks to exhibit shear thinning properties from lower shear rates than their uncrosslinked counterparts, i.e. partially crosslinked began shear thinning from a shear rate of 0.1 s^{-1}, whereas the uncrosslinked solutions begin to reduce viscosity at a shear rate of 10 s^{-1}.

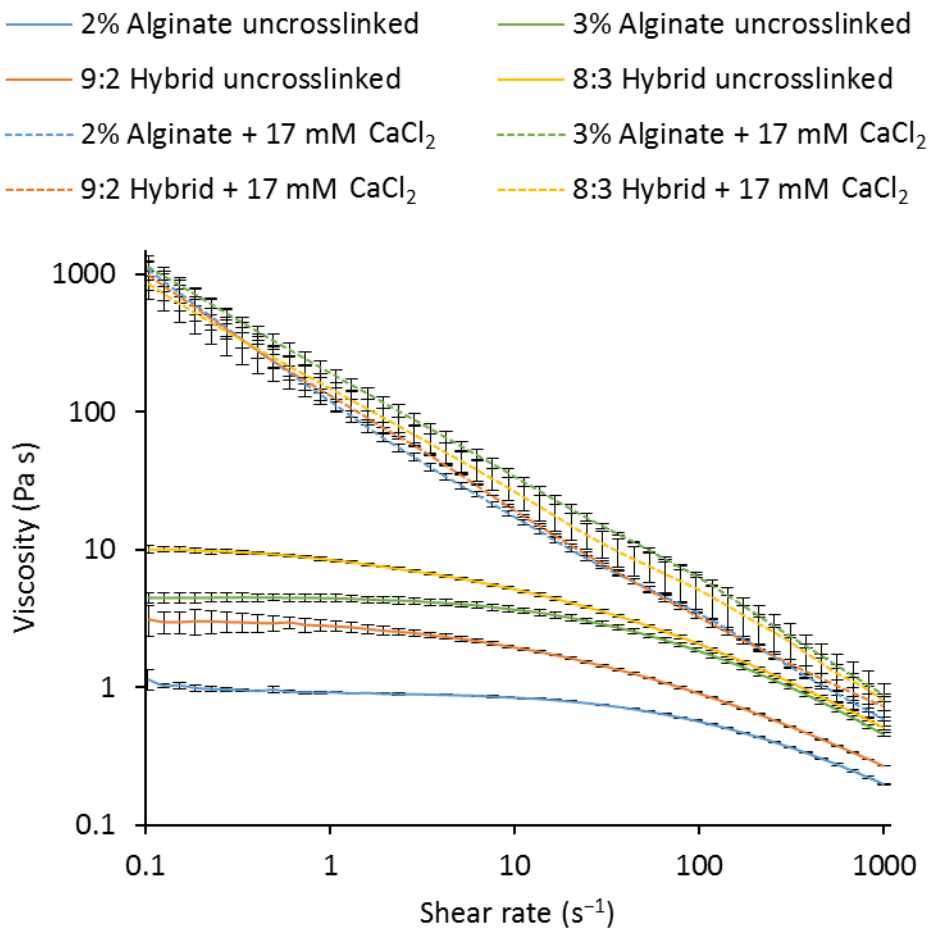

Figure 4-2 Rheology of printable alginate inks. Alginate was crosslinked with 17 mM $CaCl_2$ via syringe mixing. To determine its viscosity, the partially crosslinked inks were examined by rotational rheology. A shear rate sweep from 0.1 to 1000 s^{-1} at RT using a cone-plate setup was performed. The viscosities of the uncrosslinked solutions were examined, in addition to the rheology of the PEGDA/alginate hybrids. Mean values were plotted. Error bars represent standard deviation (n = 3).

Optimisation of extruded core–shell strands

The partially crosslinked alginate and hybrid inks were examined for their printability in order to produce strands of different diameters. The inks were extruded through a custom-made coaxial needle, and strands of differing diameters were produced by varying both the shell flow rate and printhead movement speed. The smallest strands that could be fabricated were 756±58 μm in diameter, using a flow rate of 0.1 mL min^{-1} and a printhead movement speed of 3 mm s^{-1}. Reducing the flow rate below 0.1 mL min^{-1} resulted in discontinuous strands.

To select the length of the needle, 3T3 cells were extruded through two needles of different lengths at a flow rate of 0.1 mL min^{-1}, the maximum flow rate the cells would experience, and therefore the maximum shear force the cells would experience, matching the flow rate selected for the shell material. **Figure 4-3** shows that the cell viability was 95.0±0.9% for cells extruded though a 21 mm needle (measured from the initial point of narrowing to the tip of the needle). When extruded through a longer needle (33 mm), the viability was only 35.9±5.9%. The shorter needle was selected and used for further experiments.

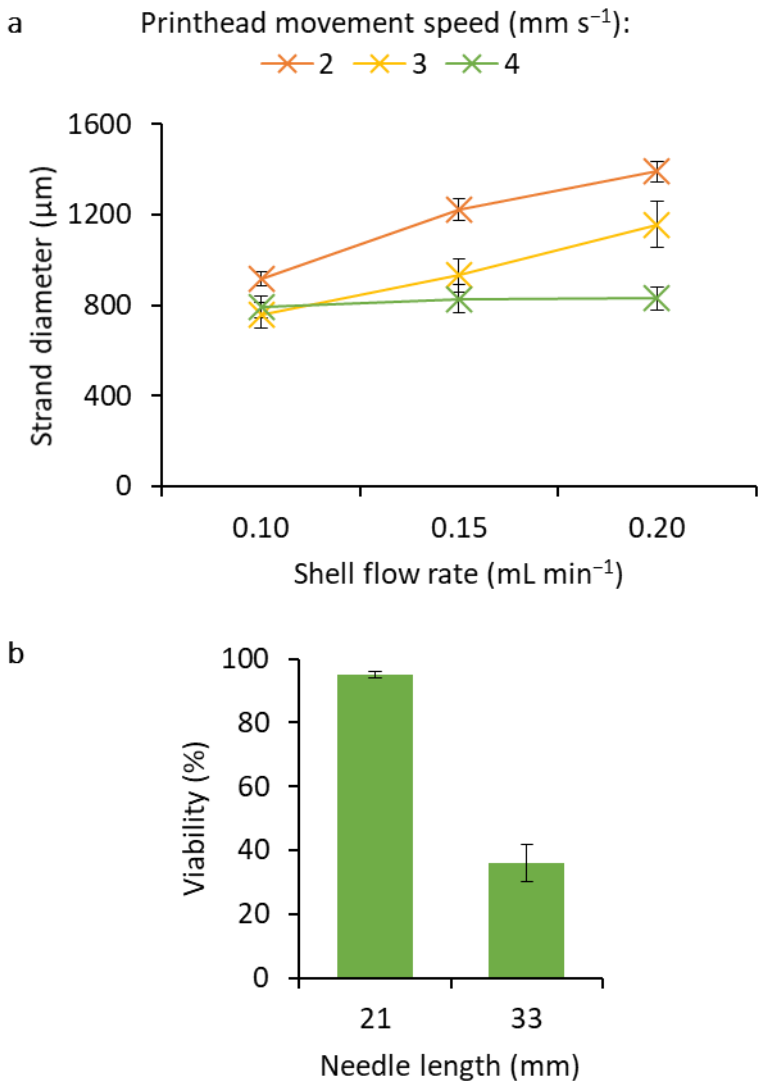

Figure 4-3 Optimisation of core–shell strand fibre diameter and needle length. (a) 2% partially crosslinked alginate ink was extruded through the custom coaxial needle at varying flow rates and printhead speeds. The core flow rate was fixed at 0.01 mL min^{-1}. Light microscopy images of the strands were taken. ImageJ was used to measure strand diameters. Mean values were plotted. Error bars represent standard deviation (n = 3). (b) 3T3 cells were extruded through 27G (210 µm) needles of varying lengths at 0.1 mL min^{-1} to measure their survival. Viability was assessed using LIVE/DEAD staining. Mean values were plotted. Error bars represent standard deviation (n = 3).

Demonstration of bioprinting using core–shell strands

The next step was to assess whether the core–shell strands could be printed into complex 3D shapes. **Figure 4-4a** shows a printed lattice structure with a core of 3T3 cells in GelMA. The printed strand shows the central position of the core within the fibre. The diameter of the core was approximately 200 µm, roughly the inner diameter of the core needle (27G/210 µm). A solid cube was also printed (**Figure 4-4b**). The cube was 1 cm^3 in volume and consisted of 14 alternating 0° and 90° layers. The layer height was determined via optical microscopy and was found to be 700 µm. Due to the large strand diameter, banding was present on the surface of the scaffold, particularly noticeable between layers, giving the side of the cube an uneven surface. A more complex ear-shape was also printed and is shown before (**Figure 4-4c**) and after crosslinking (**Figure 4-4d**). After crosslinking, the surface of the printed construct became smoother.

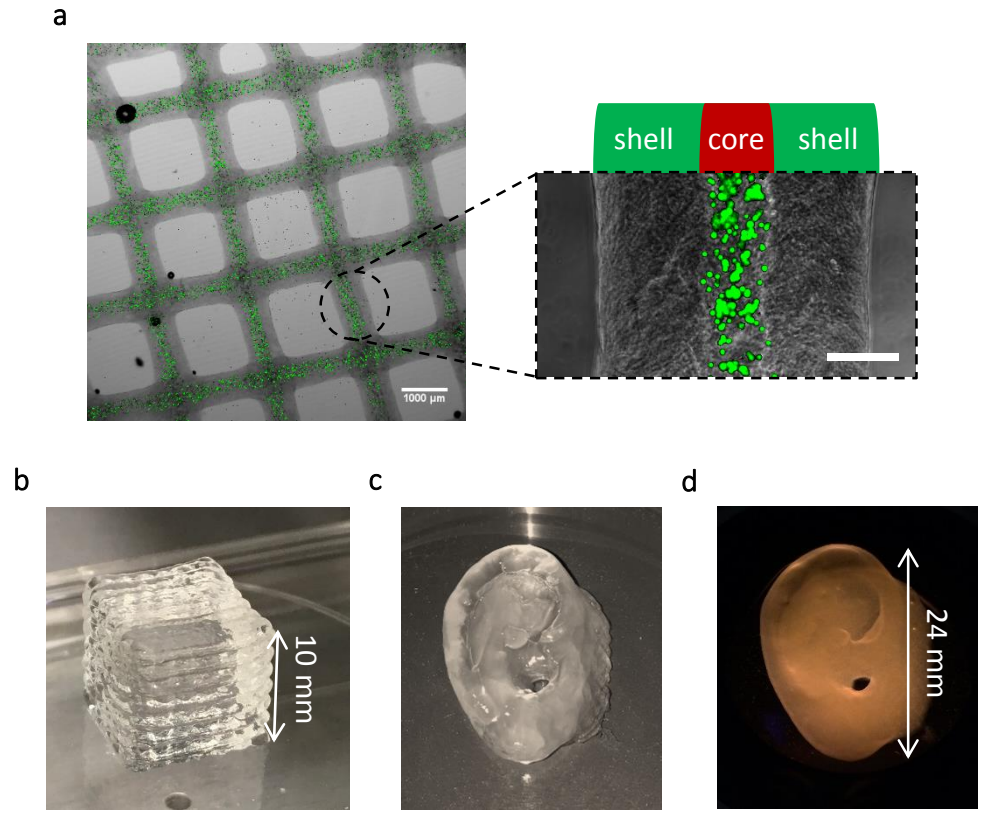

Figure 4-4 Core–shell strands, laden with 3T3 cells, were 3D printed into various constructs. (a) A printed lattice with two layers after crosslinking. A single fibre is also shown, enlarged, to show the position of the core within the alginate shell. Images were taken using confocal microscopy (left) and fluorescence microscopy (right). Scale bars represent 1 mm (left) and 200 µm (right). (b) A printed 1 cm^3 solid cube prior to crosslinking. (c) A printed ear-shaped construct prior to crosslinking. (d) The ear-shaped construct after crosslinking.

Protein diffusion through the shell material

The purpose of the hybrid hydrogel was to act as a shell material during the core-shell printing process, encapsulating a cell-laden core. The shell material, and therefore the hybrid hydrogel, will act as a barrier for nutrient diffusion between the surrounding media and the core. Protein diffusion into the core is important for the survival of cells, and protein diffusion out of the core may be necessary for the cells to carry out their function. For example, for pancreatic beta cells to function, they release insulin into the blood stream. Alternatively, if the core–shell construct was implanted *in vivo*, the shell material may act as a barrier that protects the construct from the host's immune system by preventing the diffusion of larger proteins such as antibodies. Therefore, the ability of proteins to diffuse passively through the hybrid hydrogel was assessed. Printed core–shell constructs were prepared with a GelMA core, loaded with either insulin or antibody IgG, whose molecular weights differ greatly, approximately 5.8 kDa and 150 kDa, respectively. The diffusion of these proteins through the hybrid shell was measured by quantifying the amount of each protein in the surrounding media using ELISA. The release profiles are shown in **Figure 4-5.**

ELISA standard curves can be found in **Appendix B**. For both proteins there were no significant differences between the hybrid and pure

alginate, and both materials followed the same pattern of release. This suggests that the mobility of proteins was not affected by the hydrogel chains of PEGDA. Both proteins displayed a burst release, as characterised by the rapid release followed by a plateau, and both proteins plateaued after 12 h, at which ~60% of IgG and ~75% of insulin had been released. After 48 h, ~65% of IgG and ~85% of insulin had been released in total. The plateaus of protein release suggests that, in both release studies, a portion of each protein remained entrapped within the core–shell strand. More IgG had been entrapped than insulin, indicating that the size of the protein influenced its ability to diffuse passively through the shell material. These results suggest that nutrient diffusion may be sufficient for cell encapsulation within the core of the strand. However, it also suggests that this composition of shell material is not suitable for immune-protective roles.

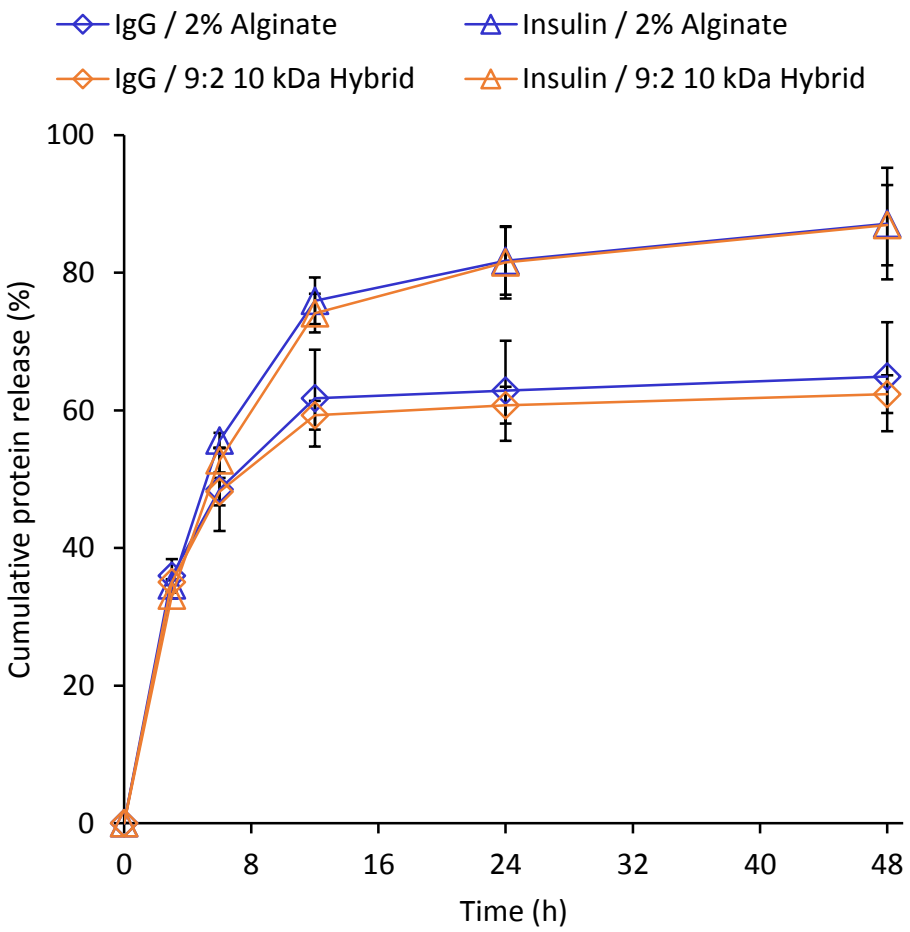

Figure 4-5 Release curves from protein-loaded core-shell strands. Core-shell strands were printed with a protein-loaded GelMA core. The protein of choice was either insulin or IgG, and the shell was composed of alginate or the alginate/PEGDA hybrid. The printed constructs were incubated at 37°C in 3T3 culture media. The amount of protein present in the surrounding media was quantified using ELISA at the indicated time points. Mean values were plotted. Error bars represent standard deviation (n = 3).

Printing tall porous structures

The fabrication of taller constructs requires pores to ensure nutrient and oxygen delivery to cells in the centre of the construct in order to avoid cell death. However to fabricate tall porous structures, co-printed gelatine was required between the core–shell strands as a sacrificial support during the printing process. A porous cube composed of core–shell strands, with a core of 3T3 cells in GelMA and with the co-printed gelatine occupying the pore space, was printed (**Figure 4-6a**). After crosslinking hydrogels in the construct, the sacrificial gelatine was removed by incubating the printed construct in an aqueous environment at 37°C (**Figure 4-6b**). To visualise the pores, the scaffold was cut transversely, freeze-dried and imaged using SEM (**Figure 4-6c**).

The fabrication of tall structures using the hybrid shell material resulted in lower cell viability during the crosslinking process. Each layer of the tall construct required UV light exposure in order to crosslink PEGDA in the shell. To evaluate the impact on cell viability during this process, printed 1 cm^3 cubes were sectioned, and the cell viability between each sectioned layer was assessed (**Figure 4-7a**). The cell viability in the topmost layer, which was exposed to the least UV light, was the greatest, at 94.8±1.2%. Moving downwards through the scaffold, as the cumulative UV light exposure increased, the cell viability decreased,

reaching a minimum of 43.2±12.2% in the layers closest to the base of the printed construct. In order to overcome this loss of cell viability, another photoinitiator, LAP, was selected. Polymerisation using LAP requires blue light in the visible region of the spectrum, opposed to the higher energy UV light required by I-2959. When exposed to visible light, for up to 40 min, the cell viability remained above 98% after exposure and above 97% on day 1 (**Figure 4-7b**). After 60 min of visible light exposure, the viability after crosslinking was 99.5±0.1%, but fell to 81.5±3.0% on day 1.

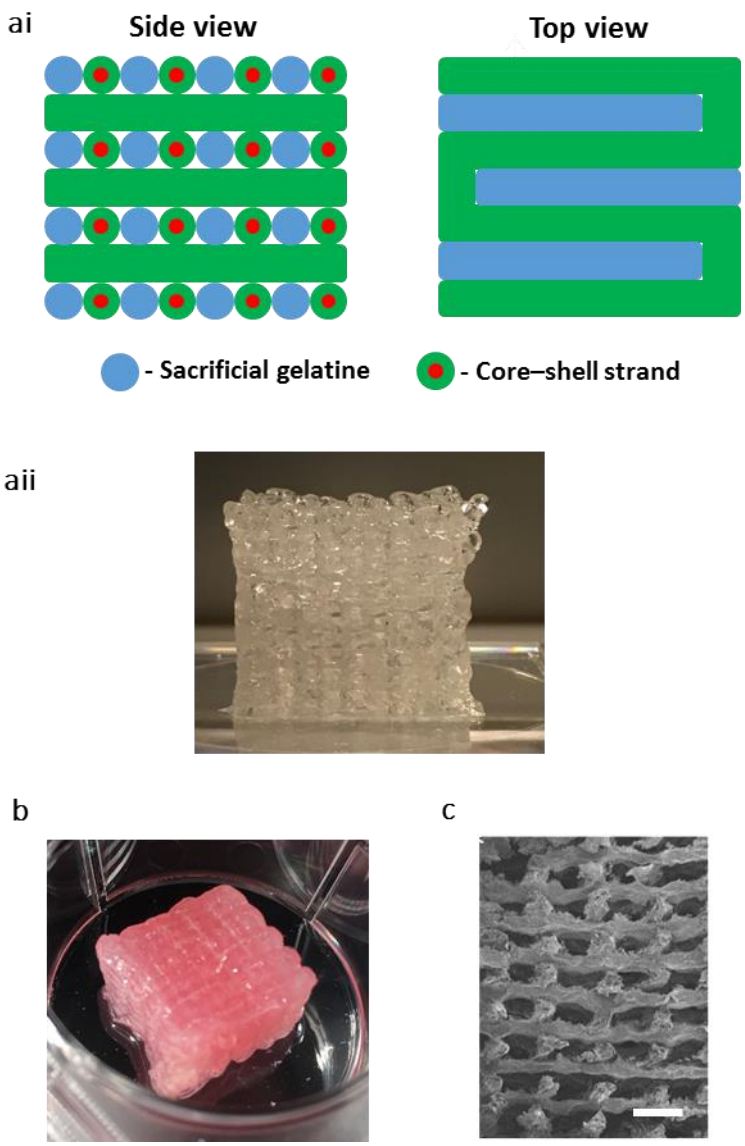

Figure 4-6 Printing of tall, porous structures using core–shell strands. Core–shell strands were pattered into a porous cube using a dual nozzle system: one nozzle dispensed core–shell strands and the other dispensed gelatine strands. The sacrificial gelatine prevented thee strands from collapsing into the pores and could later be removed. (ai) A schematic of the tall porous cube. (aii) A tall porous cube immediately after printing, where the pores were still filled with the sacrificial gelatine. (b) The porous cube after crosslinking and incubation at 37°C to remove the sacrificial gelatine. (c) SEM of a transverse section of the porous cube to visualise the pores. Scale bar represents 1 mm.

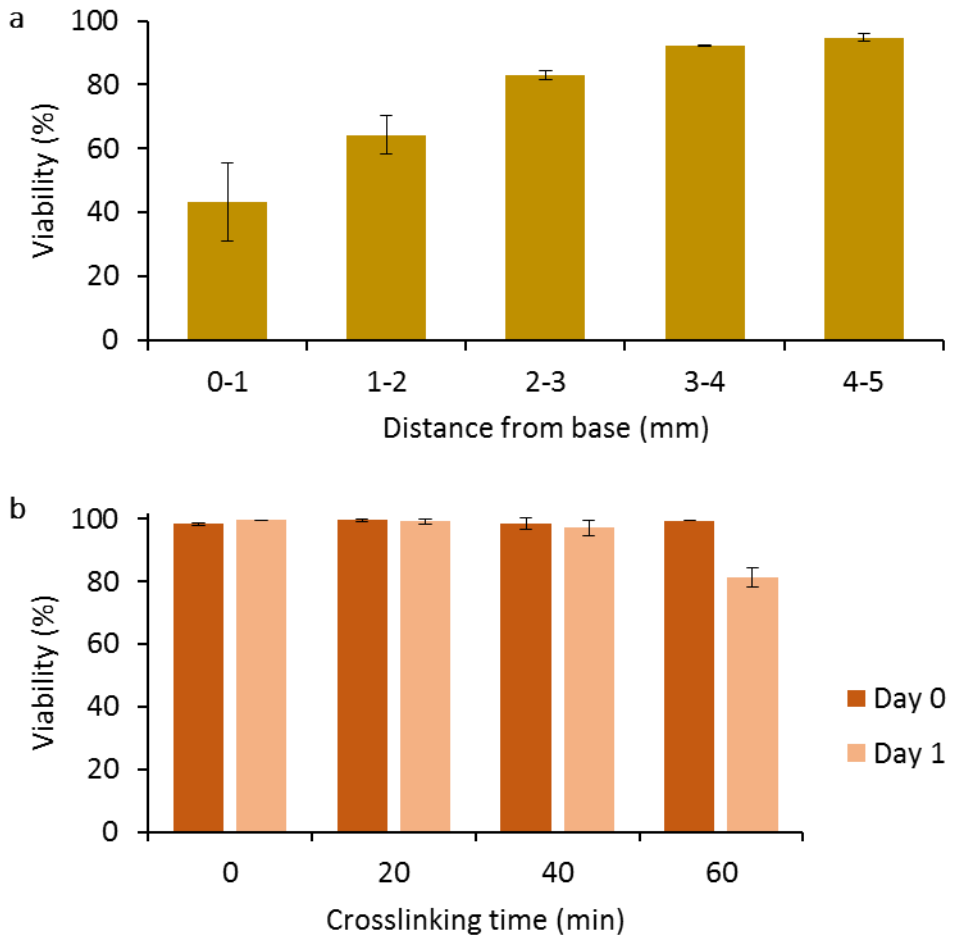

Figure 4-7 Cell viability during the crosslinking process in tall constructs. (a) Viability of 3T3 cells at different levels of a tall scaffold following repeated exposure to UV light during the crosslinking process of the hybrid hydrogel at each layer using the photoinitiator I-2959. (b) Viability of 3T3 cells following exposure to visible light for varying times using the photoinitiator LAP.

Viability of cells in the core of the core–shell strands

To assess the biocompatibility of the core–shell strand printing technique, cells were cultured in the core of the core–shell strands and their viability was monitored throughout culture. Cells were extruded with either alginate or the hybrid as the shell material. Only images of the cells in the core are shown. Images showing both the cells in the core and the shell can be found in Appendix C.

The first cells to be printed in the core were 3T3 cells in a GelMA core. 3T3 cells are from a non-cancerous origin and can be used as a base line for mammalian cell survival during the core–shell strand printing process. 3T3 fibroblasts are low cost and easy to culture, and have been cultured as feeder layers for keratinocytes and other epithelial cells. The survival of 3T3 cells promotes survival of other cell types. These cells were cultured for up to 7 days. Regardless of the shell material used, the viability remained above 90% throughout culture (**Figure 4-8a**). Morphology-wise, the cells remained rounded during culture and, by day 7, cells were present through the whole core (**Figure 4-8b**).

Tissue engineered models may be used for drug testing and toxicology studies. In this case, the liver, the site of major drug metabolism, is the organ of choice to perform these studies in. Hepatocytes are the major

cell type in the liver for drug metabolism and also are the site of any toxic side effects. A major challenge in the fabrication of engineered liver tissue is the ability for it to maintain its function long-term. In this work, HepG2 cells, a hepatocarcinoma cell line, was the next cell type to be printed in the core. HepG2 cells were the next cell-type to be printed in the core. These cells were cultured in either a collagen core or a Matrigel core. The HepG2 cells in a collagen core displayed different viabilities depending on the shell material used (**Figure 4-8a**). With an alginate shell, the viability remained above 80% up to day 28. However, with the hybrid shell, the viability was 70% after printing, and fell to 60% on day 1. By day 7 the viability recovered and was above 80%, however. The HepG2 cells proliferated and filled the core by day 7 and, as time progressed, the cells eventually began to proliferate into the shell, as demonstrated by the core widening between day 14 and day 28 (**Figure 4-8c**). Changing the core material from collagen I to Matrigel improved the viability of cells following printing (85%) and on day 1 (90%) (**Figure 4-8a**). Furthermore, the cells remained in the core throughout culture and did not proliferate into the shell (**Figure 4-8c**).

HUVECs were also printed in a Matrigel core, and displayed viability above 90% throughout culture, regardless of the shell material used

(**Figure 4-8a**). HUVECs in the core showed attachment to the Matrigel by day 1 and day 7 in the alginate and hybrid shells, respectively, as demonstrated by their elongated and spread morphology (**Figure 4-8d**). By day 7, the HUVECs had begun to align and form larger structures in both shell materials, though more pronounced for HUVECs in the alginate shell. The HUVECs adopted a cobblestone phenotype and these structures became more defined in later time points, becoming more tubular in appearance and remaining stable through to day 28.

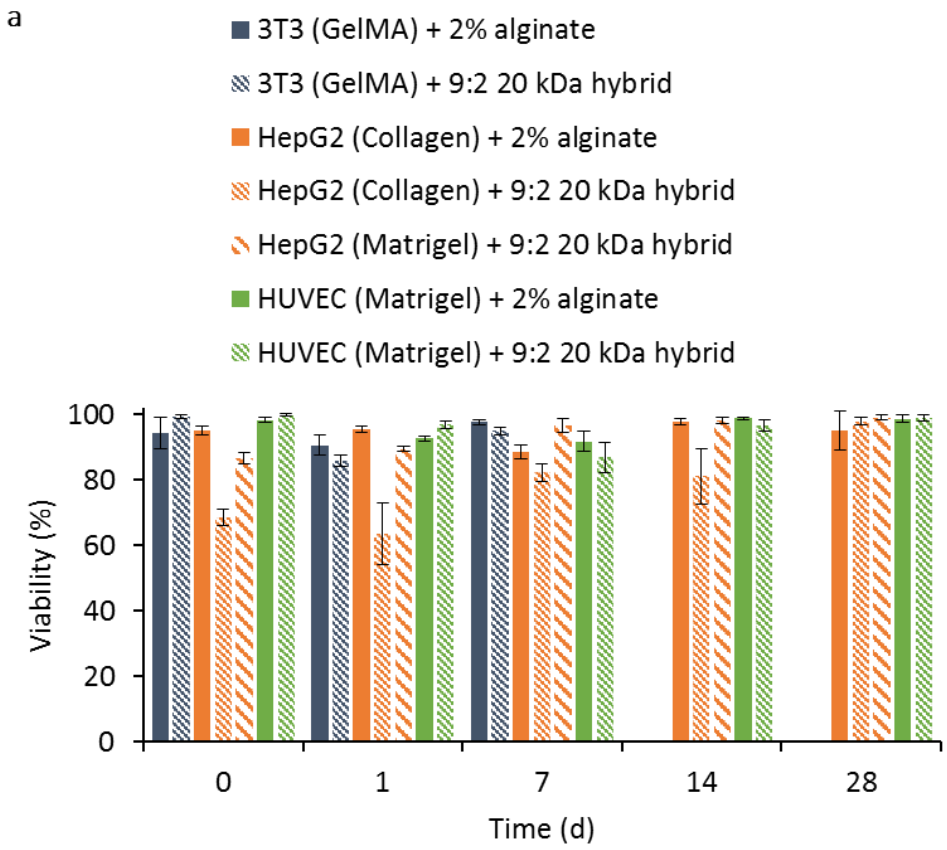

Figure 4-8 Viability and cell morphology in the core of core–shell strands. Cell-laden core–shell strands, whereby the cells were in the core and the shell was either alginate or the hybrid hydrogel, were printed, crosslinked and cultured for the indicated number of days. Cells were stained with LIVEDEAD at the indicated time-point to observe their morphology. (a) Live and dead cells were counted and viability was calculated. (b) Morphology of 3T3 cells in the core. (c) Morphology of HepG2 cells in the core. (d) Morphology of HUVECs in the core.

Figure 4-8b Morphology of 3T3 cells in the core. Scale bar represents 200 µm.

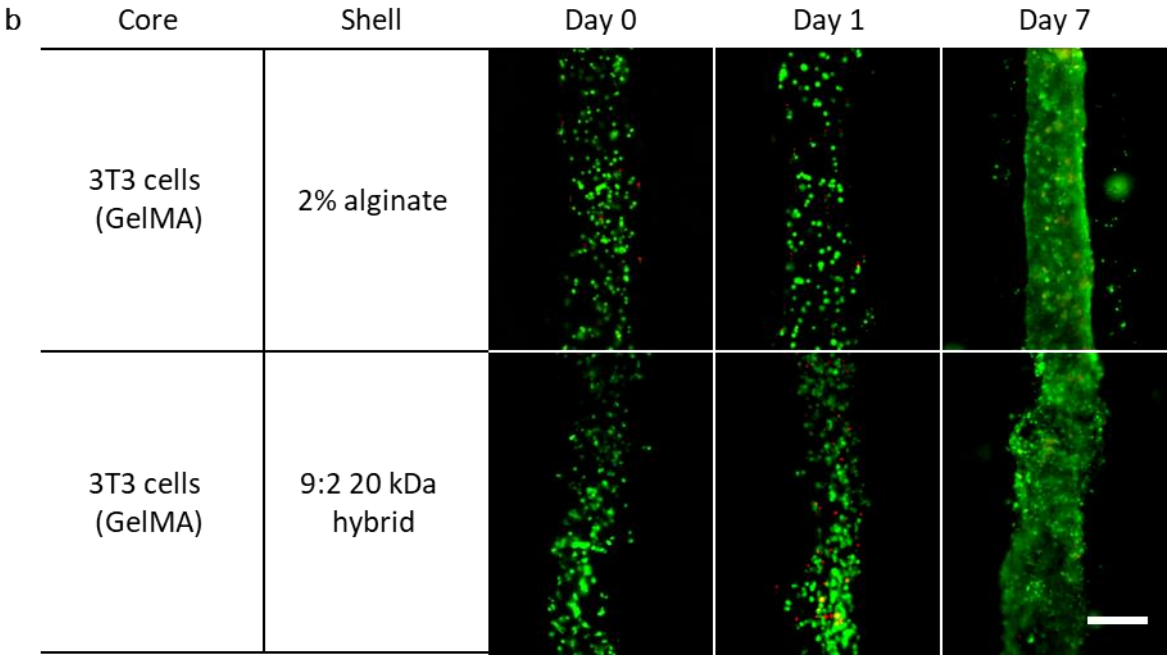

Figure 4-8c Morphology of HepG2 cells in the core. Scale bar represents 200 µm.

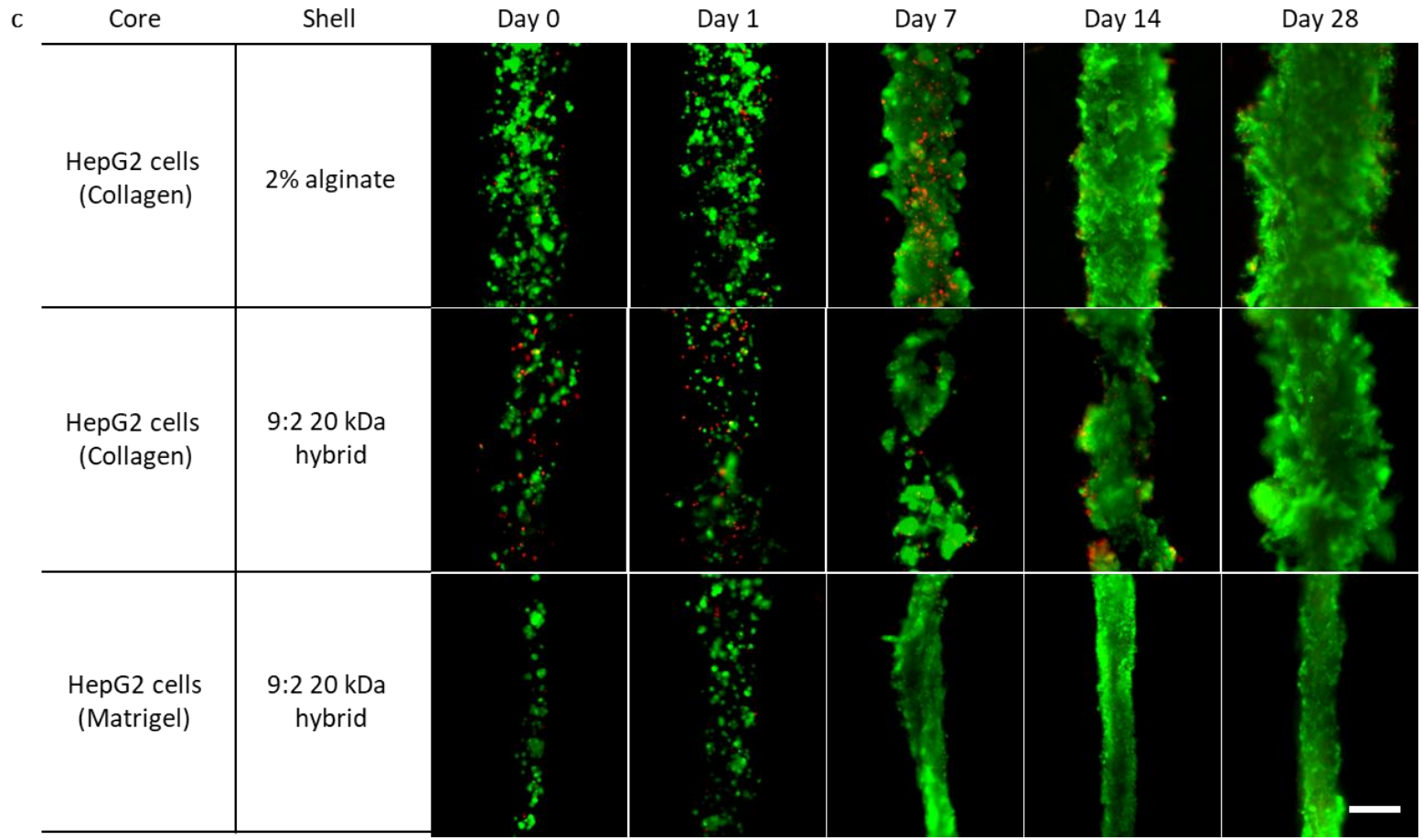

Figure 4-8d Morphology of HUVECs in the core. Scale bar represents 200 μm.

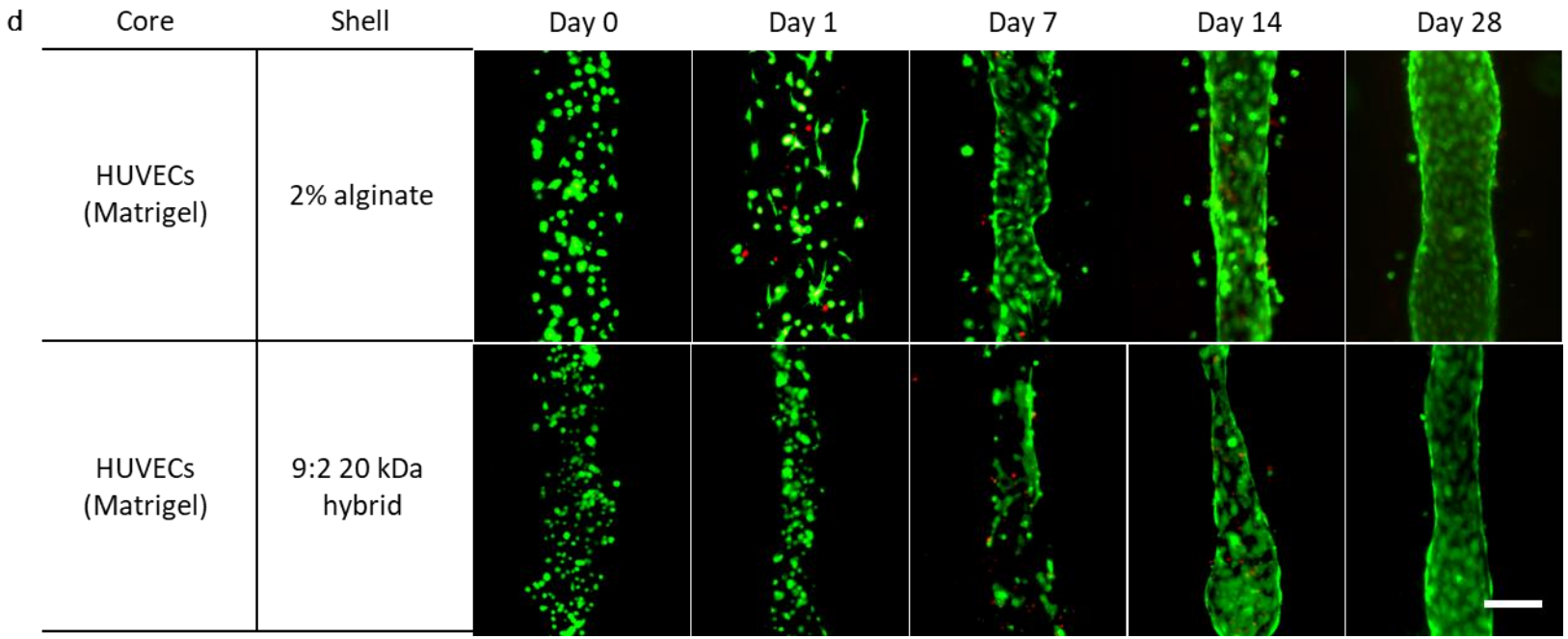

Cell function in the core of core–shell strands

To confirm if the structure displayed by HUVECs in the core of the core–shell strands was tubular, a transverse section was taken to see the cell distribution in an individual strand (**Figure 4-9a**). A continuous ring of cells was visible with a core absent of cells. The ring was a flattened circle, ovular in appearance.

A function of HepG2 cells, albumin secretion, was also checked to determine if the cells in the core were functional. Albumin secreted into the media by HepG2 cells in the collagen core of the core–shell strands was quantified by ELISA (**Figure 4-9b**). The concentration of albumin in the media increased from less than 1 μg mL^{-1} on day 1 to 152.1±5.3 μg mL^{-1} by day 28.

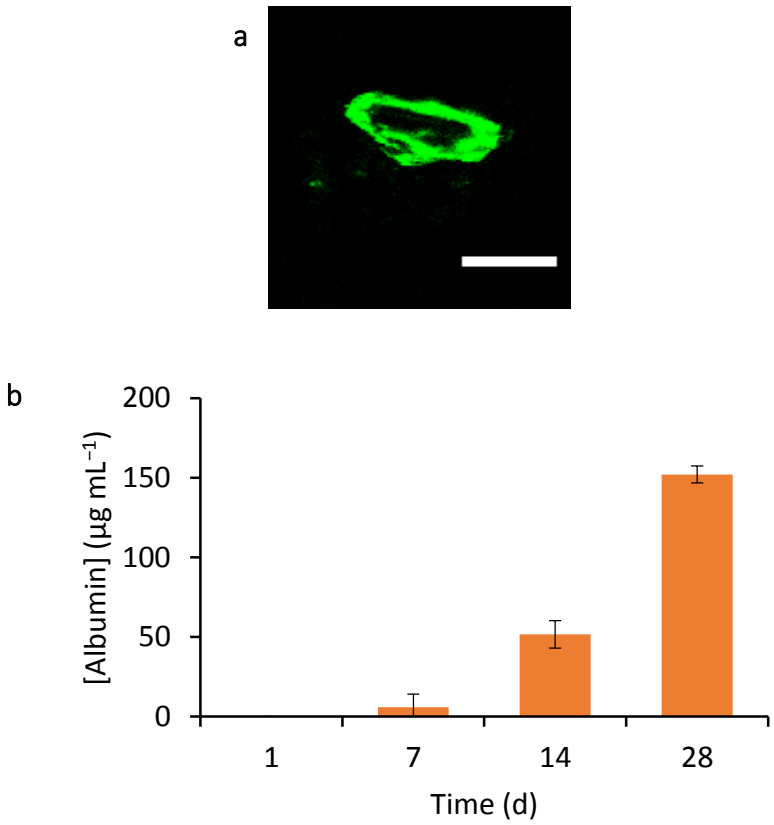

Figure 4-9 Cell function within core–shell strands. (a) Core–shell strands with a HUVEC/Matrigel core were printed and cultured. The strands were transversely sectioned at day 44 and imaged using macro confocal microscopy. Scale bar represents 200 µm. (b) Media samples from HepG2 cell-laden core–shell strands were analysed to quantify the amount of secreted albumin. Mean values were plotted. Error bars represent standard deviation (n = 3).

Patterning of two cell types in the core and shell respectively

After assessing the ability to print core–shell strands with a cell-laden core, core–shell strands containing multiple cell types were also printed. The printed strands consisted of HUVECs in a Matrigel core and HepG2 cells in the alginate shell. As shown in **Figure 4-10a**, the printed strand contained HUVECs (labelled with red-fluorescent cell-tracker) in the core of the strand and HepG2 cells (labelled with green-fluorescent cell tracker) in the shell of the strand. The printed constructs were cultured for 7 days, after which they were observed with light microscopy (**Figure 4-10b**). The core of fibre can be seen within the strand. The HepG2 cells proliferated in the shell and also on the surface of the strands.

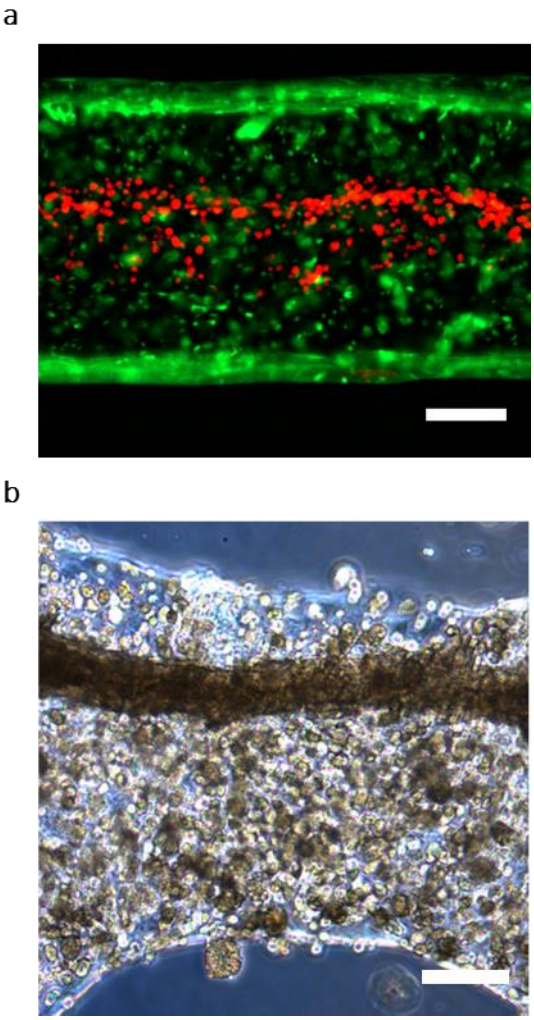

Figure 4-10 Co-printing of multiple cell-types in a single printed core–shell strand. Core–shell strands with a core of HUVECs (red) in Matrigel and HepG2 cells (green) in an alginate shell were printed. (a) The core–shell strand immediately after printing, taken with fluorescence microscopy. The HUVECs were labelled with red-fluorescent cell-tracker and HepG2 cells were labelled with green-fluorescent cell-tracker. (b) A bright-field image of the printed strand after 7 days of culture. Scale bars represent 200 μm.

3D printed hybrid cubes demonstrate improved recovery following compression

To examine the performance of the hybrid hydrogels, cell-laden core–shell strands were 3D printed into solid cubes. The core was comprised of 3T3 cells in 5% (w/v) GelMA and the shell material was either alginate or the hybrid hydrogel. Due to improved cell compatibility, LAP was also tested as a photoinitiator for the hybrid hydrogel. The printed cubes were compressed to 50% strain, beyond the failure strain of pure alginate hydrogels, and then released (**Figure 4-11a**). The percentage of height recovery was plotted (**Figure 4-11b**). Constructs containing the hybrid shell material, using either photoinitiator, demonstrated >88% recovery following compression, in comparison to constructs with the alginate shell material which only recovered 63.8±1.8% of its initial height.

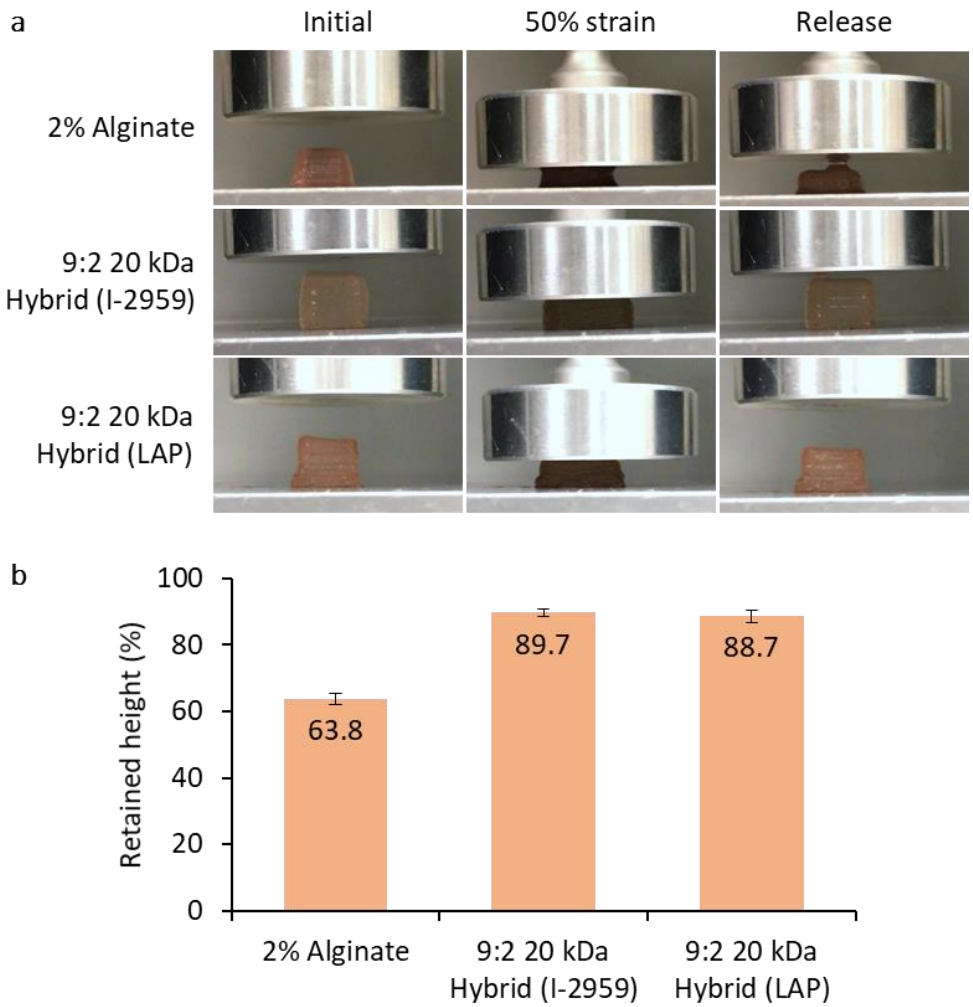

Figure 4-11 Printed constructs containing the PEGDA/alginate hybrid hydrogel demonstrated improved recovery following compression. Cell-laden core–shell strands were printed into 0.51 cm^3 solid cubes. The core consisted of 3T3 cells in 5% (w/v) GelMA and the shell material was composed of alginate or the PEGDA/alginate hybrid. The hybrid shell was crosslinked either by UV light (with the photoinitiator I-2959) or by visible light (with the photoinitiator LAP). The cubes were compressed to 50% strain and then released. (a) Representative images showing the compression of the printed constructs. (b) The change in height was measured before and after compression and was plotted as the percentage of retained height. Mean values were plotted. Error bars represent standard deviation (n = 3).

Discussion

This chapter has sought to optimise the printing of core–shell strands. Partially crosslinking alginate with 17 mM $CaCl_2$ was sufficient to raise the viscosity to produce an ink that could be extruded as a smooth strand and form stable solid 3D structures. High concentrations of alginate were not required (Luo, Lode and Gelinsky, 2013), nor was co-perfusion of $CaCl_2$ during the printing process (Colosi *et al.*, 2016b; Gao *et al.*, 2015b; Barbetta *et al.*, 2014). The printed constructs in this study were stable after printing and could be fully crosslinked in a second step after printing. This was possible for an ink with a final alginate concentration of 2% and 3%. For inks with a final alginate concentration of 1%, the inks did not form smooth strands when extruded and were not able to maintain their shape.

In this work, core–shell strand generation was achieved by using a coaxial needle. These strands could be patterned into 3D structures by combining the coaxial needle with a commercial 3D printer to control X, Y and Z motion. Unlike previous works, however the fibre diameter of the strands in this work were much larger (~800 µm). Manipulation of the flow rates and printhead movement speed could not produce continuous strands smaller than 756±58 µm. This lower limit was likely

due to the diameter of the outer needle (18G / 840 μm). Likewise, the diameter of the core was found to be ~200 μm, roughly the size of the core needle (27G / 210 μm). Fabrication of a smaller coaxial needle would overcome the challenge of producing smaller strands. However, the fabrication of such needle presents a challenge itself. Smaller core–shell strands would improve the printing resolution and consequently the banding that was present on printed constructs would become less pronounced. Cell viability through the needle was lower when extruded through a longer length needle (**Figure 4-3**) and is likely due to prolonged shear stress within the needle (Nichol *et al.*, 2010). 21 mm was the shortest core needle that could be manufactured with the coaxial configuration. The thickness of the shell has importance when considering the balance between nutrient delivery and structural integrity. A thin shell may promote nutrient diffusion, but may leave the printed construct weaker (Dai *et al.*, 2017; Zhang, Yu, Chen and Ozbolat, 2013).

The protein release studies were conducted for several reasons. Firstly, in order to successfully encapsulate cells in the core of a bioprinted strand, oxygen, nutrients and small proteins must be able to passively diffuse from the surrounding media through the shell and into the core.

Examples include hepatic growth factor to stimulate proliferation of hepatocytes in the cases of liver regeneration, and TGF β 1 for the differentiation of stem cells into chondrocytes during chondrogenesis, (Godoy et al., 2013; Tuli et al., 2003). Furthermore, hepatocytes also secrete a number of proteins, such as albumin, to carry out their function (Godoy et al., 2013). The shell material must therefore be porous enough to permit this diffusion. High gel concentrations may retard the diffusion of proteins, therefore the maximum concentration of alginate was limited to 3% in this work (Weber, Lopez and Anseth, 2009a; Lee, Tong and Yang, 2014; Holte, Tønnesen and Karlsen, 2006; Gao et al., 2015b). Secondly, in a regenerative medicine therapy, allogenic cells may be encapsulated to release therapeutic proteins. For example, pancreatic beta cells may be encapsulated for the release of insulin to control blood sugar levels. In this case, allogenic cells may initiate an undesired host immune response. Using a core-shell method, the allogenic cells can be confined to the core, isolated, and potentially be protected from the host antibodies by the shell material. The shell material in this case would have to inhibit the passage of high molecular weight proteins such as antibodies, whilst allowing the passage of lower molecular weight proteins such as insulin. To model both of these parameters, insulin (6.6 kDa) and IgG (150 kDa) were individually encapsulated in the core of the

printed strands. No significant differences were found between the alginate and hybrid material for both proteins, suggesting that the addition, and subsequent crosslinking, of PEGDA does not reduce the mesh size of the hybrid hydrogel network, at least for the molecular weights for the proteins studied. The printed constructs released over 85% of the smaller insulin and over 60% of the larger IgG. It is likely that the remaining 15% and 40%, respectively, remained entrapped within the core and the shell. Less of the larger protein, IgG (150 kDa), was released when compared to the smaller protein, insulin (6.6 kDa), suggesting that proteins with even higher molecular weights may be entrapped more and therefore released less. To increase encapsulation of IgG, a potential strategy could be to reduce the mesh size of the shell hydrogel by increasing hydrogel concentration. The protein release profiles and the swelling profiles of the hydrogels follow the same trend: both show rapid release and swelling followed by a plateau after 12 h, suggesting that two processes may be related. The rapid protein release may be attributed to the increase in the mesh size of the hydrogel network, which in turn is caused by the rapid swelling and uptake of water. As the hydrogel becomes fully swollen, the rate of protein release also plateaus. The release from the printed constructs agrees with

previous studies on alginate beads (Gray and Dowsett, 1988; Tanaka, Matsumura and Veliky, 1984).

Despite the large strand diameters, cells cultured within the core of the strands were able to receive enough oxygen and nutrients during culture and were able to proliferate and function in the printed constructs. One possible reason could be the low alginate concentration of the shell, 2%, opposed to higher concentrations used in other studies (Luo, Lode and Gelinsky, 2013). This chapter has demonstrated that different cell-types can be encapsulated within the core–shell strands and maintain good viability throughout culture. HepG2 cells were also shown to maintain their function during culture. The increase in albumin secretion appeared to be proportional to the amount of cell proliferation.

HepG2 cells were in the shell region when cultured in collagen (see **Appendix C**), suggesting that the collagen had intermixed with the shell material. This is possibly due to collagen being less viscous and more fluid when compared to Matrigel. Furthermore, the viability was only reduced for HepG2 cells in collagen using the hybrid shell. If the core and shell had intermixed during the printing process, the HepG2 cells could have come into contact with free radicals during the UV

crosslinking of the hybrid material, thus lowering their viability. Free radicals have shown to reduce cell viability during hydrogel crosslinking (Mironi-Harpaz, Wang, Venkatraman and Seliktar, 2012; Mazzoccoli *et al.*, 2010; Bryant, Nuttelman and Anseth, 2000). This would not be the case for alginate shell material as UV crosslinking was not involved.

HUVECs, endothelial cells, were selected in order to test the core–shell strands as a method of producing vascularised strands, and the formation of tubular structures was the evidence to support this. However, the maturation of the tubular structures took many weeks in this work and would not provide sufficient vascularisation until then. Therefore, the incorporation of pores is important to allow for nutrients to diffuse to the centre of printed constructs to prevent cell starvation. Whilst tall solid structures could be fabricated using the core–shell strands, tall porous structures could not. During the fabrication of a porous lattice, more than three layers, the weight of the upper layers caused the printed strands to collapse in the z-direction, causing the strands to coalesce and eliminating any introduced pores. The underlying layers were unable to support the weight of the upper layers in the printed construct.

In order to fabricate tall structures with interconnected pores, an alternative approach had to be taken to overcome this architectural challenge (**Figure 4-5**). Gelatine was selected as a sacrificial ink to provide support during the printing process. Gelatine was co-printed in between the core–shell strands and, once the shell material had been stabilised by crosslinking, it was later removed, revealing interconnected pores. A challenge in the fabrication of tall constructs arose in terms of crosslinking the hybrid hydrogel. The larger the constructs, the more the cumulative UV exposure time increased in order to fully crosslink the PEGDA hydrogel. As a result, the cell viability decreased. UV exposure time has been shown previously to impact cell viability in PEG hydrogels, through damage to DNA molecules (Gentile, Latonen and Laiho, 2003; Mironi-Harpaz *et al.*, 2012). To overcome this challenge, an alternative photoinitiator was sought out. The chosen photoinitiator, LAP, was able to crosslink PEGDA using light in the visible region of the spectrum, thus minimising cell death caused to prolonged cumulative UV exposure, allowing for the hydrogel to be fully crosslinked with live cells still present (**Figure 4-6**).

The co-printed core–shell strands, containing HUVECs and HepG2 cells resembles a simplified version of a liver sinusoid. This is a first step in the

generation of vascularised mini-tissues. By substituting the cell-types present, it may be possible to create vascularised mini-tissues of other organs. The alginate shell may be modified with RGD peptides in order to improve cell attachment (Lee, Kong, Larson and Mooney, 2003).

Finally, to assess the mechanical properties of the hybrid gel in a 3D construct, the hybrid hydrogel was printed in the shell of cell-laden core–shell strands. The compressive recovery for the hybrid hydrogel was >88% when crosslinked using either I-2959 or LAP as the photoinitiator, compared to 63.8% for the alginate hydrogels. This test was performed up to 50% strain, beyond the failure strain of alginate. Other literature has shown recovery of PEGDA-alginate hybrid hydrogels after compression to 95% strain, however those studies did not incorporate a core material and were composed of a greater proportion of PEGDA and alginate, up to a total hydrogel content of 45% (w/v), compared to 11% (w/v) in the shell material of this study (Hong et al., 2015).

Conclusion

To summarise, this chapter has shown:

- Partially crosslinking alginate can produce a printable ink that, through a coaxial needle, can produce core–shell strands.
- These core–shell strands can be patterned into 3D structures. Porous structures could be fabricated with a support of co-printed gelatine; solid structures did not require a support.
- Encapsulated proteins could be released when printed in a core-shell configuration, with the hybrid hydrogel as the shell material. The lower MW insulin was released more than the higher MW IgG.
- Cells printed in the core could survive the printing process and remaining viable during culture. HUVECs demonstrated the formation of a tubular structure and HepG2 cells demonstrated continued albumin secretion.
- HUVECs and HepG2 cells could co-printed in the core and shell, respectively, to form a miniaturised vascular tissue.
- Finally, printed constructs containing the hybrid hydrogel demonstrated improved recovery after compression when compared to alginate.

Chapter 5 – Incorporation of long-range gradients into bioprinted structures

Introduction

In the previous chapter, core–shell strands laden with cells were successfully printed, keeping cells viable and allowing them to maintain their function. To further improve the printed strands for physiologically relevance, gradients will be incorporated into the shell. Gradients occur naturally in the human body and are important in the maintenance of homeostasis. Gradients of soluble factors, such as growth factors, hormones and other small molecules, play a key role in embryonic development, and inflammation. Physical gradients, such as gradients of ECM components and material stiffness, play a role in liver sinusoids, controlling hepatocyte phenotype, and also in the interfaces between bone and soft tissues.

The fabrication of continuous gradients *in vitro* offers a system to study the cell response to increasing magnitudes of stimuli, helping to find threshold values specific to cell types. This can lead to improved biomaterial selection and scaffold design in tissue engineering (Singh, Berkland and Detamore, 2008).

3D printing has been used to incorporate gradients of pores, stiffness, and soluble factors into scaffolds (Sobral *et al.*, 2011; Woodfield *et al.*, 2004, 2005; Di Luca *et al.*, 2016). However these structures have created scaffolds that do not incorporate cells. A multi-material printhead using microfluidics has recently been used to fabricate cell-laden graded structures via extrusion-based printing.

In this chapter, the feasibility of incorporating gradients into bioprinted constructs will be investigated. In the previous chapter a core–shell bioprinting technique was developed (see **Chapter 4**). Here, gradients will be incorporated into the shell of these bioprinted core–shell strands. The first half of this chapter will explore gradients of soluble factors. The latter half of this chapter will explore gradients of material stiffness. The longevity of these gradients, and their impact on cells, will be examined.

Experimental design

For full details of methods, please refer to **Chapter 2**.

Synthesis of protein-loaded microparticles

Protein-loaded microparticles were kindly synthesised by Dr Omar Qutachi (University of Nottingham, UK) using a previously reported double emulsion method (Qutachi *et al.*, 2014). Microparticles loaded with FITC-BSA were used to characterise the release profiles. Microparticles loaded with TGFβ1 were synthesised for cell printing.

Fabrication of soluble factor gradients

Gradient printing was performed as described in **Chapter 2**.

Dyes and proteins were added to partially crosslinking alginate for gradient characterisation. Stains dissolved in diH_2O and filtered prior to the addition of alginate. Alcian blue, orange II, rhodamine B and BSA were all used at a concentration of 1 mg mL^{-1}. Acridine orange was used at 600 µg mL^{-1}. Printed constructs were cut into equal-sized portions and solubilised in a citrate buffer (55 mM sodium citrate, diH_2O; pH 7.4) to decrosslink the alginate. The strands were pipetted to aid in the decrosslinking. Decrosslinked solutions were examined using a microplate reader.

Core–shell bioprinting with a soluble factor gradient shell

Gradient printing was combined with a core to produce core–shell strands with a gradient shell. The core consisted of ihMSCs in 5% (w/v) GelMA (containing LAP), and the shell consisted of a gradient of TGFβ1-loaded microparticles. Microparticles were mixed with $CaCl_2$ at a density of 30 mg mL^{-1} prior to being syringe mixed with alginate, in the preparation of partially crosslinked alginate. Microparticles were used at a final density of 10 mg mL^{-1}, and were printed against alginate that did not contain microparticles. Rectangular constructs were printed, with dimensions of 80×20×0.8 mm. Calcium crosslinking buffer was added for 2 min to crosslink the alginate. The constructs were then exposed to visible light for 10 min to crosslink the GelMA core. The scaffolds were washed and incubated at 37°C.

Isolation of rat hepatic stellate cells

Isolation of rat hepatic stellate cells (RHSCs) was kindly performed by Dr Elke Gottschalg and Monika Owen (University of Nottingham, UK). Female rats were sacrificed, individual lobes were cut from their livers, and immediately placed in perfusion buffer (137 mM NaCl, 20 mM HEPES, 15 mM $NaHCO_3$, 5.6 mM glucose, 5.2 mM KCl, 2 mM methionine, 440 µM KH_2PO_4, 330 µM Na_2HPO_4, 10 µg mL^{-1} phenol red, diH_20; pH 7.4). The lobes were cannulated and perfused with perfusion buffer

containing 0.5 mM EGTA for 15 min at 37°C. The lobes were then perfused with perfusion buffer containing 0.5 mg mL^{-1} collagenase and 5 mM $CaCl_2$ for 12 min at 37°C. During perfusion, lobes were covered in a sterile gauze soaked in perfusion buffer to keep them moist. Following perfusion, the lobes were minced with scissors and filtered through a sterile gauze. The cells were centrifuged at 500 g_n for 15 min at 4°C. At this point, all work was carried out on ice, using ice-cold reagents. The supernatant was discarded and the pellet was resuspended in 5 mL of perfusion buffer. An equal volume of 40% Optiprep solution (40% (v/v) Optiprep Medium, 48.7 mM NaCl, 3.3 mM HEPES, diH_2O; pH 7.4) was thoroughly mixed with the cell suspension. The Optiprep-cell suspension was carefully overlaid with a 9% Optiprep solution (9% (v/v) Optiprep Medium, 114 mM NaCl, 25.6 mM HEPES, diH_2O; pH 7.4). The 9% Optiprep solution was further overlaid with a solution (10 mM HEPES, 146 mM NaCl, diH_2O; pH 7.4) producing three distinct layers. The cell suspension was centrifuged at 1400 g_n for 28 min at 4°C. The uppermost layer of the supernatant was discarded and the white band (RHSCs) present at the top of the 9% Optiprep solution layer was isolated. The cells were washed in 50 mL of stellate media, and centrifuged at 500 g_n for 15 min at 4°C. The supernatant was discarded and the cell pellet was resuspended in 10 mL of stellate media. 50 µL of cell suspension was

mixed with 50 µL of Trypan blue using a pipette. Trypan blue stains the cytoplasm of cells whose membranes have been compromised, indicating a dead cell. A haemocytomer was used to count the number of viable cells. RHSCs were only used if the viability of the isolated fraction was above 95%.

Immunostaining

Hydrogel samples were fixed in PFA overnight at 4°C. The fixed samples were incubated in 15% (w/v) sucrose for 1 h at 4°C, and then in 30% (w/v) sucrose overnight at 4°C. The samples were then cut into 10 µm slices via cryosectioning, and stored at −20°C. Cryosectioning was kindly performed by Denise McLean (University of Nottingham, UK). Cryosections were allowed to equilibrate to RT prior to immunostaining. During immunostaining, all samples were protected from light. Samples were rehydrated in PBS for 1 h at RT. The sections were blocked in blocking buffer (2% (w/v) BSA, 0.1% (v/v) Triton X-100, PBS) for 2 h at RT. The primary antibody was diluted in blocking buffer at 1:2000, added to sections, and left to incubate overnight at 4°C. The sections were washed three times in blocking buffer. The secondary antibody was diluted in blocking solution at 1:5000, added to sections, and left to incubate for 2 h at RT. The sections were washed again three times in blocking buffer,

and incubated with a 2 μg mL^{-1} Hoechst solution (in PBS) for 20 min. After this, the sections were washed three times in blocking buffer and imaged immediately.

Stiffness gradient bioprinting

RHSCs were resuspended in 5% GelMA (containing 4% gelatine) and 20% GelMA at a cell density of 1.5×10^5 cells mL^{-1}. Printing was done at RT and GelMA was placed on ice briefly until it had gelled. Rectangular constructs were printed, with dimensions of 80×20×0.8 mm. The constructs were exposed to visible light for 10 min to crosslink the GelMA. The scaffolds were washed in αMEM containing 1% (v/v) ABAM, and incubated at 37°C.

Characterisation of stiffness gradients by compression testing

5% (w/v) GelMA (containing 4% (w/v) gelatine) was printed against 20% (w/v) GelMA to produce a stiffness gradient. GelMA was prepared in αMEM containing 1% (v/v) AB/AM and 0.1% (w/v) LAP. Printing was done at RT and GelMA was placed on ice briefly until it had gelled. The gradient strand was printed into 10 individual 0.5×0.5×0.5 cm^3 cubes with no line spacing i.e. solid constructs. The constructs were crosslinked with visible light for 10 min. The hydrogels were then incubated in 3T3

culture media overnight to remove the gelatine, and then examined by compression testing, compressing the gels to 100% strain. For stability studies, the incubation time was increased to the indicated time points.

Results

Fabrication of soluble factor gradients

To produce gradients, two syringes, loaded onto two syringe pumps, were connected to each other via tubing and a Y-shaped connector. The connector fed into the outer needle of the coaxial needle, allowing for solid gradient fibres to be fabricated, with the potential for addition of a core, thus producing core-shell fibres with a gradient (see section 5.3.4). When no material is perfused in the inner needle (core), the material perfused in the outer needle (shell) fused and formed a solid strand.

The first step was the fabrication of solid strands with gradients. Two alginate inks, one containing Alcian blue dye, the other containing orange II dye, were loaded into two separate syringes and were printed simultaneously to produce a dual gradient (**Figure 5-1a**). The flow rate of the blue alginate was decelerated, from 0.1 mL min^{-1} to 0 min^{-1}, whilst, simultaneously, the flow rate of the orange alginate was accelerated from 0 mL min^{-1} to 0.1 mL min^{-1}. The maximum flow rate at any point was 0.1 mL min^{-1} as this was the flow rate to extrude core–shell strands (see **Chapter 4**). The acceleration and deceleration were both set to 12.5 µL min^{-2}. The printed strand gradually changed from orange to blue and the midsection of the printed strand appeared green, indicating mixture

of the two materials. Using the same printing parameters, the same strand was 3D printed into a solid 1×1×1 cm^3 cube (**Figure 5-1b**). The gradient was visible in the z-direction, showing the clear progression from orange, to green, to blue. To quantify the mixing within the gradient, the dyes were replaced with the fluorescent dyes rhodamine B and acridine orange. The printed strand was reproduced, divided into equal portions, and solubilised. The fluorescent intensities for each dye in each section of the strand were examined in order to quantitatively assess the gradient (**Figure 5-1c**). At the beginning of the strand, the presence of acridine orange was at maximum and, after 27 cm, the presence of the dye began to decrease. On the contrary, rhodamine B began at 0 and was immediately incorporated into the strand. After 117 cm, the presence of rhodamine B was at maximum and remained at maximum until the end of the gradient strand.

By varying the flow acceleration, gradients of different steepnesses could be achieved, those that were shallower and those that were steeper. Alcian blue-loaded alginate was co-printed with unloaded alginate, and the flow acceleration/deceleration were varied (**Figure 5-2**). The steepest gradient could be achieved with a flow acceleration of 6000 µL min^{-2}, reaching a maximum after 27 cm. The shallowest gradient could be

achieved with a flow acceleration of 6.3 μL min^{-2}, requiring 231 cm to reach maximum.

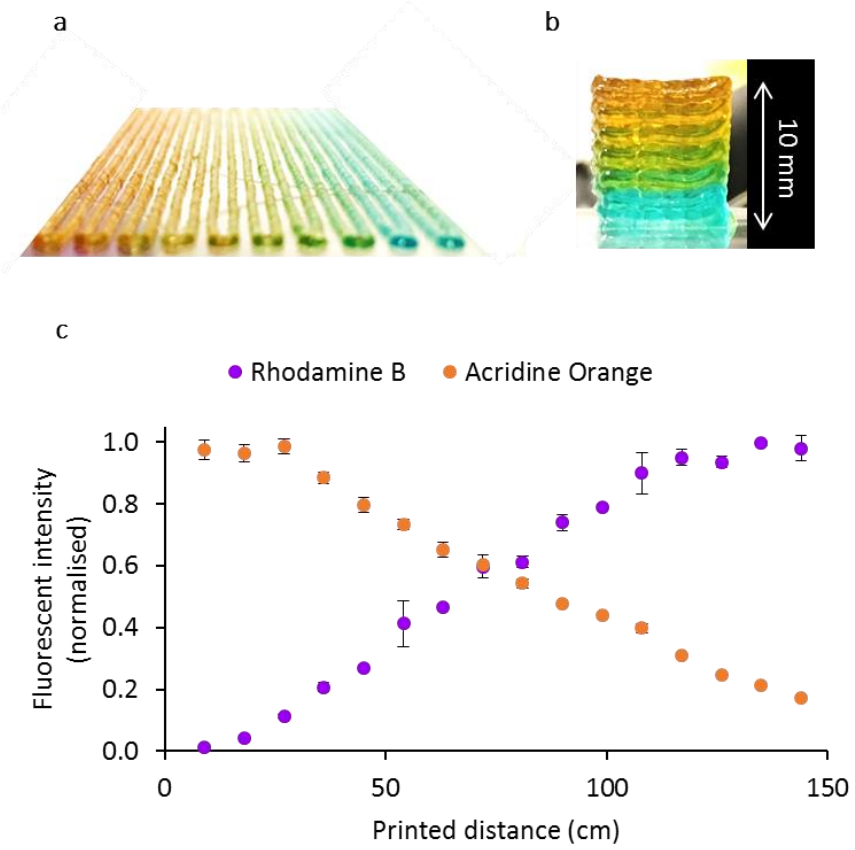

Figure 5-1 Printing of soluble factor gradients. To demonstrate the gradients, alginates containing different dyes were co-printed with varying flow rates. A) Alcian blue and Orange II dyes were co-printed to produce a solid strand. The alcian blue-loaded alginate was extruded with a flow deceleration of 12.5 µL min^{-2}. Simultaneously, the orange II-loaded alginate was extruded with a flow acceleration of 12.5 µL min^{-2}. a) A single continuous strand displaying the gradient along its length. b) The same strand was 3D printed into a 1×1×1 cm^3 cube. The gradient is visible in the z-direction. c) To quantify the opposing gradients, the printed strand in (a) was reproduced using the fluorescent dyes rhodamine B (555/580 nm) and acridine orange (488/526 nm). The strands were divided into equal portions, solubilised, and the fluorescent intensities of each dye were quantified. Data was normalised to their respective maximum values. Mean values were plotted. Error bars represent standard deviation (n = 3).

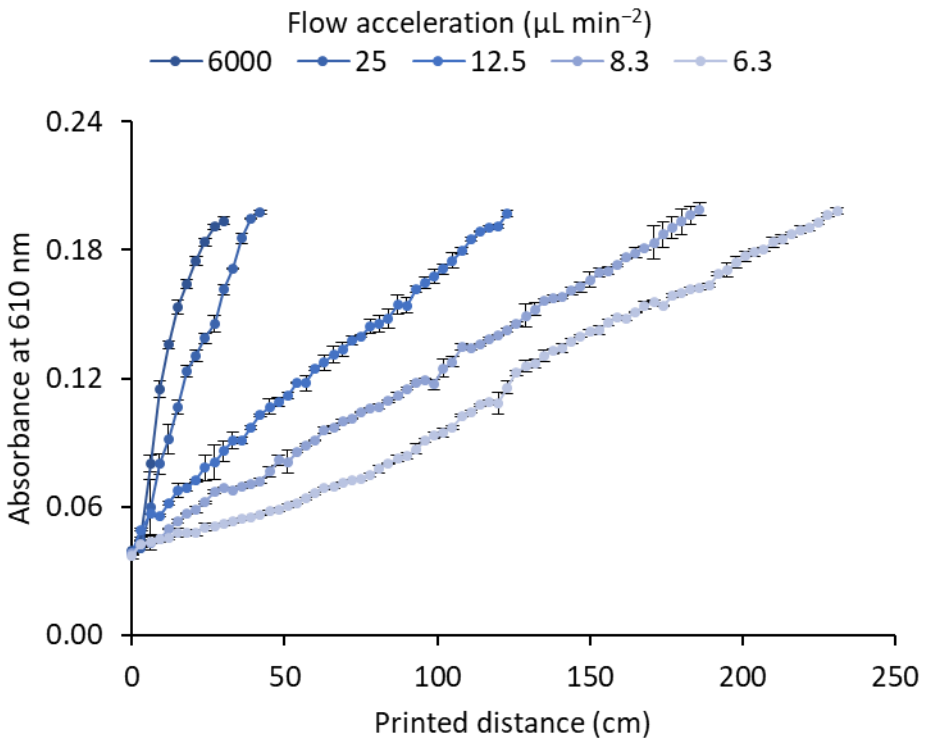

Figure 5-2 Varying the flow acceleration produced gradients of different steepnesses. Alcian blue-loaded alginate gradients were printed with varying flow accelerations. By adjusting the flow acceleration, gradients of different steepnesses were produced. To quantify the opposing gradients, the printed strands were divided into equal portions, solubilised, and the absorbance at 610 nm was measured. Mean values were plotted. Error bars represent standard deviation (n = 3).

Change of soluble factor gradient during incubation due to diffusion

The next step was to assess the stability of the printed gradients during incubation. Alginate inks were loaded with BSA to see how well maintained the gradients were. The printed strands were incubated in PBS at 37°C, and the BSA remaining in the strands were quantified (**Figure 5-3**). Three gradients, of different steepnesses were assessed, using flow accelerations of 6000, 12.5 and 6.3 µL min^{-2}. The amount of BSA remaining in the strands was quantified after 24 h and 48 h. After 24 h, the amount of BSA in the strands of all the gradients halved whilst still maintaining a gradient. For the shallowest gradient, the gradient plateaued at the upper region. After 48 h, however, there was no BSA remaining in any of the printed strands and the gradients had disappeared. This, in all, shows that, whilst gradients of soluble factors could be fabricated, a source for the gradients is required for the gradients to be maintained for relatively longer time periods.

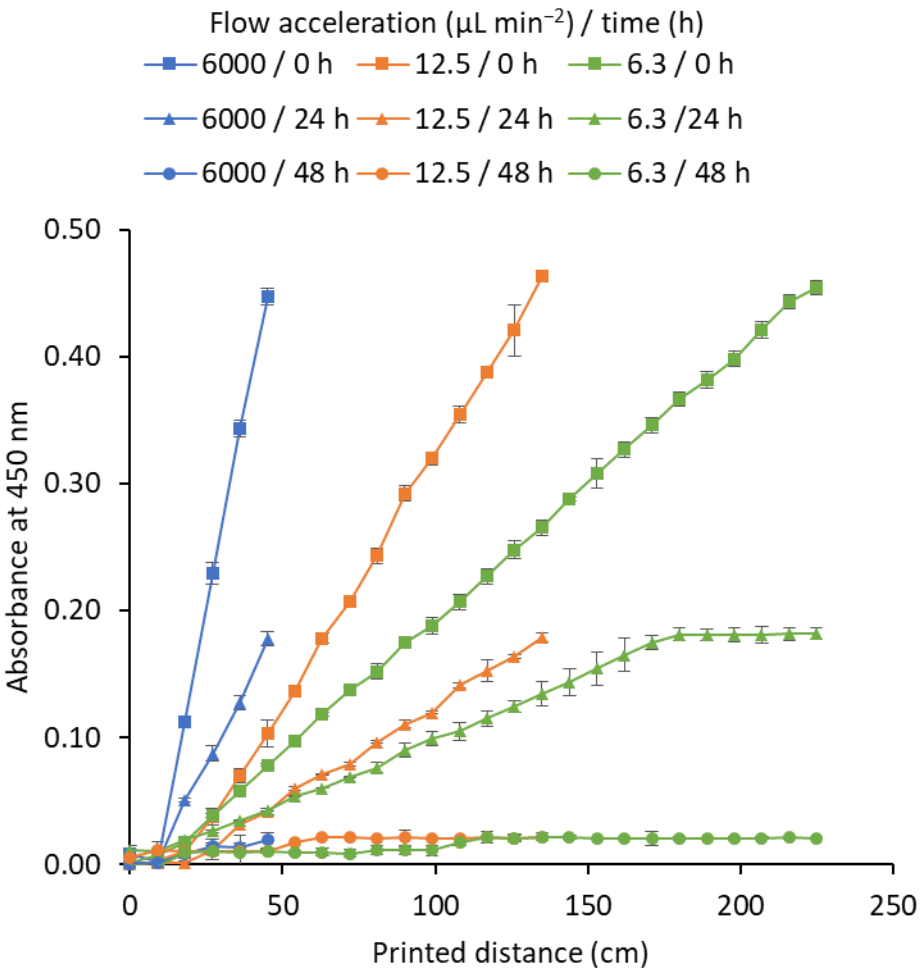

Figure 5-3 Soluble factor gradients dissipate due to diffusion. Alginate with BSA gradients were printed with varying flow accelerations. The strands were divided, placed in PBS at 37°C, and incubated for up to 48 h. At the indicated time points, the printed strands were solubilised, and the protein content was measured via Bradford's assay. Mean values were plotted. Error bars represent standard deviation (n = 3).

Protein loaded microparticles can prolong the gradients by slower release

To prolong the presence of soluble factor gradients, BSA-loaded microparticles were examined as a potential source. The continuous release of, for example, proteins would provide a way to maintain the gradients over longer periods of time. In order to create a gradient, a gradient of microparticles would be printed instead.

Microparticles, roughly 20 μm in diameter, porous and loaded with FITC-BSA were synthesised (**Appendix D**). These particles were incorporated into printed alginate strands (**Appendix D**). **Figure 5-4a** shows the microparticles in the printed strands at different positions along the gradient. By printing the particles in the same manner as a soluble factor, a gradient of microparticles was achieved. The stability of the gradient during incubation was once again assessed (**Figure 5-4b**). The 3D plot shows the cumulative release of the FITC-BSA from the particles over the 21 d time course. The lowest concentration region of the printed strand (0 – 27 cm) showed up to 20% release by day 21, compared to the highest concentration region (117 – 135 cm) which released up to 100%.

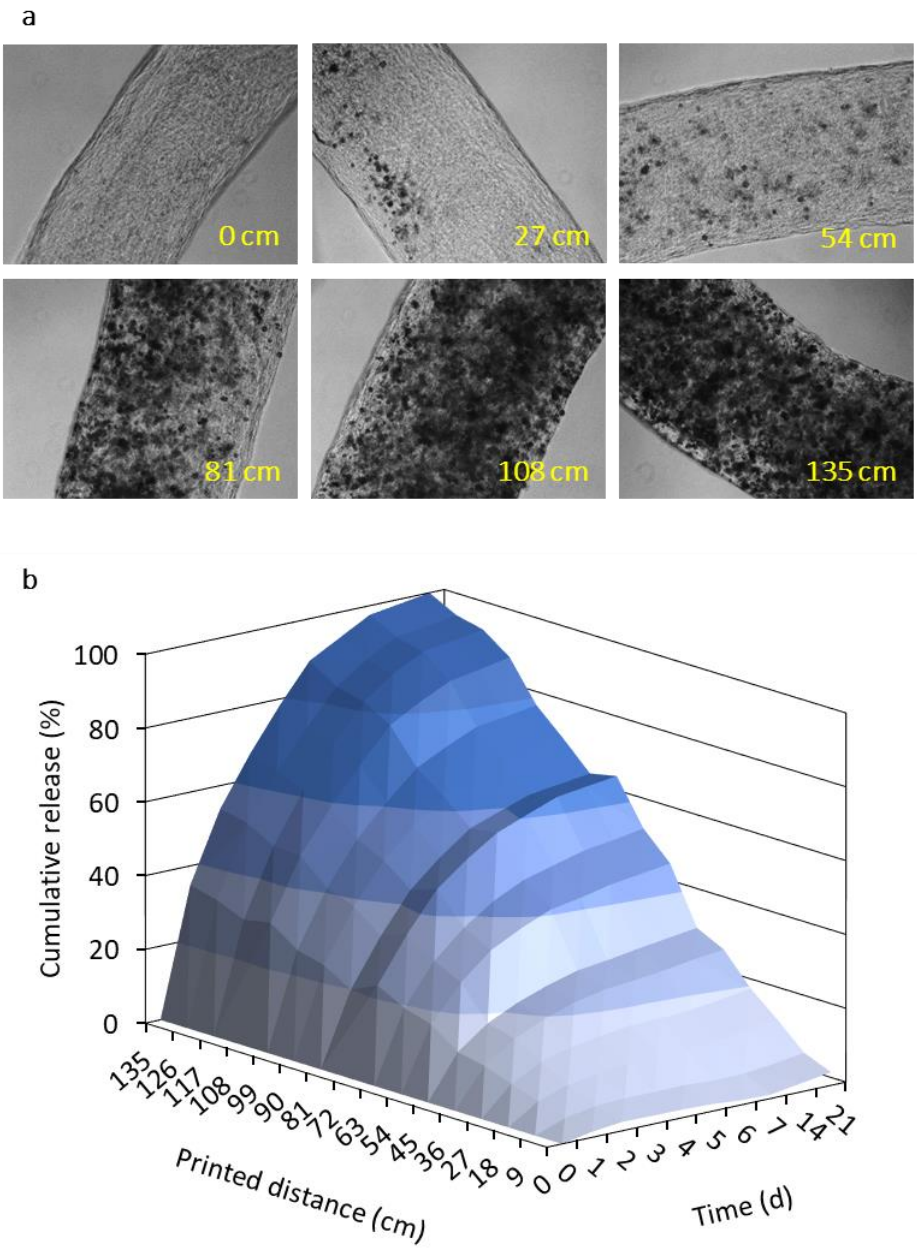

Figure 5-4 Protein-loaded microparticles can be printed as a source for soluble factor gradients. Microparticles loaded with FITC-BSA were synthesised and printed as a source for the gradient. (a) Light microscopy images of the microparticles in the printed strands labelled with their position along the strand. (b) The strands were divided into equal lengths (9 cm) and incubated in PBS at 37°C for up to 21 d. Release data was normalised to the maximum release of at the highest microparticle density. Mean values were plotted in 3D to show the gradient over the course of time.

Differentiation of ihMSCs along a gradient of TGFβ1

To assess cell response to the soluble factor gradient, microparticles loaded with TGFβ1 were synthesised, and ihMSCs were printed along a gradient of these particles to determine whether graded cell differentiation could be achieved. ihMSCs were first printed in the core of strands containing FITC-BSA-loaded microparticles to check that the core–shell configuration could still be achieved. The core–shell configuration was still visible (**Appendix D**).

Next, the core–shell strand technique was used to print strands with ihMSCs in a GelMA core surrounded by a gradient shell of TGFβ1-loaded microparticles in alginate (**Figure 5-5**). The metabolic activity of ihMSCs for all regions of the hydrogel remained steady, from after printing on day 0, until day 14 of culture, suggesting a lack of cell proliferation (**Figure 5-5a**). On day 28, the metabolic activity dropped for all regions, indicating a loss in cell viability. This was confirmed by the drop in cell number in the constructs stained with LIVE/DEAD (**Figure 5-5b-e**). The LIVE/DEAD staining shows that the cells, arranged in a core–shell configuration on day 0, began to migrate outwards into the shell material by day 1.

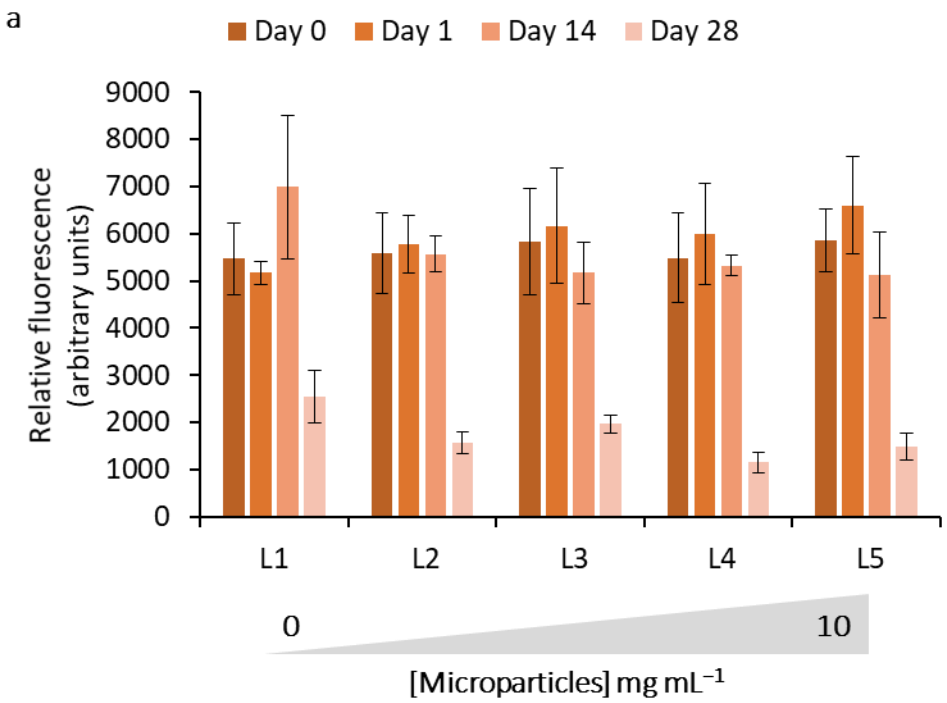

Figure 5-5 Metabolic activity and LIVE/DEAD staining of ihMSCs in a printed gradient of TGFβ1-loaded microparticles. ihMSCs were printed in the core of core–shell strands. The core consisted of ihMSCs and 5% (w/v) GelMA and the shell consisted of alginate with a gradient of TGFβ1-loaded microparticles. Metabolic activity of the ihMSCs was assessed using PrestoBlue® assay (a). Mean values were plotted. Error bars represent standard deviation. ihMSCs were stained with LIVE/DEAD® on day 0 (b), day 1 (c), day 14 (d) and day 28 (e). The microparticles also exhibited auto-fluorescence (red channel).

Figure 5-5b Day 0 ihMSCs in a gradient of TGFβ1-loaded microparticles.

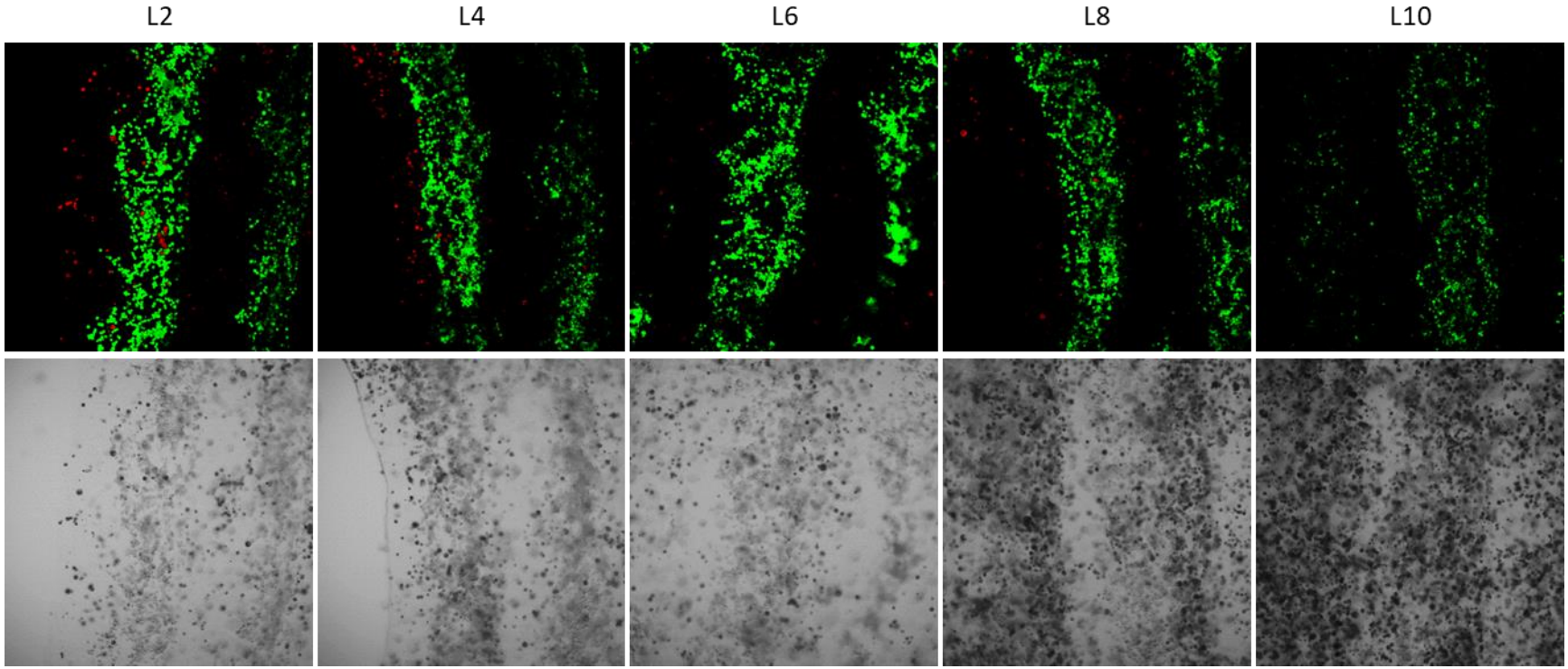

Figure 5-5c Day 1 ihMSCs in a gradient of TGFβ1-loaded microparticles.

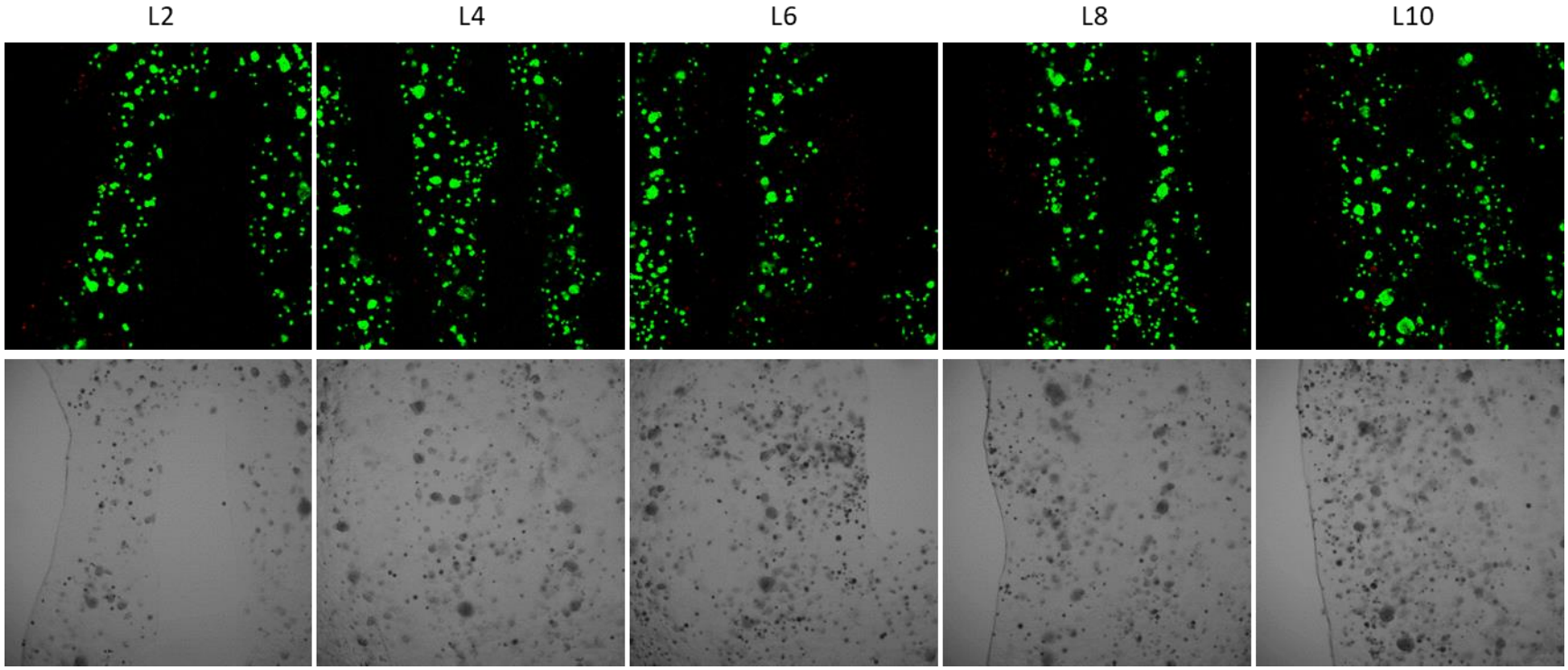

Figure 5-5d Day 14 ihMSCs in a gradient of TGFβ1-loaded microparticles.

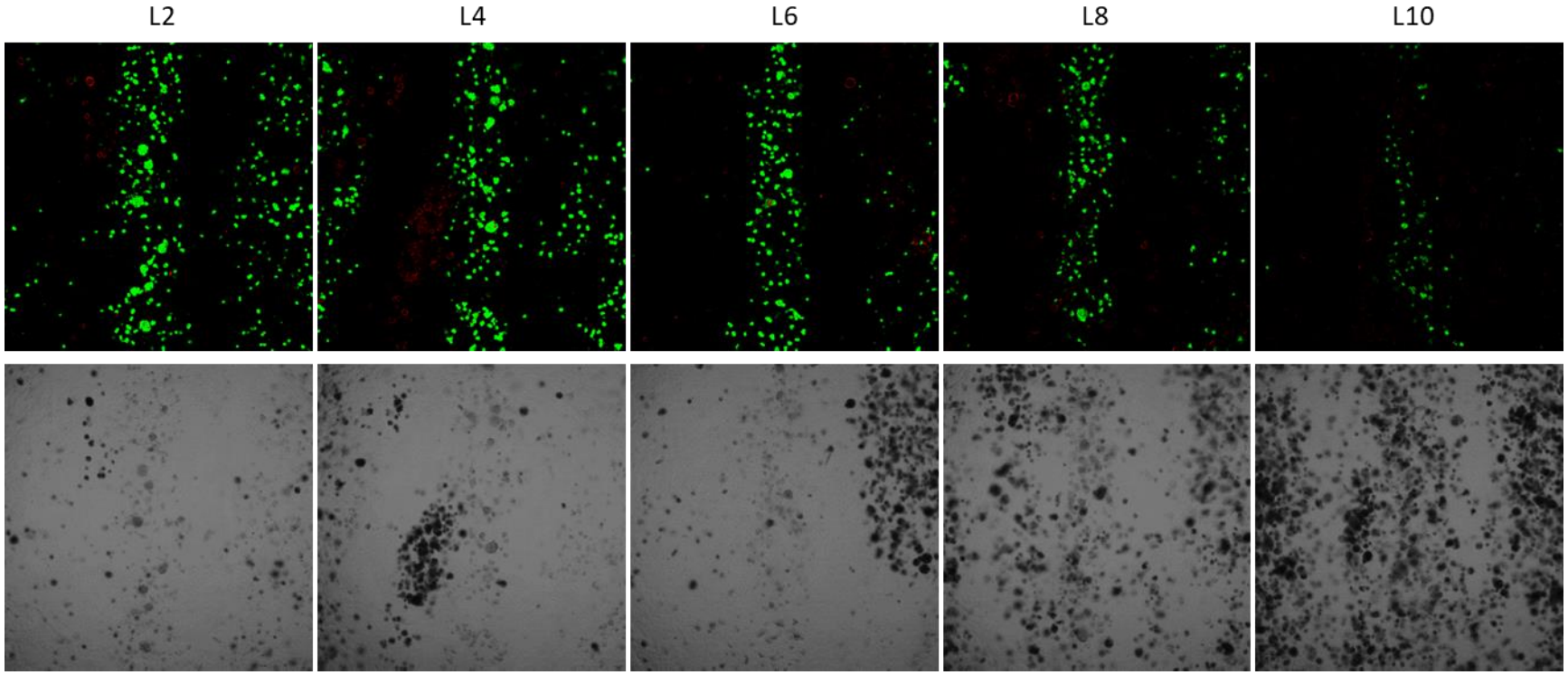

Figure 5-5e Day 28 ihMSCs in a gradient of TGFβ1-loaded microparticles.

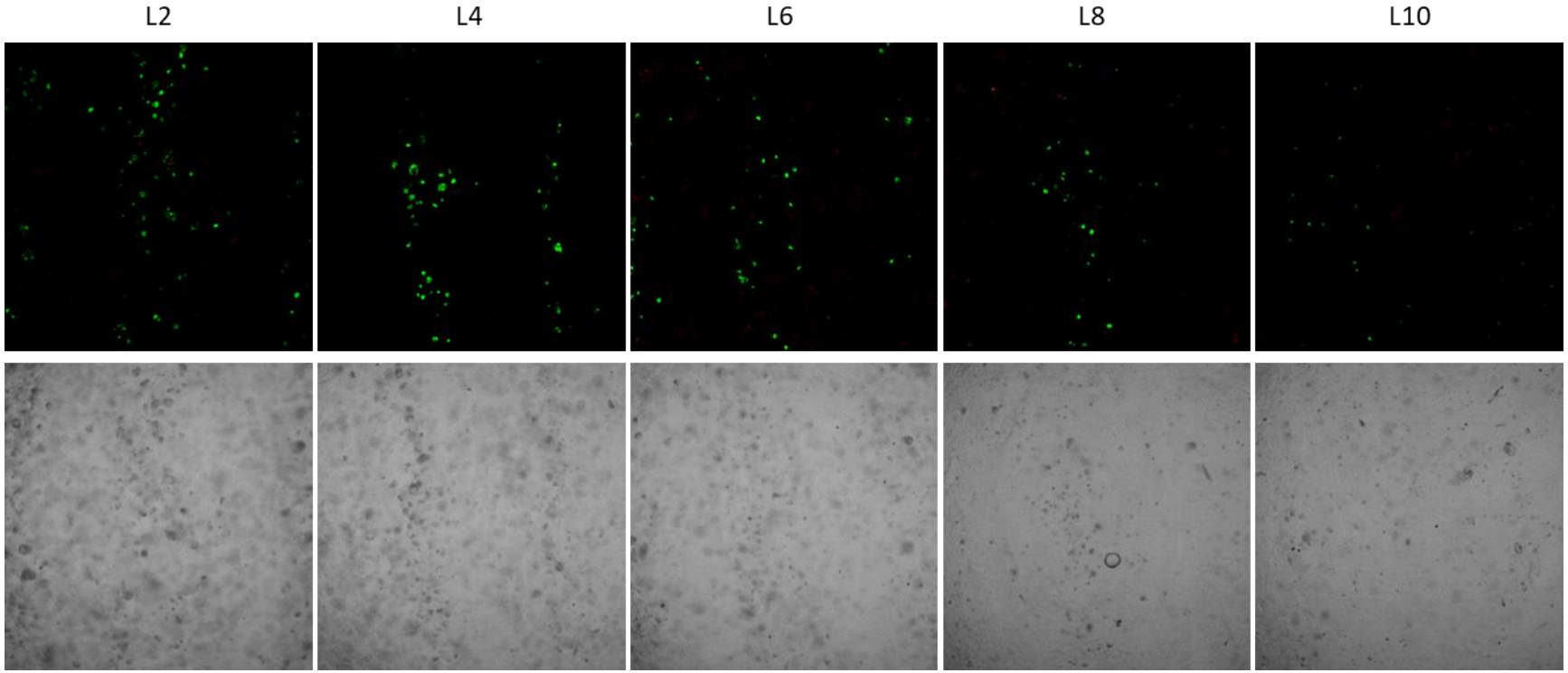

Fabrication of a gradient of stiffness by printing varying GelMA concentrations

In addition to soluble factor gradients, gradients of stiffness were also fabricated by substituting the co-printed materials for those with different mechanical properties. In this work, GelMA was co-printed at two different concentrations to produce a gradient of stiffness. To maximise the range of the stiffness gradient, the lowest concentration of GelMA chosen was one which could still form a stable hydrogel after crosslinking (**Appendix D**). 5% (w/v) and 20% (w/v) GelMA were co-printed into a strand of stiffness. 20% was printable at RT, however 5% was not viscous enough to be able to hold its shape after printing. To improve the printability of 5% GelMA, gelatine was added to increase the viscosity of the ink. The gelatine was removed in a later step by incubating the printed construct in an aqueous environment at 37°C (**Appendix D**). The gradient of stiffness was printed into individual 0.5×0.5×0.5 cm^3 cubes, crosslinked and incubated overnight at 37°C to remove the gelatine. The cubes were then assessed by compression testing. **Figure 5-6a** shows the elastic moduli of each construct. The elastic moduli increases from 12.0 kPa at L1, the 5% region, to 101.5 kPa at L10, the 20% region. The difference in strength between the constructs follows the same trend (**Figure 5-6b**). The strength also increases from 99.4 kPa at L1 to 922.5 kPa at L10.

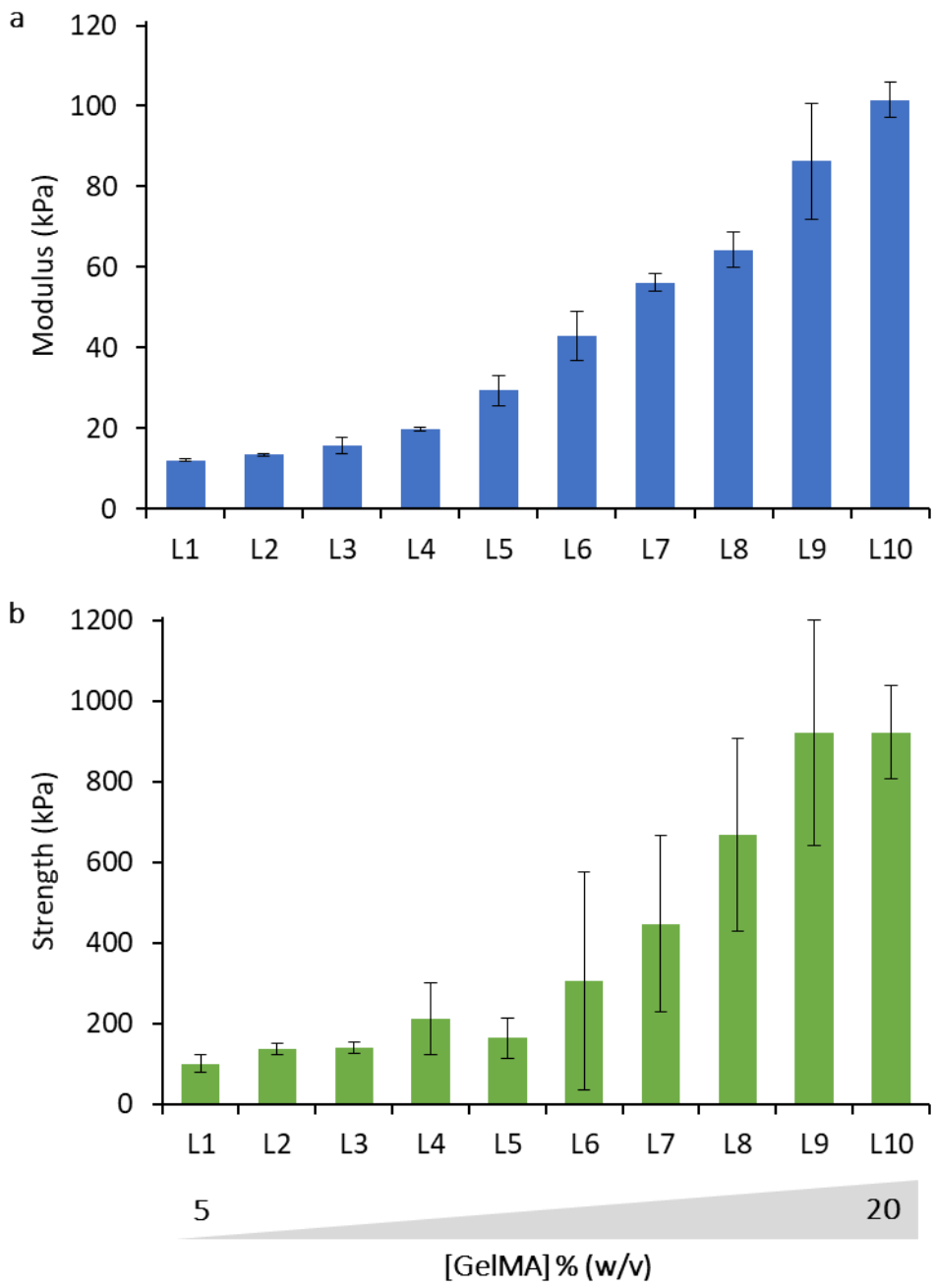

Figure 5-6 GelMA concentration gradients results in a gradient of elastic modulus and strength. A GelMA concentration gradient was printed by co-printing 5% (w/v) GelMA with 20% (w/v) GelMA. The gradient strand was printed into 10 cubes, and each were examined by compression testing to examine their elastic modulus (a) and strength (b). The flow acceleration/deceleration was fixed at 12.5 µL min^{-2}. Mean values were plotted. Error bars represent standard deviation (n = 3).

GelMA stiffness gradients are stable during incubation

To assess the stability of the GelMA stiffness gradients during incubation, GelMA stiffness gradients were fabricated and incubated at 37°C for up to 4 weeks. During this time, the change in elastic modulus and strength of each construct was assessed (**Figure 5-7**). The stiffness gradient remained intact during the 28 d of incubation, changing very little at L1. At L10, there was a slight drop in elastic modulus from 101.5 kPa on day 1 to 92.1 on day 28 (**Figure 5-7a**). There was a greater change in the strength of the hydrogel: at L1, the strength fell from 99.4 kPa on day 1 to 53.3 kPa on day 28. Likewise, at L10, the strength fell from 922.5 kPa on day 1 to 740.2 kPa on day 28. There decrease for L8 and L9 was more pronounced, falling from 667.5 kPa and 921.5 kPa on day 1 to 285.2 kPa and 424.7 kPa on day 28, respectively (**Figure 5-7b**). In general, there is a decrease in mechanical properties of the overall gradient construct after 28 days of incubation. This decrease is more pronounced for strength in comparison to the elastic modulus.

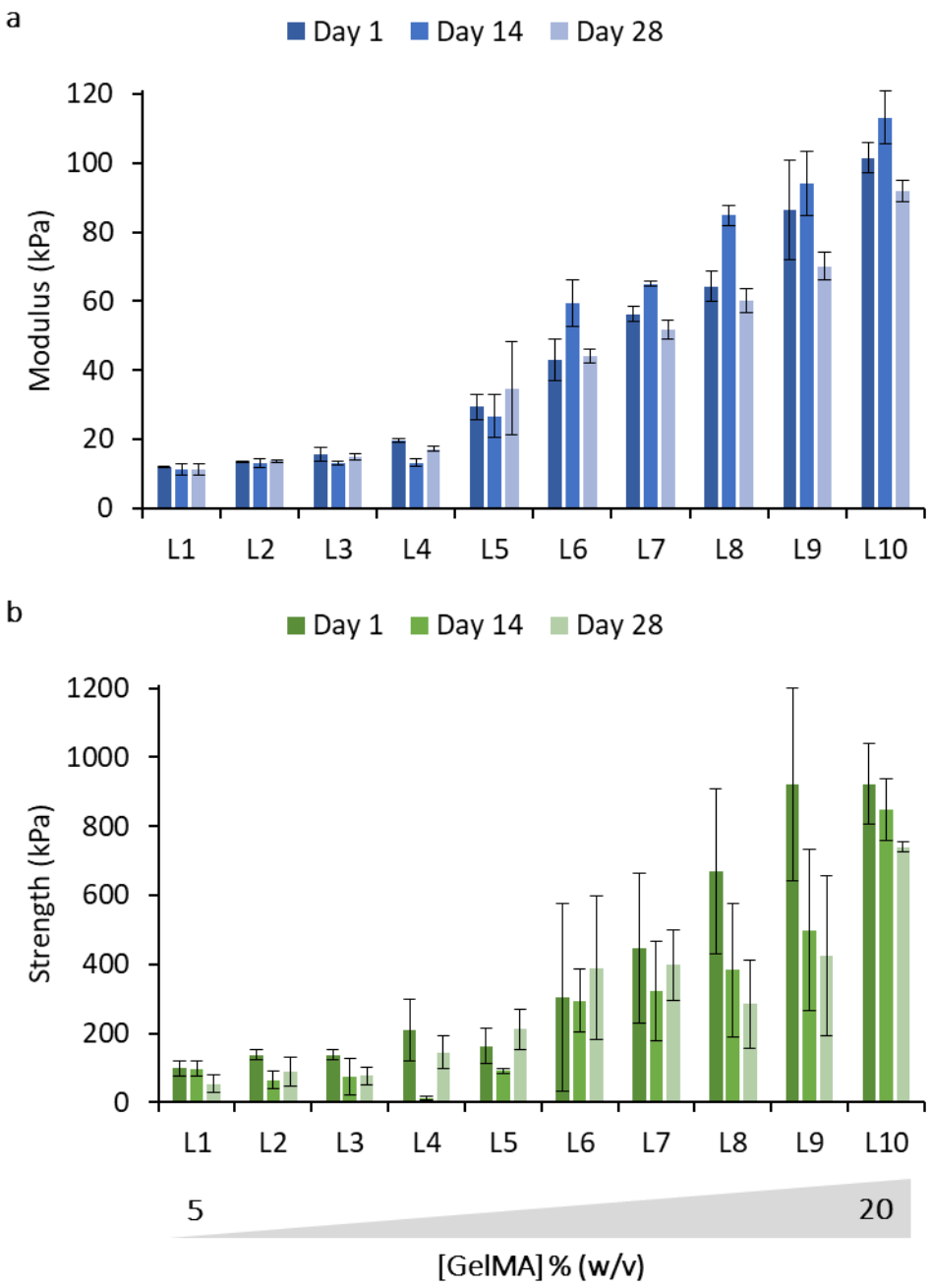

Figure 5-7 Stability of GelMA stiffness gradients during incubation. GelMA stiffness gradients were printed and incubated at 37°C. At the indicated time-points, the elastic moduli and strength of each construct were assessed by compression testing. Mean values were plotted. Error bars represent standard deviation (n = 3).

Rat hepatic stellate cells behaviour on GelMA stiffness gradients

The next step was to examine cell response in the stiffness gradient. Rat hepatic stellate cells (RHSCs) were isolated from rat livers and printed in the GelMA stiffness gradient.

The viability of the cells did not vary between the different regions of GelMA stiffness (**Figure 5-8a**). Overall, the viability showed a slight decreasing trend, starting at 90.3% on day 0 after printing and falling to 73.4% by day 14. There was little, if no, change in the morphology of the stellate cells in any of the regions of stiffness (**Figure 5-8b**). The RHSCs remained rounded and did not demonstrate any migration, remaining as single cells or small clusters.

The constructs were fixed and cryosections were taken from the terminal ends of the gradient hydrogel, the stiffer end L10, and the softer end L1. The sections were stained for the presence of αSMA (green), a marker of hepatic stellate cell activation, and counterstained with Hoescht (blue), to visualise the cell nuclei (**Figure 5-9**). For RHSCs in the L10 region, the staining showed the presence of αSMA on day 7 and day 14 for some of the cells. These cells were rounded in morphology. The RHSCs in the L1 region, there was no staining of αSMA present for any of the time-points.

However, despite this, the positive staining in the sections was scarce; only a few cells are present in the slices, and even fewer showed any staining. Furthermore, only cells from each end of the scaffold, the stiffest and softest regions, were examined by immunostaining. To better examine the effect of stiffness on RHSCs, sections need to be taken across the whole construct in order to see how the morphology and expression of αSMA changes along the stiffness gradient. The cells that did stain positive were also clustered, which may have impacted their gene expression.

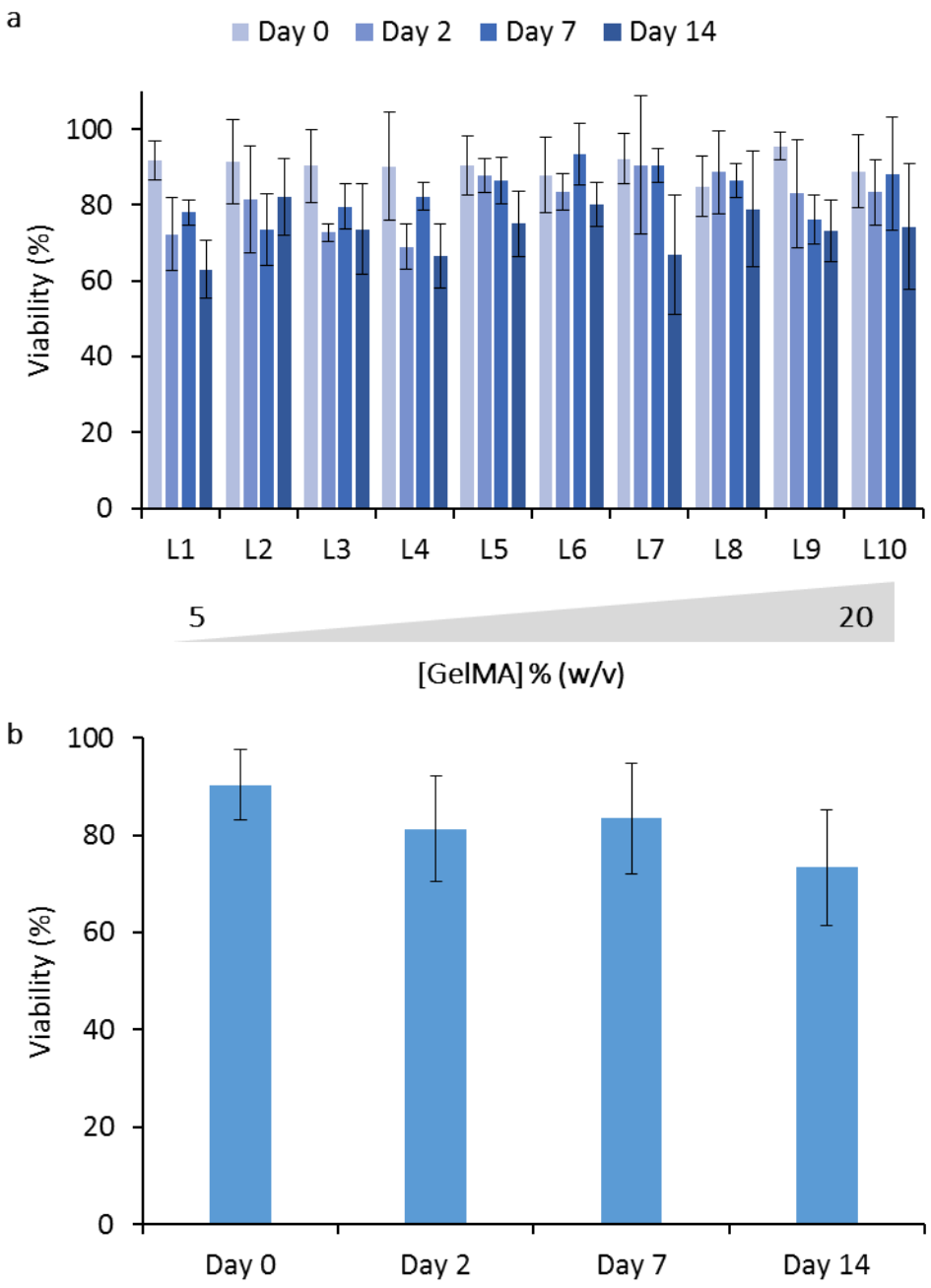

Figure 5-8 Viability of RHSCs in a GelMA stiffness gradient. RHSCs were printed in a GelMA stiffness gradient. Cells were stained with LIVE/DEAD at the indicated time points. (a) Live and dead cells were counted and viability was calculated for each region of the gradient hydrogel. Mean values were plotted. Error bars represent standard deviation (n =3). (b) The overall viability of the RHSCs in the whole construct. Error bars represent standard deviation. (c) Morphology of RHSCs in the GelMA gradient.

Figure 5-8b Morphology of RHSCs in printed GelMA stiffness gradients. Cells were stained with LIVE/DEAD (green/red).

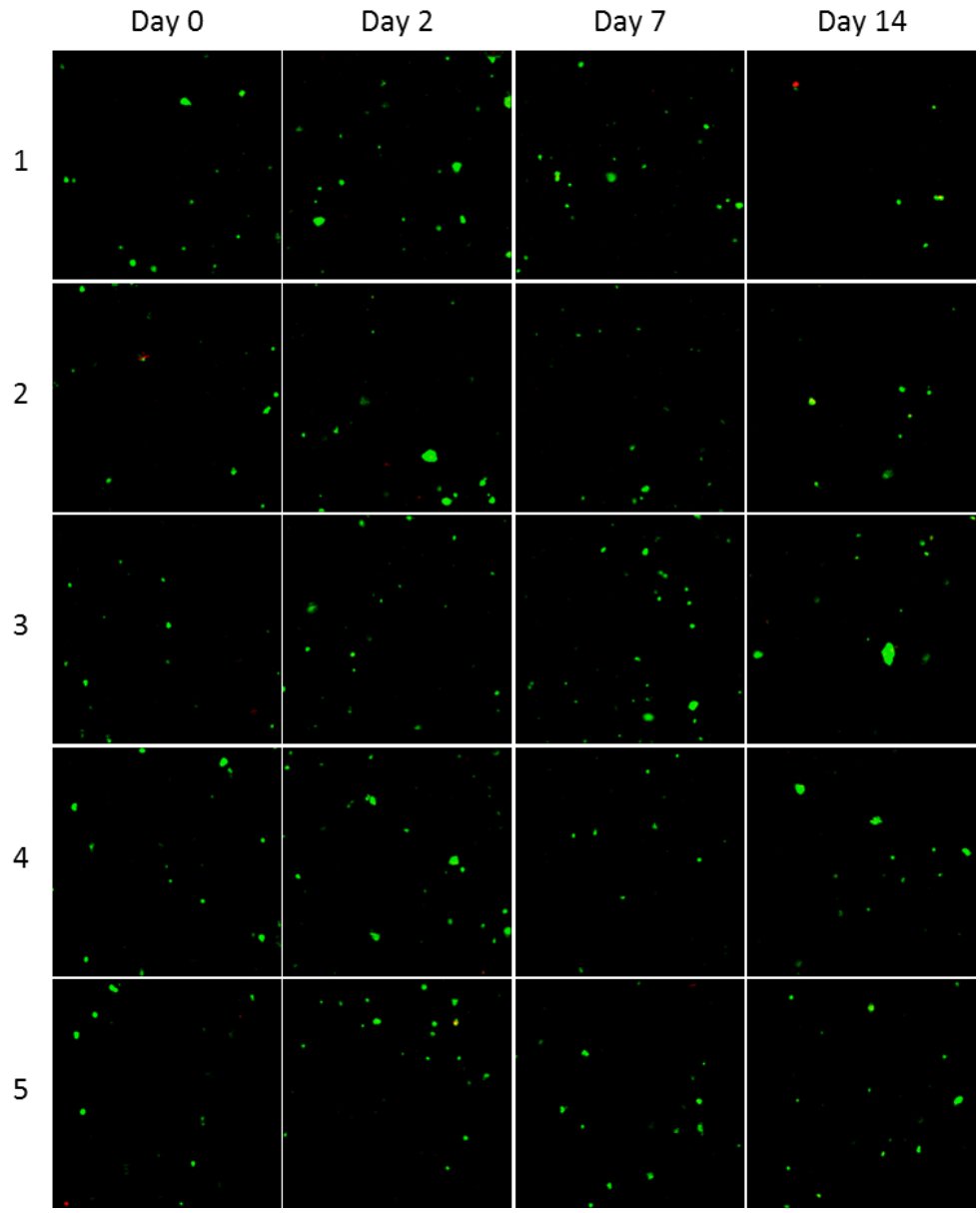

Figure 5-8c Morphology of RHSCs in printed GelMA stiffness gradients. Cells were stained with LIVE/DEAD (green/red).

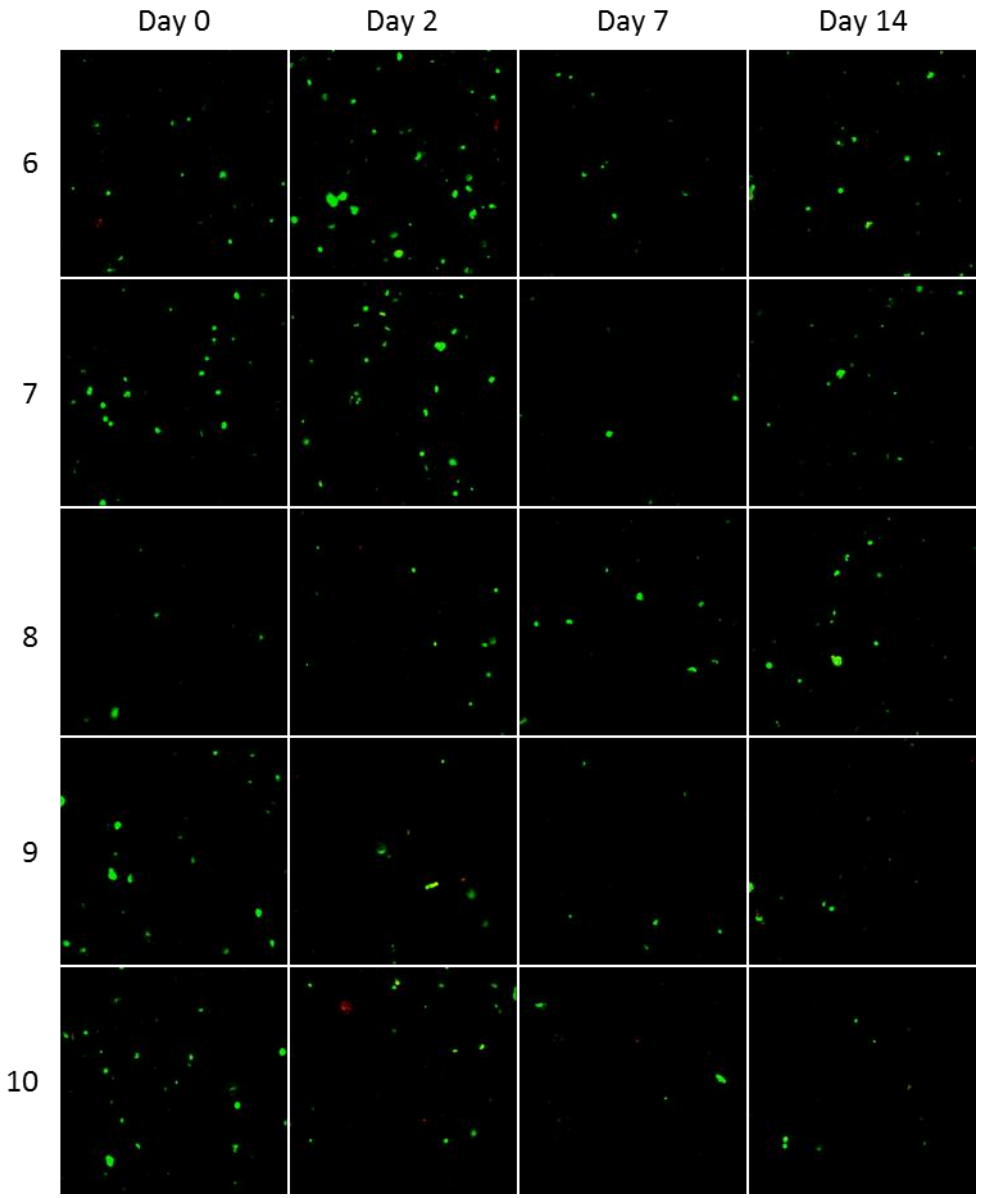

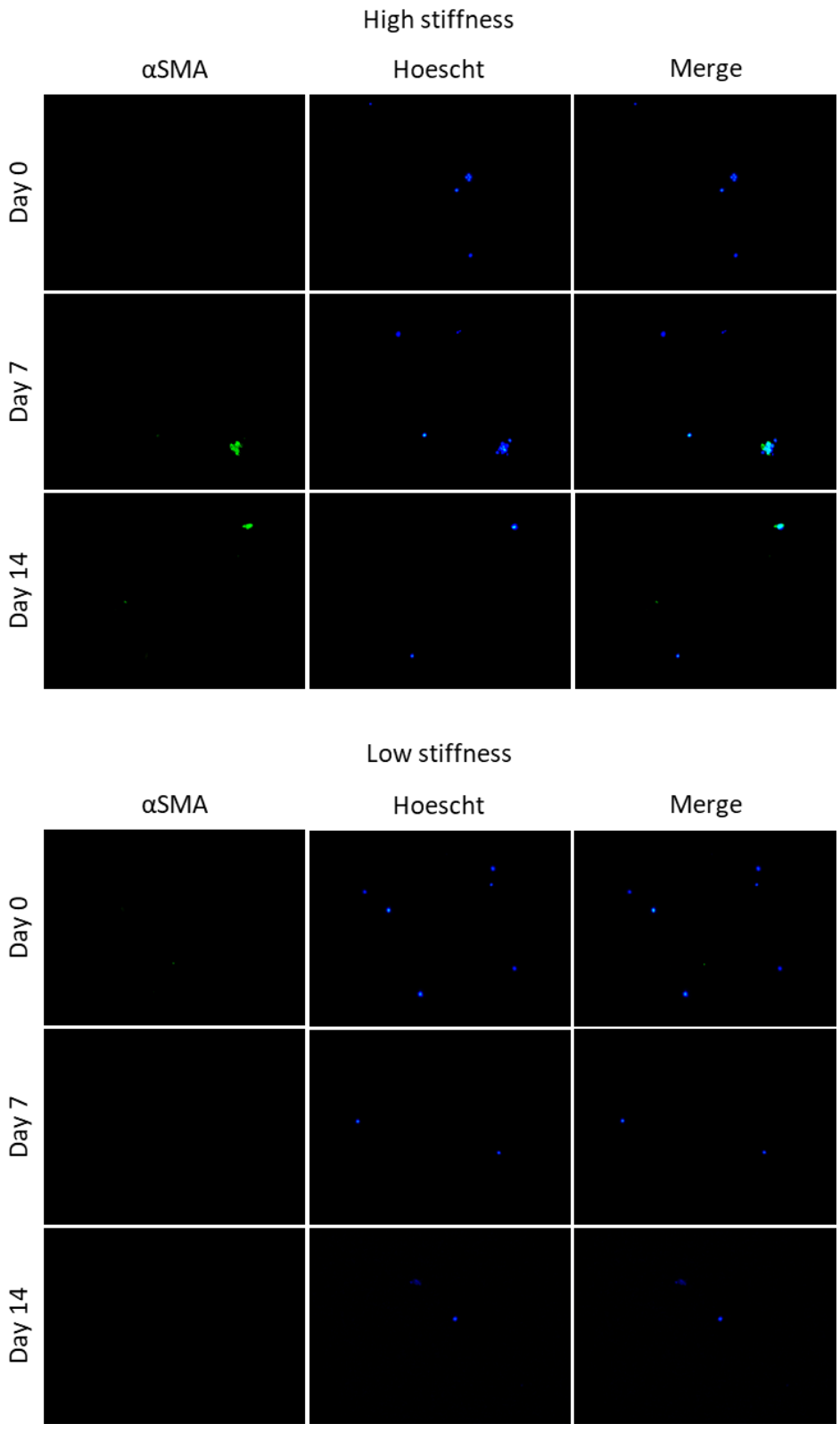

Figure 5-9 Representative images showing immunostaining of RHSCs. RSHCs, printed in a GelMA stiffness gradient, were cryosectioned and stained for the presence of αSMA (green). Cell nuclei were counterstained with Hoescht (blue).

Discussion

The aim of this chapter was to incorporate continuous gradients into 3D printed constructs with core–shell strands. This was made possible by simultaneously accelerating and decelerating two materials. Varying the materials co-printed allowed the fabrication of soluble factor gradients (**Figure 5-1**) and stiffness gradients (**Figure 5-6**). The use of the same base ink with an added component allowed the fabrication of a single gradient. By using two different soluble factors, reciprocating gradients could be fabricated in a single bioprinting step. The gradients fabricated in this work were continuous, and not graded (Liu *et al.*, 2017). Furthermore, due to the long-distance gradients, the shape of the printed construct will have an impact on the distribution of the gradient.

A challenge of soluble factor gradients is their maintenance: if the pore size of the hydrogel network is too large to trap the soluble factor, that factor will diffuse and thus dissipate the fabricated gradient. For soluble factors that do not require uptake into the cell (i.e. act only on cell membrane receptors), immobilisation of the factor to the printed hydrogel can overcome this (Sant *et al.*, 2010). In this work, to overcome this challenge, protein-loaded microparticles were synthesised and printed in the gradient hydrogel. 20 µm diameter microparticles were

chosen, roughly 10× smaller than the coaxial slot diameter (distance between the outer needle wall and inner needle wall) to prevent needle clogging. Furthermore, porous microparticles were synthesised to reduce burst release in favour of sustained release for the long differentiation process.

Whilst surviving the printing process and up to 14 days of culture, the printed ihMSCs demonstrated a sharp drop in viability by day 28, as highlighted by their reduced metabolic activity and the few cells that were stained with calcein-AM (stain for live cells). The fall in cell viability may be due to quick degradation of the PLGA microparticles. The degradation of PLGA produces the acidic by-product lactic acid and glycolic acid, resulting a local drop in pH within the hydrogel, creating an unfavourable environment for the cells (Sung, Meredith, Johnson and Galis, 2004; Holy, Dang, Davies and Shoichet, 1999). This is backed by the noticeable decrease in the number of particles within the hydrogel at later time points (**Figure 5-5b-e**).

Due to technical challenges and time constraint, gene expression data could not be obtained to assess the differentiation of these cells. The

combination of microparticles and hydrogels created challenges in obtaining sufficient quantities of RNA with adequate purity.

Soluble factor gradients were shown to lose their gradients when incubated for longer than 24 h. As a result, it was important to examine the longevity of the stiffness gradients. It was shown that stiffness gradients maintain their gradient of moduli for up to 28 days, showing minimal changes. However, the strength of the hydrogels diminished. The individual differences at each point along the stiffness gradient may be attributed to uneven mixing, another aspect of gradient fabrication, but one that has not been studied in this work (Hardin *et al.*, 2015; Ober, Foresti and Lewis, 2015).

To examine the effect of stiffness on cell response, freshly isolated rat hepatic stellate cells (RHSCs) were printed in the GelMA stiffness gradient. HSCs are one of the major four cell-types in the liver and, whilst normally rounded and quiescent, undergo myofibroblast differentiation and play a major role in liver fibrosis. Myofibroblast differentiation of these cells results in a stellate phenotype, and the expression and secretion of αSMA and abnormal ECM, respectively. Previous studies have shown that a stiffness <3 kPa allows HSCs to remain in a quiescent

state, and a stiffness >20 kPa results in their myofibroblast differentiation (Olsen *et al.*, 2011; Caliari *et al.*, 2016; Guvendiren, Perepelyuk, Wells and Burdick, 2014; Saums *et al.*, 2014). Here, RHSCs were cultured in 3D and were stained to observe their morphology and the presence of αSMA, a marker of myofibroblast differentiation. In this work, GelMA was used in the concentration range of 5% – 20%, corresponding to a stiffness range of 12 kPa – 102 kPa. 5% was the lower limit of GelMA which could be crosslinked into a stable hydrogel. Hydrogels of lower stiffnesses may be fabricated by tuning the mechanical properties of GelMA, or by swapping GelMA for another material (Yoon *et al.*, 2016; Nichol *et al.*, 2010).

Whilst above the previously reported threshold of 3 kPa, RHSCs in 12 kPa GelMA did not show expression of αSMA. However in the previous studies, HSCs were cultured in 2D. The RHSCs in this study did demonstrate myofibroblast differentiation in the maximal stiffness region of the GelMA hydrogel (102 kPa). The RHSCs in this work remained rounded throughout culture and did not display the myofibroblast phenotype. This may be due to physical confinement within the 3D hydrogel network (Baker and Chen, 2012).

Conclusion

To summarise, this chapter has shown:

- Soluble factor gradients, both single and dual factor, and stiffness gradients could be fabricated by the simultaneous acceleration and deceleration of two materials during the printing process.
- Soluble factor gradients dissipated after 48 h of incubation, but could be prolonged (up to 21 days) by using a gradient of loaded microparticles as the source.
- Stiffness gradients retained their gradient of elastic moduli up to 28 days, however the strength of the hydrogel diminished greatly.
- RHSCs cultured in GelMA stiffness gradients demonstrated little expression of αSMA where the matrix was 102 kPa, however this result is inconclusive.

Chapter 6 – Conclusion and future directions

In the pursuit of functional human tissue equivalents, either for tissue repair and organ replacement in the long-term, and *in vitro* models for drug testing and disease modelling in the short-term, there are a great deal of challenges. These challenges stem from the complexity of human physiology, where cells are in a unique environment, with a combination of mechanical, physical and chemical properties. 3D printing is promising for this field, allowing cells to be deposited with spatial control. Furthermore advances in extrusion-based bioprinting brings the long-term goals a step closer.

This thesis has explored three aspects of bioprinting in order to fabricate constructs with optimal biological and mechanical properties. In **Chapter 3**, a biocompatible, yet mechanically-robust double network hydrogel was examined. PEGDA and alginate interacted in a synergistic manner, displaying improved strength and elastic modulus when compared to their individual components. Three compositions of PEGDA/alginate hybrid hydrogels were examined, along with two MWs of PEGDA, and each hybrid hydrogel displayed its own unique mechanical properties. However, no general trend was gathered from the results presented here

and further work is required to better predict the tunability of these hybrid hydrogels. The alginate in this work was crosslinked using calcium ions. Barium ions are known to crosslink alginate more strongly, and could be explored to further increase the resilience of these hydrogels. Barium ions would also slow degradation of the hydrogels, an aspect that has not been studied in this thesis.

The purpose of this hybrid hydrogel was for use as a mechanically robust shell material that could withstand *in vitro* manipulation for core–shell strand bioprinting. A single composition of hybrid hydrogel was brought forward and combined with coaxial bioprinting in **Chapter 4** in order to fabricate core–shell strands with a mechanically robust shell and a cell-laden core. To overcome challenges with viscosities, the alginate in this study was partially crosslinked. This reduced the crosslinking time required post-printing, and lowered the hydrogel content required, allowing for greater nutrient diffusion. Using a core–shell morphology, different hydrogels could be incorporated into the core of the strands, even those that have low viscosities and cannot form 3D structures without support, such as collagen and Matrigel. Bioprinted HepG2 cells in the core demonstrated high viability for up to 28 days culture, and maintained their function during this time. It would be interesting to

culture primary hepatocytes in the core, using materials that would promote their function *in vitro*. The core–shell technique removes the requirement of the bioink to be printable; the material only needs to be extrudable. HUVECs were shown to form tubular structures in the core and, by co-printing a second cell type in the shell, mini-vascularised tissues could also be fabricated using this technique. One aspect that was not studied was the perfusability of the HUVEC tubes. It would be interesting to see if flow could be introduced. The diffusion of proteins through the shell was also examined in this work. For *in vivo* implantation, however, the 9:2 composition was not sufficient to block diffusion of IgG antibody through the shell material. Another composition may be able to block this diffusion, and immune-protective properties of that material would help bioprinted constructs containing allogenic cells to be implanted. Only proteins were released from the core of the printed constructs. For drug delivery applications, the release of other therapeutic molecules could also be studied. Changing the core and shell materials may affect entrapment of these molecules and control their release.

To further develop these bioprinted core–shell strands so that they better mimic *in vivo* physiology, the incorporation of gradients was

explored in **Chapter 5**. Both gradients of stiffness and soluble factors could be fabricated, and it was shown that, whilst stiffness gradients could be maintained for 28 days, soluble factor gradients required a source to maintain the gradient in the printed constructs. RHSCs printed in stiffness gradients little showed expression of αSMA, a marker for myofibroblast differentiation, at the stiffer end of the printed constructs. However, the presence of cells that stained positive was scarce, and the regions examined did not represent the whole of the scaffold. The differentiation of ihMSCs across a soluble factor gradient could not be assessed in this work due to time constraints, and would be interesting to study further. Gradients were only incorporated in the shell of the core–shell strands in this work. An interesting approach could be to incorporate gradients within the core of the strands too. It would also be interesting to combine both soluble factor gradients and stiffness gradients together in a single construct.

In summary, core–shell strands have been shown to be a viable method to combine two hydrogels, one which is mechanical-robust and supportive, with another that contains biological properties, into a single construct. This technique can be made more complex, and more

physiologically relevant, with the addition of gradients in the shell. These techniques may allow cells to be recapitulated into a construct that closer mimics their *in vivo* environment. The core-shell technique, combined with gradients, will help to create more physiologically relevant tissue engineered constructs which can move a step closer towards future therapies.

Bibliography

Adams, M. a, Kerin, a J., and Wisnom, M.R., 1998. Sustained loading increases the compressive strength of articular cartilage. *Connective tissue research*, 39(4), pp.245–256.

Akkineni, A.R., Ahlfeld, T., Lode, A., and Gelinsky, M., 2016. A versatile method for combining different biopolymers in a core/shell fashion by 3D plotting to achieve mechanically robust constructs. *Biofabrication*, 8(4), p.45001.

Alsberg, E., Anderson, K.W., Albeiruti, A., Franceschi, R.T., and Mooney, D.J., 2001. Cell-interactive Alginate Hydrogels for Bone Tissue Engineering. *Journal of dental research*, 80(11), pp.2025–2029.

Ambrosio, L., De Santis, R., and Nicolais, L., 1998. Composite hydrogels for implants. *Proceedings of the Institution of Mechanical Engineers, Part H: Journal of Engineering in Medicine*, 212(2), pp.93–99.

Bajaj, P., Schweller, R.M., Khademhosseini, A., West, J.L., and Bashir, R., 2014. 3D Biofabrication Strategies for Tissue Engineering and Regenerative Medicine. *Annual review of biomedical engineering*, 16, pp.247–76.

Baker, B.M., and Chen, C.S., 2012. Deconstructing the third dimension – how 3D culture microenvironments alter cellular cues. *Journal of Cell Science*, 125(13), pp.3015–3024.

Barbetta, A., Colosi, C., Costantini, M., Latini, R., Ciccarelli, S., Stampella, A., Massimi, M., Conti Devirgiliis, L., and Dentini, M., 2014. Rapid Prototyping of Chitosan-Coated Alginate Scaffolds Through the Use of a 3D Fiber Deposition Technique. *Journal of Materials Chemistry B*, 2, pp.6779–6791.

Basta, G., Montanucci, P., Luca, G., Boselli, C., Noya, G., Barbaro, B., Qi, M., Kinzer, K.P., Oberholzer, J., and Calafiore, R., 2011. Long-term metabolic and immunological follow-up of nonimmunosuppressed patients with type 1 diabetes treated with microencapsulated islet allografts: Four cases. *Diabetes Care*, 34(11), pp.2406–2409.

Billiet, T., Gevaert, E., De Schryver, T., Cornelissen, M., and Dubruel, P., 2014. The 3D printing of gelatin methacrylamide cell-laden tissue-engineered constructs with high cell viability. *Biomaterials*, 35(1), pp.49–62.

Bracaglia, L.G., Smith, B.T., Watson, E., Arumugasaamy, N., Mikos, A.G.,

and Fisher, J.P., 2017. 3D printing for the design and fabrication of polymer-based gradient scaffolds. *Acta Biomaterialia*, 56, pp.3–13.

Bryant, S.J., Nuttelman, C.R., and Anseth, K.S., 2000. Cytocompatibility of UV and visible light photoinitiating systems on cultured NIH/3T3 fibroblasts in vitro. *Journal of Biomaterials Science, Polymer Edition*, 11(5), pp.439–457.

Van Den Bulcke, A.I., Bogdanov, B., De Rooze, N., Schacht, E.H., Cornelissen, M., and Berghmans, H., 2000. Structural and rheological properties of methacrylamide modified gelatin hydrogels. *Biomacromolecules*, 1(1), pp.31–38.

Caliari, S.R., Perepelyuk, M., Cosgrove, B.D., Tsai, S.J., Lee, G.Y., Mauck, R.L., Wells, R.G., and Burdick, J.A., 2016. Stiffening hydrogels for investigating the dynamics of hepatic stellate cell mechanotransduction during myofibroblast activation. *Scientific Reports*, 6(1), p.21387.

Cavallo, A., Madaghiele, M., Masullo, U., Lionetto, M.G., and Sannino, A., 2017. Photo-crosslinked poly(ethylene glycol) diacrylate (PEGDA) hydrogels from low molecular weight prepolymer: Swelling and permeation studies. *Journal of Applied Polymer Science*, 134(2), pp.1–9.

Chang, R., Nam, J., and Sun, W., 2008. Effects of Dispensing Pressure and Nozzle Diameter on Cell Survival from Solid Freeform Fabrication–Based Direct Cell Writing. *Tissue Engineering Part A*, 14(1), pp.41–48.

Chen, H., Yang, F., Hu, R., Zhang, M., Ren, B., Gong, X., Ma, J., Jiang, B., Chen, Q., and Zheng, J., 2016a. A comparative study of the mechanical properties of hybrid double-network hydrogels in swollen and as-prepared states. *Journal of Materials Chemistry B*, 4(35), pp.5814–5824.

Chen, Q., Chen, H., Zhu, L., and Zheng, J., 2016b. Engineering of Tough Double Network Hydrogels. *Macromolecular Chemistry and Physics*, 217(9), pp.1022–1036.

Chung, J.H.Y., Naficy, S., Yue, Z., Kapsa, R., Quigley, A., Moulton, S.E., and Wallace, G.G., 2013. Bio-ink properties and printability for extrusion printing living cells. *Biomaterials Science*, 1(7), p.763.

Colosi, C., Shin, S.R., Manoharan, V., Massa, S., Costantini, M., Barbetta, A., Dokmeci, M.R., Dentini, M., and Khademhosseini, A., 2016a. Microfluidic Bioprinting of Heterogeneous 3D Tissue Constructs Using Low-Viscosity Bioink. *Advanced Materials*, 28(4), p.677–684a.

Colosi, C., Shin, S.R., Manoharan, V., Massa, S., Costantini, M., Barbetta, A., Dokmeci, M.R., Dentini, M., and Khademhosseini, A., 2016b.

Supporting Information: Microfluidic Bioprinting of Heterogeneous 3D Tissue Constructs Using Low-Viscosity Bioink. *Advanced Materials*, 28(4), p.677–684a.

Cravedi, P., Farouk, S., Angeletti, A., Edgar, L., Tamburrini, R., Dusuit, J., Perin, L., and Orlando, G., 2017. Regenerative immunology: the immunological reaction to biomaterials. *Transplant International*, 38(1), pp.42–49.

Czarnecki, S., Rossow, T., and Seiffert, S., 2016. Hybrid polymer-network hydrogels with tunable mechanical response. *Polymers*, 8(3), pp.1–16.

Dai, X., Liu, L., Ouyang, J., Li, X., Zhang, X., Lan, Q., and Xu, T., 2017. Coaxial 3D bioprinting of self-assembled multicellular heterogeneous tumor fibers. *Scientific Reports*, 7(1), p.1457.

Datta, P., Ayan, B., and Ozbolat, I.T., 2017. Bioprinting for vascular and vascularized tissue biofabrication. *Acta Biomaterialia*, 51, pp.1–20.

Demirbag, B., Huri, P.Y., Kose, G.T., Buyuksungur, A., and Hasirci, V., 2011. *Advanced cell therapies with and without scaffolds*. *Biotechnology Journal*, .

Dhoot, N.O., Tobias, C.A., Fischer, I., and Wheatley, M.A., 2004. Peptide-modified alginate surfaces as a growth permissive substrate for neurite outgrowth. *Journal of Biomedical Materials Research - Part A*, 71(2), pp.191–200.

Diniz, I.M.A., Chen, C., Xu, X., Ansari, S., Zadeh, H.H., Marques, M.M., Shi, S., and Moshaverinia, A., 2015. Pluronic F-127 hydrogel as a promising scaffold for encapsulation of dental-derived mesenchymal stem cells. *Journal of Materials Science: Materials in Medicine*, 26(3), pp.1–10.

Discher, D.E., Janmey, P., and Wang, Y.-L., 2005. Tissue cells feel and respond to the stiffness of their substrate. *Science (New York, N.Y.)*, 310(5751), pp.1139–43.

Engler, A.J., Sen, S., Sweeney, H.L., and Discher, D.E., 2006. Matrix Elasticity Directs Stem Cell Lineage Specification. *Cell*, 126(4), pp.677–689.

Fairbanks, B.D., Schwartz, M.P., Bowman, C.N., and Anseth, K.S., 2009. Photoinitiated polymerization of PEG-diacrylate with lithium phenyl-2,4,6-trimethylbenzoylphosphinate: polymerization rate and cytocompatibility. *Biomaterials*, 30(35), pp.6702–6707.

Faulkner-Jones, A., Greenhough, S., King, J. a, Gardner, J., Courtney, A., and Shu, W., 2013. Development of a valve-based cell printer for the formation of human embryonic stem cell spheroid aggregates.

Biofabrication, 5, p.15013.

Gao, G., Du, G., Sun, Y., and Fu, J., 2015a. Self-healable, tough, and ultrastretchable nanocomposite hydrogels based on reversible polyacrylamide/montmorillonite adsorption. *ACS Applied Materials and Interfaces*, 7(8), pp.5029–5037.

Gao, Q., He, Y., Fu, J., Liu, A., and Ma, L., 2015b. Coaxial nozzle-assisted 3D bioprinting with built-in microchannels for nutrients delivery. *Biomaterials*, 61, pp.203–215.

Gentile, M., Latonen, L., and Laiho, M., 2003. Cell cycle arrest and apoptosis provoked by UV radiation-induced DNA damage are transcriptionally highly divergent responses. *Nucleic Acids Research*, 31(16), pp.4779–4790.

Godoy, P., Hewitt, N.J., Albrecht, U., Andersen, M.E., Ansari, N., Bhattacharya, S., Bode, J.G., Bolleyn, J., Borner, C., Böttger, J., Braeuning, A., Budinsky, R. a, Burkhardt, B., Cameron, N.R., Camussi, G., Cho, C.-S., Choi, Y.-J., Craig Rowlands, J., Dahmen, U., Damm, G., Dirsch, O., Donato, M.T., Dong, J., Dooley, S., Drasdo, D., Eakins, R., Ferreira, K.S., Fonsato, V., Fraczek, J., Gebhardt, R., Gibson, A., Glanemann, M., Goldring, C.E.P., Gómez-Lechón, M.J., Groothuis, G.M.M., Gustavsson, L., Guyot, C., Hallifax, D., Hammad, S., Hayward, A., Häussinger, D., Hellerbrand, C., Hewitt, P., Hoehme, S., Holzhütter, H.-G., Houston, J.B., Hrach, J., Ito, K., Jaeschke, H., Keitel, V., Kelm, J.M., Kevin Park, B., Kordes, C., Kullak-Ublick, G. a, LeCluyse, E.L., Lu, P., Luebke-Wheeler, J., Lutz, A., Maltman, D.J., Matz-Soja, M., McMullen, P., Merfort, I., Messner, S., Meyer, C., Mwinyi, J., Naisbitt, D.J., Nussler, A.K., Olinga, P., Pampaloni, F., Pi, J., Pluta, L., Przyborski, S. a, Ramachandran, A., Rogiers, V., Rowe, C., Schelcher, C., Schmich, K., Schwarz, M., Singh, B., Stelzer, E.H.K., Stieger, B., Stöber, R., Sugiyama, Y., Tetta, C., Thasler, W.E., Vanhaecke, T., Vinken, M., Weiss, T.S., Widera, A., Woods, C.G., Xu, J.J., Yarborough, K.M., and Hengstler, J.G., 2013. *Recent advances in 2D and 3D in vitro systems using primary hepatocytes, alternative hepatocyte sources and non-parenchymal liver cells and their use in investigating mechanisms of hepatotoxicity, cell signaling and ADME. Archives of toxicology*, .

Gong, J.P., 2010. Why are double network hydrogels so tough? *Soft Matter*, 6(12), p.2583.

Gong, J.P., Katsuyama, Y., Kurokawa, T., and Osada, Y., 2003. Double-network hydrogels with extremely high mechanical strength. *Advanced Materials*, 15(14), pp.1155–1158.

Guillotin, B., and Guillemot, F., 2011. Cell patterning technologies for

organotypic tissue fabrication. *Trends in Biotechnology*, 29(4), pp.183–190.

Guillotin, B., Souquet, A., Catros, S., Duocastella, M., Pippenger, B., Bellance, S., Bareille, R., Rémy, M., Bordenave, L., Amédée, J., and Guillemot, F., 2010. Laser assisted bioprinting of engineered tissue with high cell density and microscale organization. *Biomaterials*, 31(28), pp.7250–6.

Guvendiren, M., Perepelyuk, M., Wells, R.G., and Burdick, J.A., 2014. Hydrogels with differential and patterned mechanics to study stiffness-mediated myofibroblastic differentiation of hepatic stellate cells. *Journal of the Mechanical Behavior of Biomedical Materials*, 38, pp.198–208.

Haraguchi, K., and Takehisa, T., 2002. Nanocomposite hydrogels: A unique organic-inorganic network structure with extraordinary mechanical, optical, and swelling/De-swelling properties. *Advanced Materials*, 14(16), pp.1120–1124.

Hardin, J.O., Ober, T.J., Valentine, A.D., and Lewis, J.A., 2015. Microfluidic printheads for multimaterial 3D printing of viscoelastic inks. *Advanced Materials*, 27(21), pp.3279–3284.

Holy, C.E., Dang, S.M., Davies, J.E., and Shoichet, M.S., 1999. In vitro degradation of a novel poly (lactide-co-glycolide) 75 / 25 foam. *Changes*, 20(13), pp.1177–1185.

Hong, S., Sycks, D., Chan, H.F., Lin, S., Lopez, G.P., Guilak, F., Leong, K.W., and Zhao, X., 2015. 3D Printing of Highly Stretchable and Tough Hydrogels into Complex, Cellularized Structures. *Advanced Materials*, p.n/a-n/a.

Hutmacher, D.W., 2000. Scaffolds in tissue engineering bone and cartilage. *Biomaterials*, 21(24), pp.2529–2543.

Itagaki, H., Kurokawa, T., Furukawa, H., Nakajima, T., Katsumoto, Y., and Gong, J.P., 2010. Water-induced brittle-ductile transition of double network hydrogels. *Macromolecules*, 43(22), pp.9495–9500.

Jiang, F., Huang, T., He, C., Brown, H.R., and Wang, H., 2013. Interactions affecting the mechanical properties of macromolecular microsphere composite hydrogels. *Journal of Physical Chemistry B*, 117(43), pp.13679–13687.

Khattak, S.F., Bhatia, S.R., and Roberts, S.C., 2005. Pluronic F127 as a cell encapsulation material: utilization of membrane-stabilizing agents. *Tissue Eng.*, 11(5–6), pp.974–83.

Khetani, S.R., and Bhatia, S.N., 2008. Microscale culture of human liver cells for drug development. *Nature biotechnology*, 26(1), pp.120–6.

Kim, B.S., and Mooney, D.J., 1998. Development of biocompatible synthetic extracellular matrices for tissue engineering. *Trends in Biotechnology*, 16(5), pp.224–229.

Kinstlinger, I.S., Bastian, A., Paulsen, S.J., Hwang, D.H., Ta, A.H., Yalacki, D.R., Schmidt, T., and Miller, J.S., 2016. Open-Source Selective Laser Sintering (OpenSLS) of nylon and biocompatible polycaprolactone. *PLoS ONE*, 11(2), pp.1–25.

Kloxin, A.M., Benton, J.A., and Anseth, K.S., 2010. In situ modulation with dynamic substraes to direct cell phenotype. *NIH Public access Author manuscript*, 31(1), pp.1–8.

Koch, L., Gruene, M., Unger, C., and Chichkov, B., 2013. Laser assisted cell printing. *Current pharmaceutical biotechnology*, 14(1), pp.91–7.

Kolesky, D.B., Truby, R.L., Gladman, a S., Busbee, T. a, Homan, K. a, and Lewis, J. a, 2014. 3D bioprinting of vascularized, heterogeneous cell-laden tissue constructs. *Advanced materials (Deerfield Beach, Fla.)*, 26(19), pp.3124–30.

Kong, H.J., Kaigler, D., Kim, K., and Mooney, D.J., 2004. Controlling rigidity and degradation of alginate hydrogels via molecular weight distribution. *Biomacromolecules*, 5(5), pp.1720–1727.

Lee, K.Y., Bouhadir, K.H., and Mooney, D.J., 2004. Controlled degradation of hydrogels using multi-functional cross-linking molecules. *Biomaterials*, 25(13), pp.2461–2466.

Lee, K.Y., Kong, H.J., Larson, R.G., and Mooney, D.J., 2003. Hydrogel Formation via Cell Crosslinking. *Advanced Materials*, 15(21), pp.1828–1832.

Lee, K.Y., and Mooney, D.J., 2012. Alginate: properties and biomedical applications. *Progress in polymer science*, 37(1), pp.106–126.

Lee, K.Y., Rowley, J.A., Eiselt, P., Moy, E.M., Bouhadir, K.H., and Mooney, D.J., 2000. Controlling mechanical and swelling properties of alginate hydrogels independently by cross-linker type and cross-linking density. *Macromolecules*, 33(11), pp.4291–4294.

Lee, S., Tong, X., and Yang, F., 2014. The effects of varying poly(ethylene glycol) hydrogel crosslinking density and the crosslinking mechanism on protein accumulation in three-dimensional hydrogels. *Acta Biomaterialia*, 10(10), pp.4167–4174.

Lee, V.K., Kim, D.Y., Ngo, H., Lee, Y., Seo, L., Yoo, S.-S., Vincent, P. a, and Dai, G., 2014. Creating perfused functional vascular channels using 3D bio-printing technology. *Biomaterials*, 35(28), pp.8092–102.

Levato, R., Visser, J., Planell, J.A., Engel, E., Malda, J., and Mateos-Timoneda, M.A., 2014. Biofabrication of tissue constructs by 3D bioprinting of cell-laden microcarriers. *Biofabrication*, 6(3), p.35020.

Li, J., Illeperuma, W.R.K., Suo, Z., and Vlassak, J.J., 2014. Hybrid hydrogels with extremely high stiffness and toughness. *ACS Macro Letters*, 3(6), pp.520–523.

Liu, R., Liang, S., Tang, X.-Z., Yan, D., Li, X., and Yu, Z.-Z., 2012. Tough and highly stretchable graphene oxide/polyacrylamide nanocomposite hydrogels. *Journal of Materials Chemistry*, 22(28), p.14160.

Liu, W., Zhang, Y.S., Heinrich, M.A., De Ferrari, F., Jang, H.L., Bakht, S.M., Alvarez, M.M., Yang, J., Li, Y.C., Trujillo-de Santiago, G., Miri, A.K., Zhu, K., Khoshakhlagh, P., Prakash, G., Cheng, H., Guan, X., Zhong, Z., Ju, J., Zhu, G.H., Jin, X., Shin, S.R., Dokmeci, M.R., and Khademhosseini, A., 2017. Rapid Continuous Multimaterial Extrusion Bioprinting. *Advanced Materials*, 29(3), pp.1–8.

Loh, Q.L., and Choong, C., 2013. Three-Dimensional Scaffolds for Tissue Engineering Applications: Role of Porosity and Pore Size. *Tissue Engineering Part B: Reviews*, 19(6), pp.485–502.

Di Luca, A., Longoni, A., Criscenti, G., Lorenzo-Moldero, I., Klein-Gunnewiek, M., Vancso, J., van Blitterswijk, C., Mota, C., and Moroni, L., 2016. Surface energy and stiffness discrete gradients in additive manufactured scaffolds for osteochondral regeneration. *Biofabrication*, 8(1), p.15014.

Luo, Y., Lode, A., and Gelinsky, M., 2013. Direct plotting of three-dimensional hollow fiber scaffolds based on concentrated alginate pastes for tissue engineering. *Advanced Healthcare Materials*, 2(6), pp.777–783.

Maher, P.S., Keatch, R.P., Donnelly, K., Mackay, R.E., and Paxton, J.Z., 2009. Construction of 3D biological matrices using rapid prototyping technology. *Rapid Prototyping Journal*, 15(3), pp.204–210.

Malda, J., Visser, J., Melchels, F.P., Jüngst, T., Hennink, W.E., Dhert, W.J. a, Groll, J., and Hutmacher, D.W., 2013. 25th anniversary article: Engineering hydrogels for biofabrication. *Advanced materials (Deerfield Beach, Fla.)*, 25(36), pp.5011–28.

Marx, V., 2015. Tissue engineering: Organs from the lab. *Nature*, 522(7556), pp.373–377.

Mazzoccoli, J.P., Feke, D.L., Baskaran, H., and Pintauro, P.N., 2010. Mechanical and cell viability properties of crosslinked low- And high-molecular weight poly(ethylene glycol) diacrylate blends. *Journal of Biomedical Materials Research - Part A*, 93(2), pp.558–566.

Melchels, F.P.W., Feijen, J., and Grijpma, D.W., 2010. A review on stereolithography and its applications in biomedical engineering. *Biomaterials*, 31(24), pp.6121–6130.

Miller, J.S., Stevens, K.R., Yang, M.T., Baker, B.M., Nguyen, D.-H.T., Cohen, D.M., Toro, E., Chen, A.A., Galie, P. a, Yu, X., Chaturvedi, R., Bhatia, S.N., and Chen, C.S., 2012. Rapid casting of patterned vascular networks for perfusable engineered three-dimensional tissues. *Nature materials*, 11(9), pp.768–74.

Mironi-Harpaz, I., Wang, D.Y., Venkatraman, S., and Seliktar, D., 2012. Photopolymerization of cell-encapsulating hydrogels: Crosslinking efficiency versus cytotoxicity. *Acta Biomaterialia*, 8(5), pp.1838–1848.

Murphy, S. V, and Atala, A., 2014. 3D bioprinting of tissues and organs. *Nature Biotechnology*, 32(8), pp.773–785.

Murphy, S. V., Skardal, A., and Atala, A., 2013. Evaluation of hydrogels for bio-printing applications. *Journal of Biomedical Materials Research - Part A*, 101 A(1), pp.272–284.

Murphy, W.L., McDevitt, T.C., and Engler, A.J., 2014. Materials as stem cell regulators. *Nature Materials*, 13(6), pp.547–557.

Naficy, S., Kawakami, S., Sadegholvaad, S., Wakisaka, M., and Spinks, G.M., 2013. Mechanical properties of interpenetrating polymer network hydrogels based on hybrid ionically and covalently crosslinked networks. *Journal of Applied Polymer Science*, 130(4), pp.2504–2513.

Nakamura, M., Iwanaga, S., Henmi, C., Arai, K., and Nishiyama, Y., 2010. Biomatrices and biomaterials for future developments of bioprinting and biofabrication. *Biofabrication*, 2(1), p.14110.

Nichol, J.W., Koshy, S.T., Bae, H., Hwang, C.M., Yamanlar, S., and Khademhosseini, A., 2010. Cell-laden microengineered gelatin methacrylate hydrogels. *Biomaterials*, 31(21), pp.5536–5544.

Ober, T.J., Foresti, D., and Lewis, J.A., 2015. Active mixing of complex fluids at the microscale. *Proceedings of the National Academy of Sciences*, 112(40), pp.12293–12298.

Okamoto, T., Suzuki, T., and Yamamoto, N., 2000. Microarray fabrication with covalent attachment of DNA using bubble jet technology. *Nature biotechnology*, 18(4), pp.438–441.

Okumura, Y., and Ito, K., 2001. The polyrotaxane gel: A topological gel by figure-of-eight cross-links. *Advanced Materials*, 13(7), pp.485–487.

Olsen, A.L., Bloomer, S.A., Chan, E.P., Gaca, M.D.A., Georges, P.C., Sackey, B., Uemura, M., Janmey, P.A., and Wells, R.G., 2011. Hepatic stellate cells require a stiff environment for myofibroblastic differentiation. *AJP: Gastrointestinal and Liver Physiology*, 301(1), pp.G110–G118.

Onoe, H., Okitsu, T., Itou, A., Kato-Negishi, M., Gojo, R., Kiriya, D., Sato, K., Miura, S., Iwanaga, S., Kuribayashi-Shigetomi, K., Matsunaga, Y.T., Shimoyama, Y., and Takeuchi, S., 2013. Metre-long cell-laden microfibres exhibit tissue morphologies and functions. *Nature materials*, 12(6), pp.584–90.

Oyen, M.L., 2014. Mechanical characterisation of hydrogel materials. *International Materials Reviews*, 59(1), pp.44–59.

Ozbolat, I.T., and Hospodiuk, M., 2016. Current advances and future perspectives in extrusion-based bioprinting. *Biomaterials*, 76, pp.321–343.

Pati, F., Jang, J., Ha, D.-H., Won Kim, S., Rhie, J.-W., Shim, J.-H., Kim, D.-H., and Cho, D.-W., 2014. Printing three-dimensional tissue analogues with decellularized extracellular matrix bioink. *Nature communications*, 5, p.3935.

Patra, S., and Young, V., 2016. A Review of 3D Printing Techniques and the Future in Biofabrication of Bioprinted Tissue. *Cell Biochemistry and Biophysics*, 74(2), pp.93–98.

Pekkanen, A.M., Mondschein, R.J., Williams, C.B., and Long, T.E., 2017. 3D Printing Polymers with Supramolecular Functionality for Biological Applications. *Biomacromolecules*, p.acs.biomac.7b00671.

Qutachi, O., Vetsch, J.R., Gill, D., Cox, H., Scurr, D.J., Hofmann, S., Müller, R., Quirk, R.A., Shakesheff, K.M., and Rahman, C. V., 2014. Injectable and porous PLGA microspheres that form highly porous scaffolds at body temperature. *Acta Biomaterialia*, 10(12), pp.5090–5098.

Remminghorst, U., and Rehm, B.H.A., 2006. Bacterial alginates: From biosynthesis to applications. *Biotechnology Letters*, 28(21), pp.1701–1712.

Sant, S., Hancock, M.J., Donnelly, J.P., Iyer, D., and Khademhosseini, A.,

2010. Biomimetic gradient hydrogels for tissue engineering. *Canadian Journal of Chemical Engineering*, 88(6), pp.899–911.

Saums, M.K., Wang, W., Han, B., Madhavan, L., Han, L., Lee, D., and Wells, R.G., 2014. Mechanically and chemically tunable cell culture system for studying the myofibroblast phenotype. *Langmuir*, 30(19), pp.5481–5487.

Sawkins, M.J., Mistry, P., Brown, B.N., Shakesheff, K.M., Bonassar, L.J., and Yang, J., 2015. Cell and protein compatible 3D bioprinting of mechanically strong constructs for bone repair. *Biofabrication*, 7(3), p.35004.

Schuurman, W., Khristov, V., Pot, M.W., van Weeren, P.R., Dhert, W.J.A., and Malda, J., 2011. Bioprinting of hybrid tissue constructs with tailorable mechanical properties. *Biofabrication*, 3(2), p.21001.

Schuurman, W., Levett, P.A., Pot, M.W., van Weeren, P.R., Dhert, W.J.A., Hutmacher, D.W., Melchels, F.P.W., Klein, T.J., and Malda, J., 2013. Gelatin-methacrylamide hydrogels as potential biomaterials for fabrication of tissue-engineered cartilage constructs. *Macromolecular Bioscience*, 13(5), pp.551–561.

Seol, Y.J., Kang, H.W., Lee, S.J., Atala, A., and Yoo, J.J., 2014. Bioprinting technology and its applications. *European Journal of Cardio-thoracic Surgery*, 46(3), pp.342–348.

Sharma, B., Fermanian, S., Gibson, M., Unterman, S., Herzka, D.A., Cascio, B., Coburn, J., Hui, A.Y., Marcus, N., Gold, G.E., and Elisseeff, J.H., 2013. Human Cartilage Repair with a Photoreactive Adhesive-Hydrogel Composite. *Science Translational Medicine*, 5(167), p.167ra6-167ra6.

Singh, M., Berkland, C., and Detamore, M.S., 2008. Strategies and Applications for Incorporating Physical and Chemical Signal Gradients in Tissue Engineering. *Tissue Engineering Part B: Reviews*, 14(4), pp.341–366.

Skardal, A., Zhang, J., and Prestwich, G.D., 2010. Bioprinting vessel-like constructs using hyaluronan hydrogels crosslinked with tetrahedral polyethylene glycol tetracrylates. *Biomaterials*, 31(24), pp.6173–81.

Sobral, J.M., Caridade, S.G., Sousa, R.A., Mano, J.F., and Reis, R.L., 2011. Three-dimensional plotted scaffolds with controlled pore size gradients: Effect of scaffold geometry on mechanical performance and cell seeding efficiency. *Acta Biomaterialia*, 7(3), pp.1009–1018.

Sun, J.-Y., Zhao, X., Illeperuma, W.R.K., Chaudhuri, O., Oh, K.H., Mooney, D.J., Vlassak, J.J., and Suo, Z., 2012. Highly stretchable and tough

hydrogels. *Nature*, 489(7414), pp.133–136.

Sung, H.-J., Meredith, C., Johnson, C., and Galis, Z.S., 2004. The effect of scaffold degradation rate on three-dimensional cell growth and angiogenesis. *Biomaterials*, 25(26), pp.5735–5742.

Tabriz, A.G., Hermida, M.A., Leslie, N.R., and Shu, W., 2015. Three-dimensional bioprinting of complex cell laden alginate hydrogel structures. *Biofabrication*, 7(4), p.45012.

Truby, R.L., and Lewis, J.A., 2016. Printing soft matter in three dimensions. *Nature*, 540(7633), pp.371–378.

Wang, T., Liu, D., Lian, C., Zheng, S., Liu, X., and Tong, Z., 2012. Large deformation behavior and effective network chain density of swollen poly(N-isopropylacrylamide)–Laponite nanocomposite hydrogels. *Soft Matter*, 8(3), pp.774–783.

Weber, L.M., Lopez, C.G., and Anseth, K.S., 2009a. Effects of PEG hydrogel crosslinking density on protein diffusion and encapsulated islet survival and function. *Journal of Biomedical Materials Research Part A*, 90A(3), pp.720–729.

Weber, L.M., Lopez, C.G., and Anseth, K.S., 2009b. Effects of PEG hydrogel crosslinking density on protein diffusion and encapsulated islet survival and function. *Journal of Biomedical Materials Research Part A*, 90A(3), pp.720–729.

Wells, R.G., 2008. The role of matrix stiffness in regulating cell behavior. *Hepatology (Baltimore, Md.)*, 47(4), pp.1394–400.

Wong, J.Y., Velasco, A., Rajagopalan, P., and Pham, Q., 2003. Directed movement of vascular smooth muscle cells on gradient-compliant hydrogels. *Langmuir*, 19(5), pp.1908–1913.

Woodfield, T.B.F., Van Blitterswijk, C. a, De Wijn, J., Sims, T.J., Hollander, a P., and Riesle, J., 2005. Polymer scaffolds fabricated with pore-size gradients as a model for studying the zonal organization within tissue-engineered cartilage constructs. *Tissue engineering*, 11(9–10), pp.1297–1311.

Woodfield, T.B.F., Malda, J., De Wijn, J., Péters, F., Riesle, J., and Van Blitterswijk, C.A., 2004. Design of porous scaffolds for cartilage tissue engineering using a three-dimensional fiber-deposition technique. *Biomaterials*, 25(18), pp.4149–4161.

Wu, G.H., and Hsu, S.H., 2015. Review: Polymeric-based 3D printing for tissue engineering. *Journal of Medical and Biological Engineering*, 35(3),

pp.285–292.

Wu, W., Deconinck, A., and Lewis, J.A., 2011. Omnidirectional printing of 3D microvascular networks. *Advanced Materials*, 23(24), pp.H178-83.

Wu, Z., Su, X., Xu, Y., Kong, B., Sun, W., and Mi, S., 2016. Bioprinting three-dimensional cell-laden tissue constructs with controllable degradation. *Scientific Reports*, 6(April), p.24474.

Xu, T., Gregory, C. a, Molnar, P., Cui, X., Jalota, S., Bhaduri, S.B., and Boland, T., 2006. Viability and electrophysiology of neural cell structures generated by the inkjet printing method. *Biomaterials*, 27(19), pp.3580–8.

Xu, T., Jin, J., Gregory, C., Hickman, J.J., and Boland, T., 2005. Inkjet printing of viable mammalian cells. *Biomaterials*, 26(1), pp.93–99.

Yang, T., Malkoch, M., and Hult, A., 2013. Sequential interpenetrating poly(ethylene glycol) hydrogels prepared by UV-initiated thiol-ene coupling chemistry. *Journal of Polymer Science, Part A: Polymer Chemistry*, 51(2), pp.363–371.

Yasuda, K., Gong, J.P., Katsuyama, Y., Nakayama, A., Tanabe, Y., Kondo, E., Ueno, M., and Osada, Y., 2005. Biomechanical properties of high-toughness double network hydrogels. *Biomaterials*, 26(21), pp.4468–4475.

Yoon, H.J., Shin, S.R., Cha, J.M., Lee, S.H., Kim, J.H., Do, J.T., Song, H., and Bae, H., 2016. Cold water fish gelatin methacryloyl hydrogel for tissue engineering application. *PLoS ONE*, 11(10), pp.1–18.

Zein, I., Hutmacher, D.W., Tan, K.C., and Teoh, S.H., 2002. Fused deposition modeling of novel scaffold architectures for tissue engineering applications. *Biomaterials*, 23(4), pp.1169–1185.

Zhang, Y., Yu, Y., Akkouch, A., Dababneh, A., Dolati, F., and Ozbolat, I.T., 2015. In Vitro Study of Directly Bioprinted Perfusable Vasculature Conduits. *Biomaterials science*, 3(1), pp.134–143.

Zhang, Y., Yu, Y., Chen, H., and Ozbolat, I.T., 2013. Characterization of printable cellular micro-fluidic channels for tissue engineering. *Biofabrication*, 5(2), p.25004.

Zhang, Y., Yu, Y., and Ozbolat, I.T., 2013. Direct Bioprinting of Vessel-Like Tubular Microfluidic Channels. *Journal of Nanotechnology in Engineering and Medicine*, 4(May 2013), p.20902.

Zhao, Y., Nakajima, T., Yang, J.J., Kurokawa, T., Liu, J., Lu, J., Mizumoto, S.,

Sugahara, K., Kitamura, N., Yasuda, K., Daniels, A.U.D., and Gong, J.P., 2014. Proteoglycans and glycosaminoglycans improve toughness of biocompatible double network hydrogels. *Advanced Materials*, 26(3), pp.436–442.

Appendix A

Table A-1 List of chemicals and reagents used in this thesis.

Chemical/ Reagent	Product name	Product code	Company, location
αSMA primary antibody	Anti-Actin, α -Smooth Muscle antibody, Mouse monoclonal	A5228	Sigma-Aldrich, UK
10 kDa PEGDA	Poly(ethylene glycol) diacrylate average 10,000 MW	729094	Sigma-Aldrich, UK
20 kDa PEGDA	Poly(ethylene glycol) diacrylate average 20,000 MW	767549	Sigma-Aldrich, UK
AB/AM	Antibiotic Antimycotic Solution	A5955	Sigma-Aldrich, UK
Accutase	Accutase® solution	A6964	Sigma-Aldrich, UK
Acridine orange	Acridine Orange base	235474	Sigma-Aldrich, UK
Albumin ELISA	Rat Albumin ELISA Kit	ab108789	Abcam, UK
Alcian blue	Fluka Analytical Alcian Blue 8GX	05500	Honeywell, Romania
Alginate	Manugel GMB	-	FMC Biopolymer, UK
Bradford's reagent	Bradford's reagent	5002205	Bio-Rad, UK
BSA	Bovine Serum Albumin solution	A8412	Sigma-Aldrich, UK
CaCl2	Calcium chloride anhydrous	C1016	Sigma-Aldrich, UK
CaSO4	Alfa Aesar Calcium sulfate, anhydrous, 99%	40144	Thermo Fischer Scientific, UK
Collagen I	Corning® Collagen I, High Concentration, Rat Tail	354249	Corning, USA

Collagenase	Collagenase NB 4G Proved Grade	17465	Serva Electrophoresis, Germany
DMEM	Gibco™ DMEM, high glucose, HEPES	42430-025	Thermo Fischer Scientific, UK
DMSO	Dimethyl sulfoxide	D5879	Sigma-Aldrich, UK
EGTA	Ethylene glycol-bis(2-aminoethylether)-N,N,N′,N′-tetraacetic acid	03777	Sigma-Aldrich, UK
Endothelial medium	Endothelial Cell Medium (Ready-to-use)	C-22010	PromoCell
FBS	Foetal bovine serum	F9665	Sigma-Aldrich, UK
FITC-BSA	Albumin–fluorescein isothiocyanate conjugate	A9771	Sigma-Aldrich, UK
FITC-dextran	FITC-CM-Dextran	74817	Sigma-Aldrich, UK
Glucose	D-(+)-Glucose	G7021	Sigma-Aldrich, UK
HB gelatine	Gelatin from porcine skin powder, gel strength ~300 g Bloom, Type A, BioReagent, for electrophoresis, suitable for cell culture	G1890	Sigma-Aldrich, UK
HEPES	HEPES hemisodium salt	H9897	Sigma-Aldrich, UK
Hoechst	bisBenzimide H 33258	B2883	Sigma-Aldrich, UK
I-2959	2-Hydroxy-4′-(2-hydroxyethoxy)-2-methylpropiophenone	410896	Sigma-Aldrich, UK
IgG ELISA	Human IgG ELISA Kit	RAB0001	Sigma-Aldrich, UK
Insulin	Insulin, Recombinant Human	91077C	Sigma-Aldrich, UK

Insulin ELISA	SimpleStep ELISA™ Human Insulin ELISA Kit	ab200011	Abcam, UK
KCl	Potassium chloride	P5405	Sigma-Aldrich, UK
KH_2PO_4	Potassium phosphate monobasic	P5655	Sigma-Aldrich, UK
LAP	Lithium Phenyl(2,4,6-trimethylbenzoyl) phosphinate	L0290	Tokyo Chemical Industry Co., UK
LB gelatine	Gelatin from porcine skin, gel strength 90-110 g Bloom, Type A	G6144	Sigma-Aldrich, UK
L-Glutamine	L-Glutamine	G7513	Sigma-Aldrich, UK
LIVE/DEAD	Invitrogen LIVE/DEAD® Viability/Cytotoxicity Kit for mammalian cells	L3224	Thermo Fischer Scientific, UK
Matrigel	BD Matrigel Matrix	354234	BD Biosciences, USA
MEME	Minimal Essential Medium Eagle's	M2279	Sigma-Aldrich, UK
Methacrylic anhydride	Methacrylic anhydride	276685	Sigma-Aldrich, UK
Methionine	L-Methionine	M5308	Sigma-Aldrich, UK
NaCl	Sodium chloride	FLBP35810	Thermo Fischer Scientific, UK
$NaHCO_3$	Sodium bicarbonate	S5761	Sigma-Aldrich, UK
Na_2HPO_4	Sodium phosphate dibasic	S5136	Sigma-Aldrich, UK
NEAA	Gibco™ MEM Non-Essential Amino Acids Solution (100X)	11140035	Thermo Fischer Scientific, UK
Optiprep	OptiPrep™ Density Gradient Medium	D1556	Sigma-Aldrich, UK
Orange II	Orange II sodium salt	195235	Sigma-Aldrich, UK

PBS	Phosphate Buffered Saline Tablets	BR014G	Fisher BioReagents™ (Thermo Fischer Scientific), UK
PFA	Paraformaldehyde	158127	Sigma-Aldrich, UK
Phenol red	Phenol red indicator	151430250	Acros Organic (Thermo Fischer Scientific), UK
PrestoBlue	PrestoBlue® Cell Viability Reagent	A-13262	Invitrogen, Thermo Fischer Scientific, UK
Rhodamine B	Rhodamine B	R6626	Sigma-Aldrich, UK
Secondary antibody	Goat Anti-Mouse IgG H&L (Alexa Fluor® 488)	ab150113	Abcam, UK
Selenite	Sodium selenite	S9133	Sigma-Aldrich, UK
Sodium citrate	Sodium citrate monobasic	71497	Sigma-Aldrich, UK
TGFβ1	Recombinant Human Transforming Growth Factor-Beta 1	ABC7176	Source BioScience, UK
Triton X-100	Triton™ X-100	T8787	Sigma-Aldrich, UK
Trypsin	Trypsin solution from porcine pancreas	T4549	Sigma-Aldrich, UK
αMEM	Alpha MEM Eagle w/o L-Glutamine	BE12-169F	Lonza, UK

Appendix B

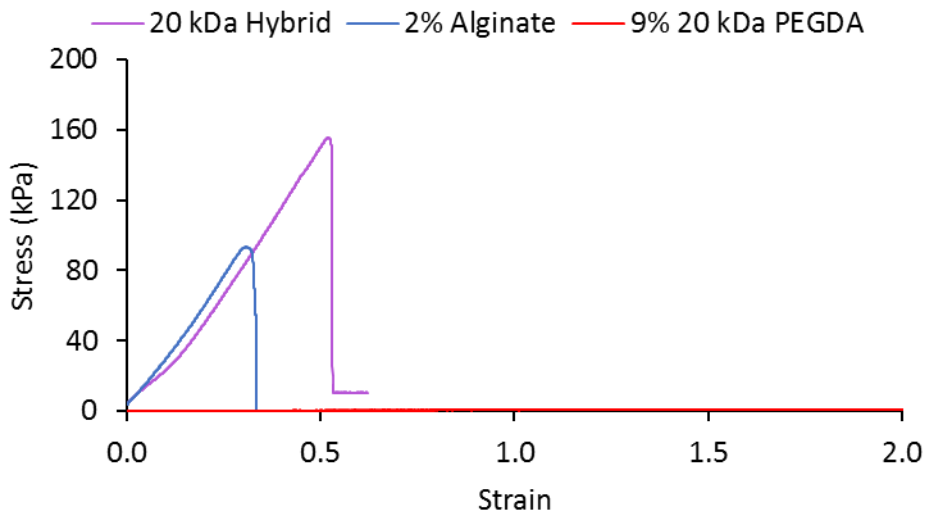

Figure B-1 Representative stress–strain curves of alginate, PEGDA and the hybrid hydrogels.

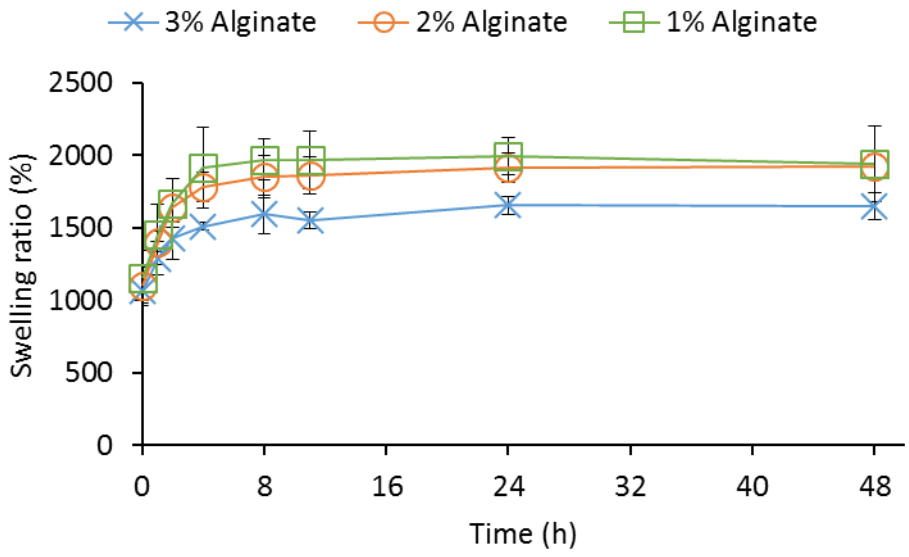

Figure B-2 Swelling profiles of pure alginate hydrogels. Mean values were plotted. Error bars represent standard deviation (n = 3).

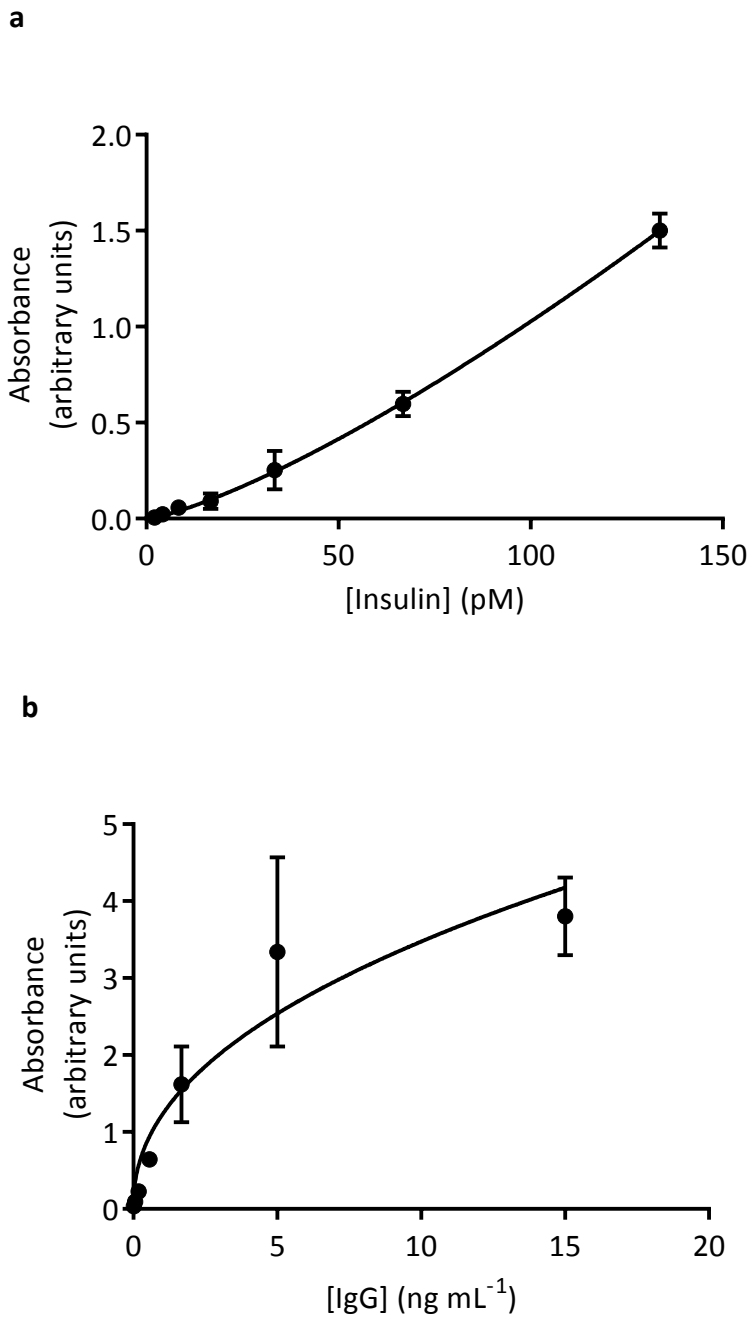

Figure B-3 ELISA standard curves. (a) Standard curve for Insulin ELISA. (b) Standard curve for IgG ELISA. Mean values were plotted. Error bars represent standard deviation (n = 3).

Appendix C

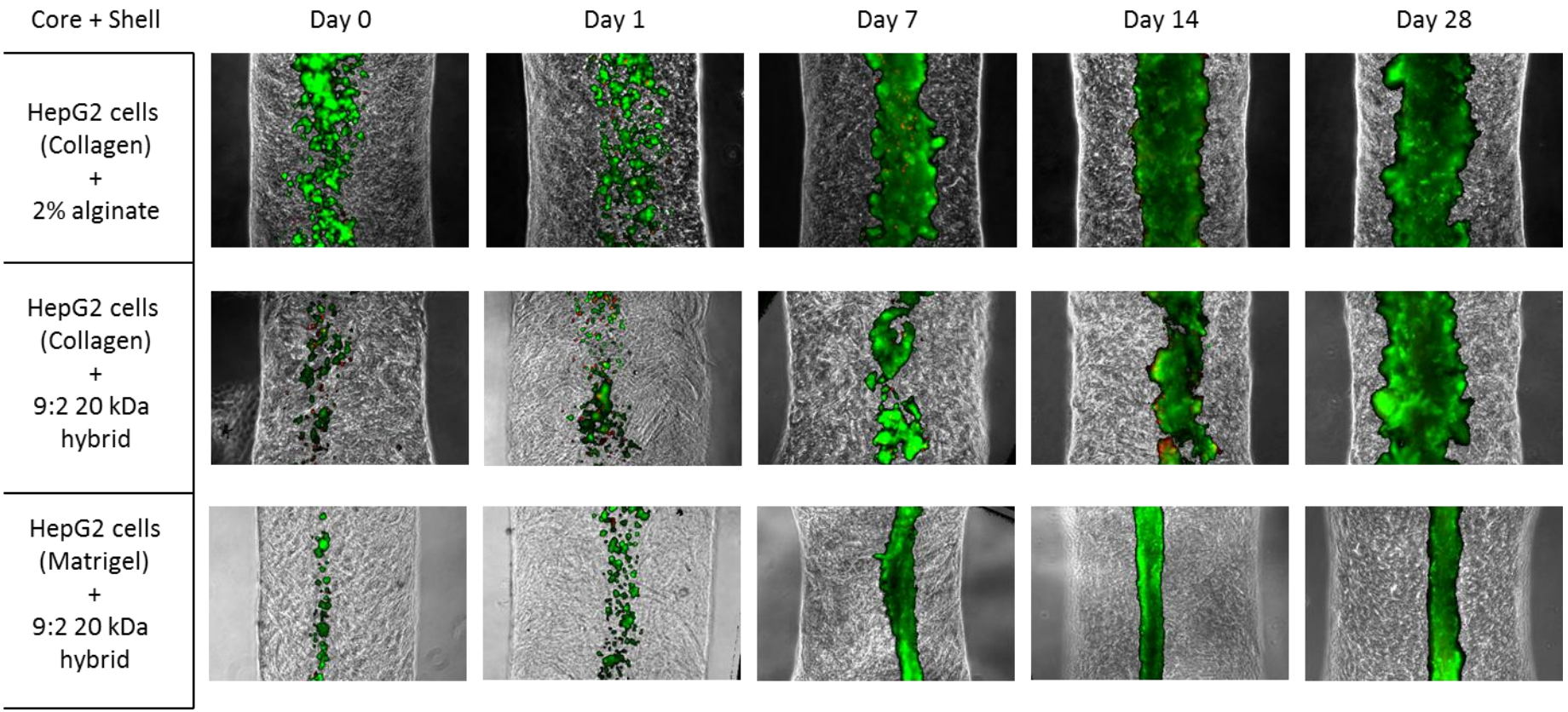

Figure C-1 LIVE/DEAD overlays showing the position of HepG2 cell-laden cores with respect to the whole core–shell strand.

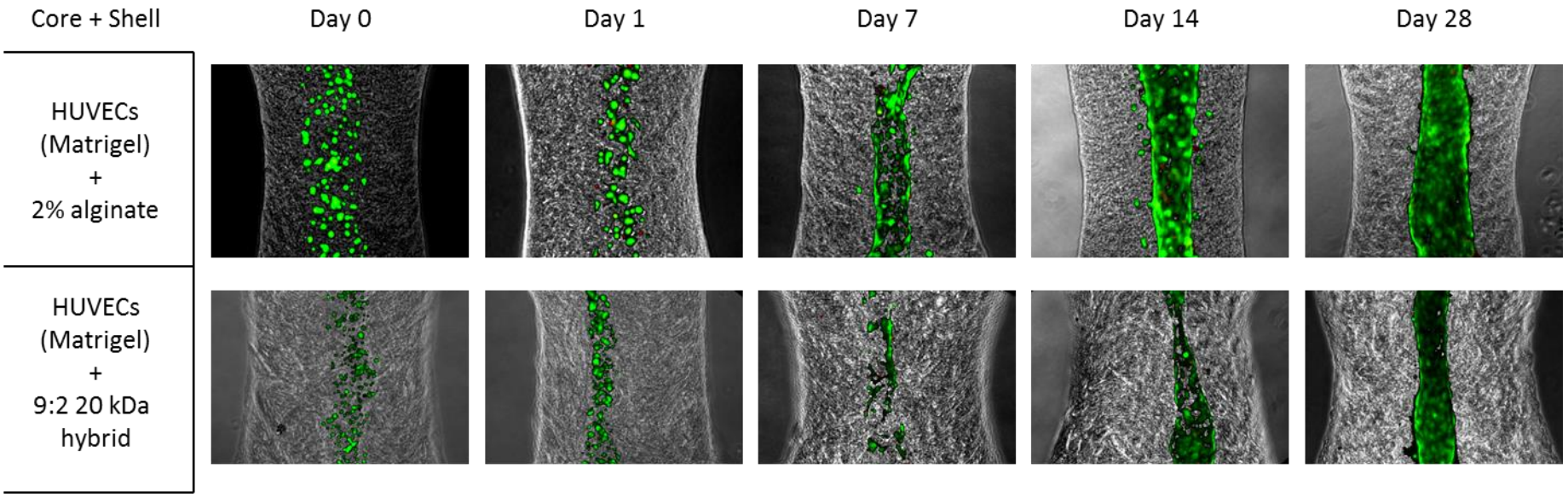

Figure C-2 LIVE/DEAD overlays showing the position of HUVEC-laden cores with respect to the whole core–shell strand.

Appendix D

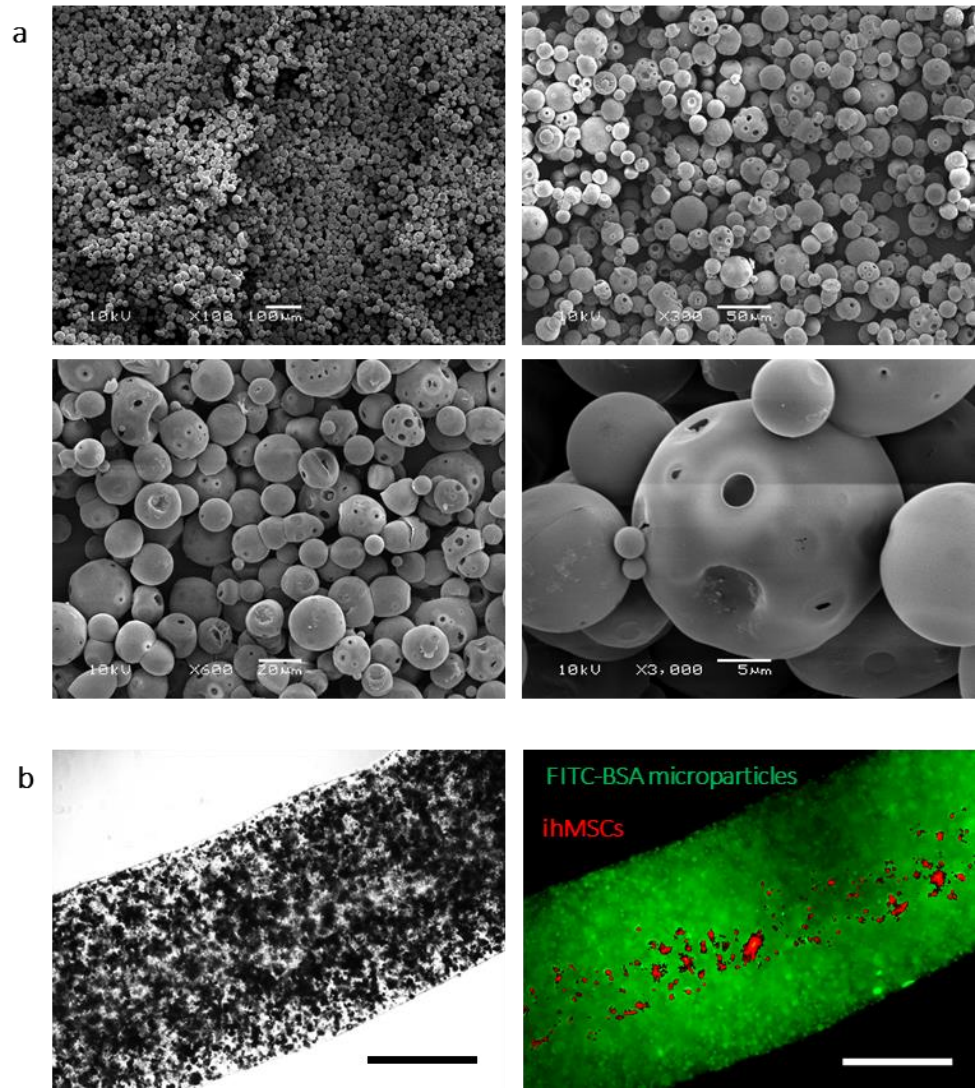

Figure D-1 FITC-BSA-loaded microparticles for gradient printing. (a) SEM of microparticles loaded with FITC-BSA. (b) Brightfield (left) and fluorescent (right) images of a cell-laden core–shell strand with microparticles in the shell.

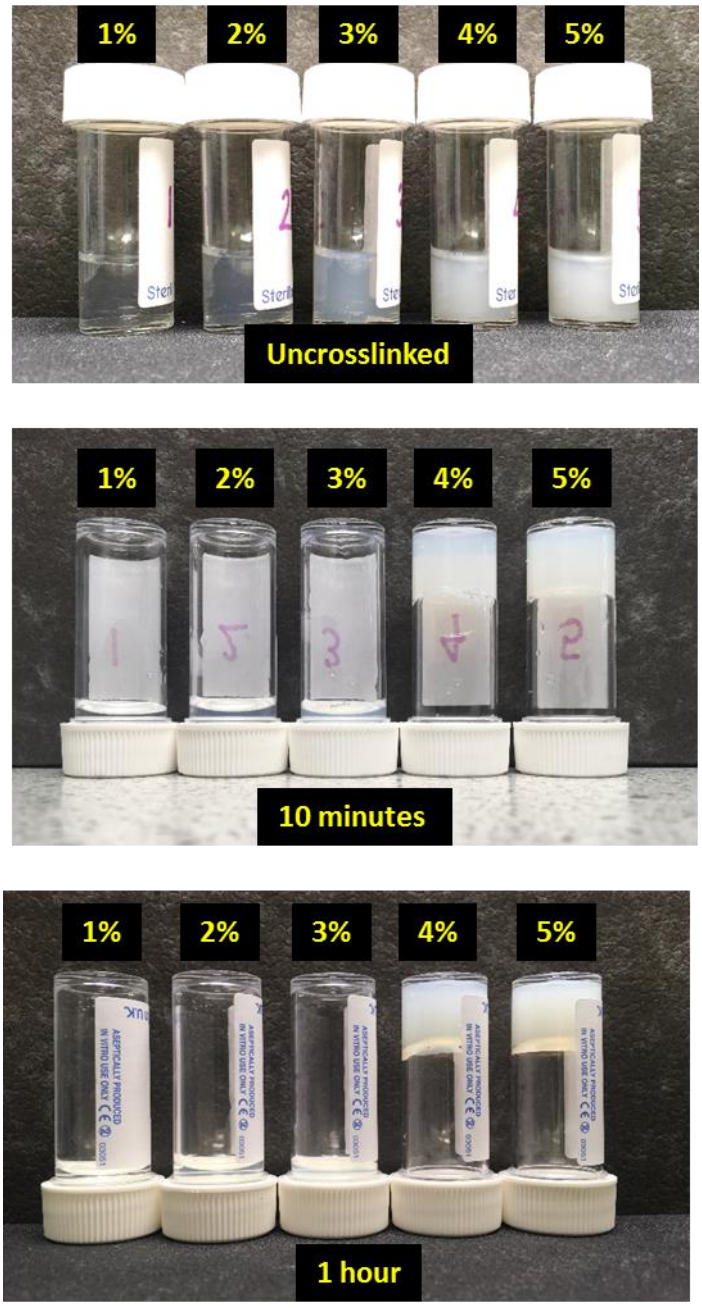

Figure D-2 Minimum concentration of GelMA required to form a stable hydrogel. GelMA was poured into vials and photocrosslinked. The vials were then inverted to check the fluidity and stability of the gels. Below 4%, GelMA was unable to polymerise, even after 1 hour of photocrosslinking. At 4%, the GelMA hydrogel was too soft to be handled and therefore 5% was chosen.

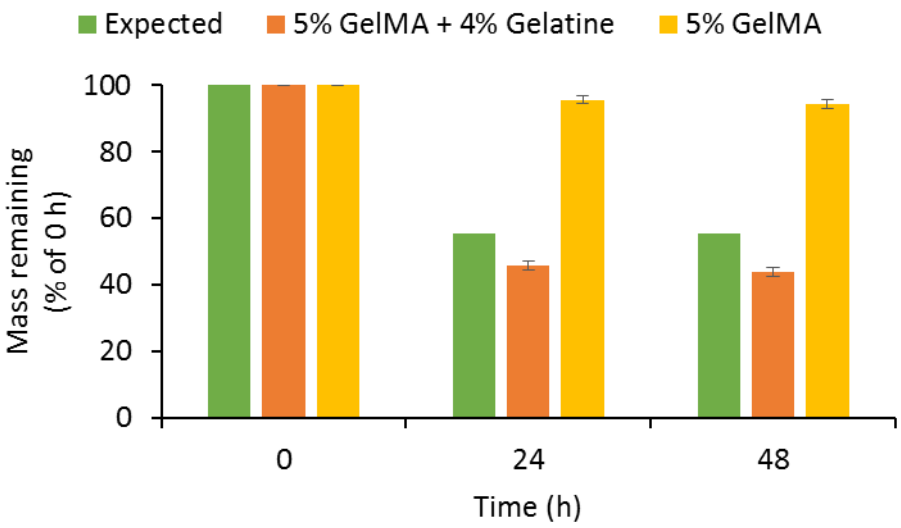

Figure D-3 Gelatine can be removed from GelMA hydrogels by incubation at 37°C. GelMA hydrogels were prepared either with or without gelatine, and incubated in PBS at 37°C. At the indicated time points, the hydrogels were freeze dried and the dry mass was measured. The percentage change in mass of each hydrogel was calculated. Mean values were plotted. Error bars represent standard deviation (n = 3).